Micro-bubble dynamics in turbulent flow

Zhentong Zhang

THÈSE

En vue de l'obtention du

DOCTORAT DE L'UNIVERSITÉ DE TOULOUSE

Délivré par :

Institut National Polytechnique de Toulouse (Toulouse INP)

Discipline ou spécialité :

Energétique et Transferts

Présentée et soutenue par :

M. ZHENTONG ZHANG

le mardi 19 novembre 2019

Titre :

Micro-bubble dynamics in turbulent flow

Ecole doctorale :

Mécanique, Energétique, Génie civil, Procédés (MEGeP)

Unité de recherche :

Institut de Mécanique des Fluides de Toulouse (IMFT)

Directeur(s) de Thèse :

M. DOMINIQUE LEGENDRE

M. RÉMI ZAMANSKY

Rapporteurs :

M. CHAO SUN, UNIVERSITE DE TSINGHUA A PEKIN

M. MIKHAEL GOROKHOVSKI, ECOLE CENTRALE DE LYON

Membre(s) du jury :

M. MIKHAEL GOROKHOVSKI, ECOLE CENTRALE DE LYON, Président

M. DOMINIQUE LEGENDRE, TOULOUSE INP, Membre

Mme AURORE NASO, ECOLE CENTRALE DE LYON, Membre

M. RÉMI ZAMANSKY, TOULOUSE INP, Membre

M. SERGIO CHIBBARO, UNIVERSITE PIERRE ET MARIE CURIE, Membre

Micro-bubble dynamics in turbulent flow

Zhentong Zhang

A thesis presented for the degree of
Doctor of Philosophy

19 November 2019

Abstract

This thesis is devoted to the study of the motion of small bubbles in homogeneous isotropic turbulent flows. The work addresses several questions related to the statistical description of the hydrodynamic forces exerted on a bubble as well as the stochastic modeling of their high frequency fluctuations. First, we propose a model for the acceleration of micro-bubbles (smaller than the dissipative scale of the flow) subjected to the drag and the fluid inertia forces. This model, that depends on the Stokes number, the Reynolds number and the density ratio, reproduces the evolution of the acceleration variance as well as the relative importance and alignment of the two forces as observed from Direct Numerical Simulations (DNS). Second, based on the observation that acceleration statistics conditional to the local kinetic energy dissipation rate are invariant with the Stokes number and the dissipation rate, we propose a stochastic model for the instantaneous bubble acceleration vector accounting for the small-scale intermittency of the turbulent flows. The norm of the bubble acceleration is obtained by modeling the dissipation rate along the bubble trajectory from a log-normal stochastic process, whereas its orientation is given by two coupled random walk on a unit sphere in order to model the evolution of the joint orientation of the drag and inertia forces acting on the bubble. Furthermore, the proposed stochastic model for the bubble acceleration is used in the context of large eddy simulations (LES) of turbulent flows laden with small bubbles. It can effectively reproduce effect of turbulent motion at scales smaller than the mesh resolution by adding a random contribution depending on local average dissipation rate. Comparisons with DNS and standard LES, show that the proposed model improves significantly the statistics of the bubbly phase. Third, we extend the previous results in the case of bubbles with large Reynolds number by considering non-linear drag laws. We define an effective relaxation time based on the drag coefficient to characterize bubble motion (acceleration,velocity). Eventually we study the effect of buoyancy and lift force on the bubble dynamics, and analyze the reduction of the average rising velocity in turbulent flow compared to quiescent flows. It is observed that bubbles preferentially explore region having downward fluid acceleration which contributes through the inertia force to reduction of the rising velocity. In addition, as already observed, the lift force brings preferably bubbles into downstream fluid motion which also reduce their rising velocity.

Key words: Bubble dynamics, isotropic turbulence, LES, sub-grid model, two-phase flow.

Résumé

Cette thèse est consacrée à l'étude du mouvement de bulles dans des écoulements turbulents homogènes isotropes. Le travail aborde différentes questions liées à la description statistique des forces hydrodynamiques exercées sur une bulle ainsi qu'à leur modélisation stochastique tenant compte des effets d'intermittence. Nous proposons un modèle pour l'accélération de bulles de taille inférieures à l'échelle Kolmogorov soumises à la traînée et aux forces d'inertie du fluide. Ce modèle, qui dépend du nombre de Stokes, du nombre de Reynolds et du rapport de densité, reproduit l'évolution de la variance d'accélération ainsi que l'importance relative et l'alignement des deux forces observées à partir de DNS. Deuxièmement, sur la base de l'observation selon laquelle les statistiques d'accélération conditionnelles au taux de dissipation de l'énergie cinétique locale sont invariantes avec le nombre de Stokes et le taux de dissipation, nous proposons un modèle stochastique du vecteur d'accélération instantanée de la bulle, qui tient compte de l'intermittence à petite échelle de la turbulence. La norme de l'accélération de la bulle est obtenue en modélisant le taux de dissipation le long de la trajectoire de la bulle à partir d'un processus stochastique log-normal, tandis que son orientation est donnée par deux marches aléatoires couplées sur une même sphère afin de modéliser l'évolution de l'orientation conjointe la traînée et les forces d'inertie agissant sur la bulle. Le modèle stochastique proposé pour l'accélération des bulles permet d'améliorer les simulations de grandes turbulences (LES) d'écoulements turbulents transportant de petites bulles. Il peut reproduire efficacement l'effet des échelles turbulentes inférieures à la résolution du maillage en ajoutant une contribution aléatoire en fonction du taux de dissipation moyen local. Les comparaisons avec le DNS et les LES standard montrent que le modèle proposé améliore considérablement les statistiques de la phase de formation de bulles. Troisièmement, nous étendons les résultats précédents dans le cas de bulles à plus grand nombre de Reynolds en prenant en compte les lois de traînée non-linéaires. Nous définissons un temps de relaxation effectif basé sur le coefficient de traînée pour caractériser le mouvement de la bulle (accélération, vitesse). Finalement, nous étudions l'effet de la flottabilité et de la force de portance sur la dynamique des bulles et analysons la réduction de la vitesse moyenne ascensionnelle dans les écoulements turbulents par rapport aux écoulements au repos. On observe que la bulle explore de préférence une région ayant une accélération de fluide vers le bas qui contribue, par le biais de la force d'inertie, à réduire la vitesse de montée. De plus, comme déjà observée, la force de portance amène de préférence les bulles dans un mouvement de fluide en aval qui réduit également leur vitesse de montée.

Mots clés: Dynamiques des bulles, turbulence isotropie, LES, modèle de sous-maillage, écoulement diphasique.

Acknowledgments

I would like to express my sincere appreciations to Dominique Legendre and Rémi Zamansky for framing these thesis works. Their valuable advises and constant guidance have been greatly helpful to me during these years. Many thanks to both of them for their kindness and encouraging speeches during my thesis defense.

I have known Dominique Legendre even before that I had started my Ph.D. He inspired my interest in scientific research which influenced greatly my career planning. He guided me step by step to entering the career of research. It is always intriguing and delightful to talk with him. His suggestions and his vision in physics are crucial to my Ph.D works.

My gratitude to Rémi Zamansky for sharing his rich knowledge of turbulence, math and computational skills. Also the numerical code used in this work is developed based on his program *FieldZ*. His vision of physics and the way he works thought me how to initiate my research career. His brilliant ideas and advises guided me throughout this whole project and also he gave many suggestions for my future career.

I wish to thank Chao Sun and Michael Gorokhovski, the rapporteurs of this manuscript, for their careful reading and their pertinent remarks. Also the discussions with Professor Gorokhovski enlightened me greatly during the studies. Thanks to Professor Sun for travailing thousands kilometers from Beijing to my thesis defense and he gave me so many valuable suggestions.

I also thank Aurore Naso and Sergio Chibbaro for having accepted to be members of my jury. Many appreciations for their comments and interesting questions during the thesis defense.

I warmly thank my dear friends and colleagues in IMFT for their accompany and exchanges of working skills.

Thanks to my parents for supporting me in making this professional choices. Know that I am infinitely grateful to you.

Yang, thank you for sharing my life and for your encourages.

Contents

Chapter 1

Introduction

Small bubbles dispersed in turbulence can be found in many natural phenomena and a lot of real life applications. The studies of the bubble dynamics in turbulent flows can improve the understanding of climate changing and optimization of industrial design.

For example, the environmental change due to human activities brings a lot of attention in the scientific society. Recent researches of climate change review the importance of the transfer of the CO2 from the atmosphere to the ocean which will acidify the water body. And a portion of the CO2 is captured by trapping of small bubbles of atmospheric gases in the ocean by breaking waves. The smallest typical ocean dissipative scale $\eta_0 \sim \mathcal{O}(1mm)$ and the typical bubble size vary from $1 - 100\mu m$. Studies of these bubbles motion under the buoyancy and oceanic turbulence are of great interests to estimate qualitatively the CO2 transfer across the ocean surface [1, 2] as illustrated in figure 1.1.

Micro-bubbles are also used for improving industrial design, such as drag reduction of the turbulence boundary layer [3, 4]. The concept is to inject small bubbles with comparable size of Kolmogorov scale of the turbulent boundary layer. An experimental characterization of the turbulent boundary layer over a flat plate in the presence of small amounts of micro-bubbles has proved that, even at a small void fraction, the interaction between bubbles and turbulence leads to significant modifications of the underlying flow field. This concept can be wildly used in maritime vessel fabrication, see figure 1.2.

Besides, the micro-bubble turbulence system can also be fund in chemical reactors, water treatment, steam generators, etc. These above examples demonstrate the crucial importance of understanding the dynamics of bub-

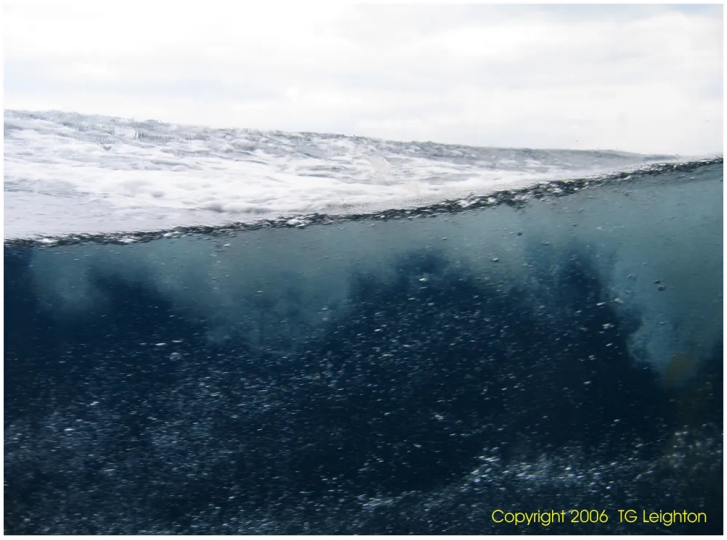

Figure 1.1: Photography showing a bubble cloud under the surface of the ocean. [1]

bles in turbulence. The ultimate objective is to understand and model the physical mechanism in order to prediction and optimal design. The development of computational technology not only change our lifestyle but also introduce a brand new approach for scientific research. The high performance supercomputer is widely used in both fundamental studies of basic physical mechanisms and engineering analyses. Especially in fundamental studies, numerical simulations can help us to understand the mechanisms and further to establish mathematical models to describe physical phenomena. In order to simulate realistically the physical phenomena, it requires sometime extremely high accuracy and resolution. For instance, in fluid dynamic problems, the motion of the fluid can be simulated by numerically resolving the Navier-Stokes equations. The full resolution of the system of equations needs to resolve the smallest scales to capture all the information of the fluid field which is often referred as a Direct Numerical Simulation (DNS). However, in bubbly turbulent flows, the Reynolds number is generally large and the complexity of such flows lies in the coupling between the various physical phenomena. When the Reynolds number of the flow is very large, the continuous phase presents strong fluctuations of the velocity at the scale of the bubble. Despite its crucial position in the academic research, the DNS for high Reynolds number two phases or multi-phase turbulent flows can hardly be considered as practical in industrial applications due to the limitation of the computational capacities. Therefore, in numerical study, we usually seek to simplify the problem as long as the assumptions that we

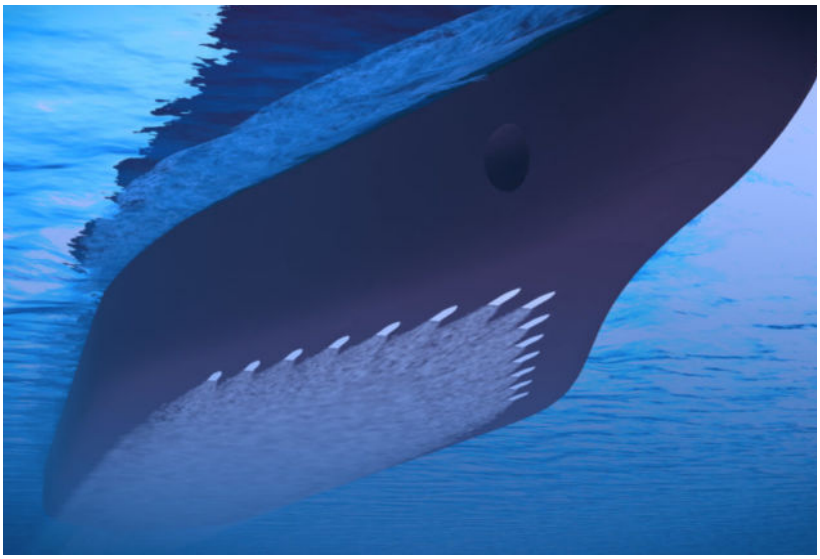

Figure 1.2: Illustration of air lubrication technology

made are adequate to the specific problem that we are interested in.

The present work focus on a particular situation where the bubble diameter is smaller than the Kolmogorov scale $d_b \ll \eta$ so that such a bubble is called *micro-bubble*. Among all the existing numerical methods, the point-wise particle approximation is often used to deal with small dispersed bubbles with diameter smaller than the Kolmogorov scale. One good reason is that, a DNS resolves only the turbulent fluid motion of length scales equal or greater than the Kolmogorov length scale and the fluid seen by the bubble in such case can be approximately regarded as uniform at the bubble scale. The bubbles we consider in such context will be regarded as no-deformable spherical particles with slip or no-slip boundary condition, with density and viscosity are much smaller than the carrier flow. The concept of this method consists in computing the turbulent field by resolving Navier-Stokes equations as if there is no dispersed phase. And then the resolved fluid information interpolated at the positions of the bubbles are used to solve their Lagrangian trajectory by considering the force balance applied on each bubble [5].

This approximation is a classic method for numerical studies of the particle-laden turbulence. For heavy particles, [6] used this approach to study the settling of aerosol particles for moderate Reynolds (drag and gravity) and they have found that the settling velocity of heavy particles will be increased in the turbulence compared to that in the quiescent flow. Later [7] included

the Basset force in the equation of motion to study this effect for the particle settling in turbulence and found that the Basset force has virtually no influence on the structure of the fluid velocity fluctuations seen by the particles and on particle diffusivity. [8] studied the turbulence effect on the drag force and concluded that the drag force estimated by this method is only applicable for small particles. [9] Investigated the preferential concentration effect with this approach, and analysis the threshold of the Stokes number for the clustering effect. [10] studied heavy particle acceleration statistics and found that the variance of heavy particle acceleration sharply falls off from the fluid tracer value at quite small Stokes numbers and the tails of the probability density function of the normalized acceleration decreases with the Stokes number.

For bubbles or light particles in turbulence, [11] found that the bubble rising velocity is reduced by the turbulence. [12] and [13] showed that the lift force along with gravity makes the bubble preferably sampling the down flow region of the turbulence and use two-way coupling to study bubble influence backward to the carrier flow. They found that the small wavenumbers are attenuated and the large ones are enhanced by the bubble which is due to the bubble clustering in down-flow regions. Considering bubble acceleration statistics [14], showed that the forces acting on bubbles are strongly intermittent, and they argued that this holds in particular for the lift force that is proved to be a very intermittent quantity.

The development of Large Eddies Simulation (LES) provides another approach to further simplify the problem. The method has a great potential for being a prediction tool for the engineering interest, because of its efficiency compared to direct numerical simulation. It demands less computational resources and can estimate the large scale feature of very high Reynolds number based on a scale separation hypothesis [15]. The largest scales are directly conditioned by the boundary conditions and are thus "case dependent" while the small scales are believed to present the universality (locally homogeneous and isotropic). In the meantime, most of the kinetic energy is contained in the large scales and thus contributes significantly to dispersion phenomena at long time. In LES, the unresolved scales can be modeled by the turbulent viscosity ν_Δ which is responsible for the energy flux to the smaller scales. However, the model can only provide an estimation of the influence of these small scales on the fluid motion at larger scales. The instantaneous velocity u_i, governed by the Navier-Stokes equations, is composed of filtered and residual components:

$$u_i = \overline{u}_i + u_i'$$

This decomposition into filtered and residual components can also be applied

to the material acceleration (or total acceleration) $a_i = \frac{\partial u_i}{\partial t} + u_k \frac{\partial u_i}{\partial x_k}$ [16]:

$$a_i = \overline{a}_i + a'_i$$

In LES, only $\overline{u}_i$ and $\overline{a}_i$ are explicitly resolved and the residual contribution u'_i and a'_i are not resolved. When we compute the hydrodynamic forces on a bubble to track its trajectory, only the filtered (resolved) parts are accounted for in standard LES, while the small scales' contributions to the bubble acceleration $\boldsymbol{a}'_b$ are discarded.

$$a_{bi}(u_{fi}, a_{fi}) = \overline{a}_{bi}(\overline{u}_{fi}, \overline{a}_{fi}) + a'_{bi}(u'_{fi}, a'_{fi})$$

The experimental studies of fluid tracer Lagrangian acceleration [17, 18, 19] reported that Lagrangian acceleration presents probability density distributions with stretched tails, depending on the Reynolds number. Also, the intermittent Lagrangian acceleration may induce strong fluctuations to the bubble. [14] and [20] reported that the bubble acceleration is even more intermittent than the fluid tracer. This intermittency is mainly manifested by those small scale fluctuations. Those small scales are typically associated with the large fluctuations of the dissipation rate of turbulent kinetic energy ε [21, 22, 23, 16]. As a consequence, if we want to obtain predictive results by LES-type methods, a sub-grid model is needed to reproduce the interaction of the bubble with the small-scale fluid motion, namely the residue bubble acceleration $a'_{bi}(u'_{fi}, a'_{fi})$ in LES.

A sub-grid stochastic acceleration model has already been proposed for heavy particle in THI [24]. In heavy particle dynamics, only the drag force is taken into account. However, the bubble dynamic is different because of the presence of the fluid inertia force. According to the theory of Tchen (1947) [25], light particle amplifies the high frequency fluctuations of the fluid field. Bubbles basically have no inertia and thus are extremely sensitive to the fluctuations of the velocity field around them. It is like a "hole" moving in the continuous media which granted a force that suppose to act originally on the same volume of fluid substance who shall occupy this "hole". Supplemented with the added mass force, the bubble has an acceleration even larger than the fluid particle due to its small density. The theory has been confirmed in later investigation [26], and it has also been found that the light particle's acceleration fluctuation is even more intense than that of the fluid tracer [20, 27, 28].

Therefore, we focus on this research topic to develop a tool for numerical simulations of large scales (LES) for homogeneous isotropic turbulent flow laden with point-wise bubbles. The question then arises to correctly estimate the turbulent fluctuations of the carrier flow in sub-mesh scale and in particular those "seen" by the bubbles. This is our motivation to use

stochastic model of phenomena related to unresolved scales. The interest of coupling LES with the sub-grid acceleration stochastic models is to give access to the unresolved and intermittent structures of the turbulent flow and at the same time to take into account the general organization of Large-scale flows.

We will present in this document how to account for the contribution of the fluid inertia force into such sub-grid model. The concept of the sub-grid model is to take account the filtered field contribution and along with a random force reproducing the fluctuations of small-scale fluid structure. The decomposition can be represented by

$$\boldsymbol{a}_b = \overline{\boldsymbol{a}}_b + |\boldsymbol{a}_b^*| \cdot \boldsymbol{e}^* \tag{1.1}$$

where $\boldsymbol{a}_b$ is the bubble acceleration, the over-bar denotes the resolved large scale contribution and the unresolved small scale contribution $\boldsymbol{a}_b'$ is modeled by $|\boldsymbol{a}_b^*| \cdot \boldsymbol{e}^*$ with $|\boldsymbol{a}_b^*|$ is the amplitude and $\boldsymbol{e}^*$ is a random orientation. Variable with '$*$' denote a variable obtained with the model. The resolved large scale contribution is computed by interpolating on the coarse mesh. Based on the time scale separation between the evolution of the norm and the orientation [18, 29] the unresolved contribution can be expressed by the product of two stochastic processes, one for the amplitude and the other for its orientation vector. Due to the times correlation of the amplitude and the orientation which are very different, we can assume that the two variables are independent [24, 23, 22].

Outline of the document: In Chapter 2, we begin with a short introduction on isotropic and homogeneous turbulence to recall the usual definition of the intermittency of the turbulence acceleration and its influence to the dispersed phases. We present a classic stochastic process to model the variable having a log-normal distribution. In Chapter 3, the point-particle approximation (Euler-Lagrangian method) is presented and we discuss the hypothesis to use this method to track micro-bubbles in turbulence. In Chapter 4, we provide the detail of the numerical code to resolve the statistical stationary IHT field in a 3D box with periodical conditions. The Lagrangian statistics of a fluid tracer is presented in this part. Chapter 5 is presented in a form of a standalone article on studying the bubble dispersed in THI with a DNS using the point particle approach. The hydrodynamic forces are only taking account of the drag and inertia forces. The main question is to understand the statistical features of these forces and the relation between them. We propose a model for the acceleration of micro-bubbles (smaller than the dissipative scale of the flow) subjected to the drag and the fluid inertia forces in a homogeneous and isotropic turbulent flow. This model accounts for the effects of the Stokes number, the Reynolds number

and the density ratio. In Chapter 6, we use DNS to study the influence of the bubble Reynolds number corrections to the drag law, while in Chapter 7, we study the bubble motion with the presence of gravity. We discuss the finite Re_b effect as well as the fluid inertia force effect to the rising velocity. Also we present the acceleration statistics of the bubble when considering the gravity. In Chapter 8, the influence of the lift force on the bubble dynamics is considered.

Chapter 2

Quick introduction to turbulent flows

A flow can be generally classified in two regimes: laminar or turbulence. Laminar flows are calm and smooth and the flow field is organized in a deterministic manner at any position of the fluid and any time. The counterpart is called turbulent flow or turbulence. It is a general characterization of that fluid field having highly fluctuated velocity, pressure or other mechanic quantities.

In order to measure the competition between the fluid inertia and the viscous effect, George Stokes introduced a dimensionless parameter, the Reynolds number $Re = \frac{U.L}{\nu}$, where $U(m/s)$ denotes the characteristic velocity, $L(m)$ denotes the characteristic length and $\nu(m^2/s)$ is the kinetic viscosity. For given boundary conditions, the Reynolds number is the only control parameter of the flow. The flow is expected to be turbulent when Re it is sufficiently large. The concept of Reynolds number greatly simplifies the investigation of flows with similar geometrical configuration. In the context of this paper, we focus on flows with large Reynolds number.

Based on the fundamental physical laws, the Navier-Stokes equations have been introduced. It is a set of two partial differential equations: the mass conservation Eq. (2.1) and momentum conservation Eq. (2.2), describing the motion of a viscous fluid named Navier-Stokes equations after Claude-Louis Navier and George Stokes.

$$\frac{\partial u_i}{\partial x_i} = 0 \tag{2.1}$$

$$\frac{\partial u_i}{\partial t} + u_k \frac{\partial u_i}{\partial x_k} = -\frac{1}{\rho}\frac{\partial P}{\partial x_i} + \nu \frac{\partial}{\partial x_j}\left(\frac{\partial u_i}{\partial x_j} + \frac{\partial u_j}{\partial x_i}\right) + f_i \tag{2.2}$$

In the equation the velocity $u_i(\boldsymbol{x}, t)$ for $i = 1, 2, 3$ is a vector of 3 components and the pressure $P(\boldsymbol{x}, t)$ is a scalar. These variables are function of space $\boldsymbol{x} = x_i$ for $i = 1, 2, 3$ and time t. In the present study, we consider incompressible Newtonian flow, which is a classical assumption in the studies of hydrodynamic. The incompressible hypothesis assumes that the density ρ of the fluid substance depends only on the temperature and in the context, without considering the temperature effect, it remains constant. The Newtonian flow assumes that the shear stress in the fluid is proportional to the local velocity gradient at a rate of μ the dynamics viscosity depending only on temperature. The kinematic viscosity ν appeared in the equation is defined as the ratio of dynamic viscosity and the volume mass $\nu = \mu/\rho$. $\boldsymbol{f}$ is the external force depending on $\boldsymbol{x}$ and t, which could be the perturbation that have been mentioned before. When these equations are supplemented with appropriate boundaries conditions and initial conditions, they are supposed to provide an accurate description of flows. However, there is no exact analytical solution of this system of equations due to it's non-linearity and non-locality.

2.1 Statistical description of turbulence

One of the characteristic features of the turbulent motion is highly unpredictable. Two same realizations could result in completely different values of the dynamic quantities at certain locations and instant. It is necessary to use statistical method to study the turbulence. The use of time-space averaging to statistically study the fluid dynamic quantity of turbulence is a good way to qualitatively analyze some physical phenomenons, because it greatly simplifies the problem by eliminating the time and space dependence of these random variables. Before talking turbulence statistical properties, let's revisit some important assumption.

2.2 Homogeneous and isotropic

In a fully developed turbulence far enough from the boundary, there exists a region of turbulence where the dynamic quantities can be defined as isotropic and homogeneous. The concept of isotropic homogeneous turbulence is an ideal assumption to study the turbulent theory. Let's make an example of

the velocity which is a random variable and the time dependence is not considered here so the velocity is noted as $\boldsymbol{u}(\boldsymbol{x})$. The probability mean value of the velocity denotes as $\langle \boldsymbol{u}(\boldsymbol{x}) \rangle$, it is the average over repeatedly realizations and it should converge to zero, when the statistical sample base is sufficiently large. For a fully developed turbulence, this value should be identical to the space averaging mean value at all point in the space. Whereas, the space averaging mean value of the variable over a control volume A, where $\boldsymbol{x}) \in A$, can be written as

$$\tilde{\boldsymbol{u}}(\boldsymbol{x})) = \frac{1}{A} \int_A \boldsymbol{u}(\boldsymbol{x}) d\boldsymbol{x} \tag{2.3}$$

Secondly, the correlation function of two points in all the domain depends only on the norm of the vector between these two points. Finally, if the mean value of all possible function of the values of the field at several points of space may be obtained by space averaging, it is necessary that the N-dimensional probability density function of the velocity being invariant to any kind of transformation (displacement or rotation or mirror reflection) in the domain. The turbulence field satisfying all the above conditions is referred as isotropic homogeneous turbulence (IHT). Since the isotropic homogeneous turbulence presences superior statistical features, it becomes a popular subject of scientific research to help us have a better understanding of the turbulence. In this paper, we will focus on such isotropic homogeneous turbulence and it will be referred as IHT. Although this turbulence regime can be hardly found or produced in the real life, since fluid in real life must have boundaries even though it is very faraway. It is challenging to experimentally verify the turbulence theory based on IHT.

2.3 Statistical stationary

The definition of the statistical steady state follows the same way of defining the IHT. But this time we focus only on time dependence $\boldsymbol{u}(t)$. Firstly, the time average in a period of time T

$$\tilde{\boldsymbol{u}}(t) = \frac{1}{T} \int_T \boldsymbol{u}(t+\tau) d\tau$$

will converge to the statistical average of velocity $\langle \boldsymbol{u}(t) \rangle$. If $\langle \boldsymbol{u}(t) \rangle$ it is a constant and independent to instant t. The time correlation function of two instant t_1 and t_2 depends only on the time increment $\Delta t = t_2 - t_1$.

$$\langle \boldsymbol{u}(t_1) \boldsymbol{u}(t_2) \rangle = \langle \boldsymbol{u}(0) \boldsymbol{u}(\Delta t) \rangle$$

The fluid field reaches its statistical steady state when the above conditions are satisfied. In order to reaches this statistical steady stat, two conditions must be satisfied. Firstly, the external force needs to inject energy continually into the flow field to balance the energy dissipation lose.

2.4 Correlation functions and characteristic length scales

The IHT presents same interesting statistical features. In this section, the statistical feature in IHT will be presented. The most important feature is the two-point correlation function. In IHT, it depends only the distance between the two separate points. It was introduced by G.I.Taylor in 1935 and is a starting point of statistical approach to study the turbulence. In general form, the two-point correlation tensor separated by a vector $\boldsymbol{r}$ can be noted as

$$R_{ij}(\boldsymbol{r}) = \langle u_x^2 \rangle \left[\rho_u \delta_{ij} + \frac{r}{2} \frac{d\rho_u}{dr} (\delta_{ij} - \frac{r_i r_j}{r^2}) \right] \tag{2.4}$$

where ρ_u is the longitudinal correlation function

$$\rho_u(r) = \frac{R_{xx}(r\vec{e}_x)}{\langle u_x^2 \rangle} = \frac{\langle u(\vec{x}) u(\vec{x} + r\vec{e}_x) \rangle}{\langle u_x^2 \rangle} \tag{2.5}$$

The figure 2.1 is a typical illustration of ρ_u, for $r = 0$, $\rho_u(0) = 1$ which means the velocity perfectly correlated to itself and for $r \to \infty$, $\rho_u(\infty) = 0$ means the velocities at two separated points with a long-distance are compliantly uncorrelated. They are independent in terms of statistical description. The reason why should the correlation function is important is that it is easy to measure with experimental approach. The correlation function can help us to determine an important characteristic length scale in turbulence. Correlation length associated with the progressive decorrelation Integral scale L_{int} of the flow:

$$L_{int} = \int_0^\infty \rho_u(r) dr \tag{2.6}$$

This corresponds to the characteristic scale of the largest turbulent structures of the flow or Macro-scale. Another length scale can be determined by the correlation function, the Taylor micro-scale λ.

$$\frac{1}{\lambda^2} = \left. \frac{d\rho_u^2}{d^2 r} \right|_{r=0}$$

The Taylor scale λ is often used to estimate the average dissipation rate of kinetic energy.

$$\frac{\langle u_x^2 \rangle}{\lambda^2} \sim \langle \left(\frac{\partial u_x}{\partial x} \right)^2 \rangle$$

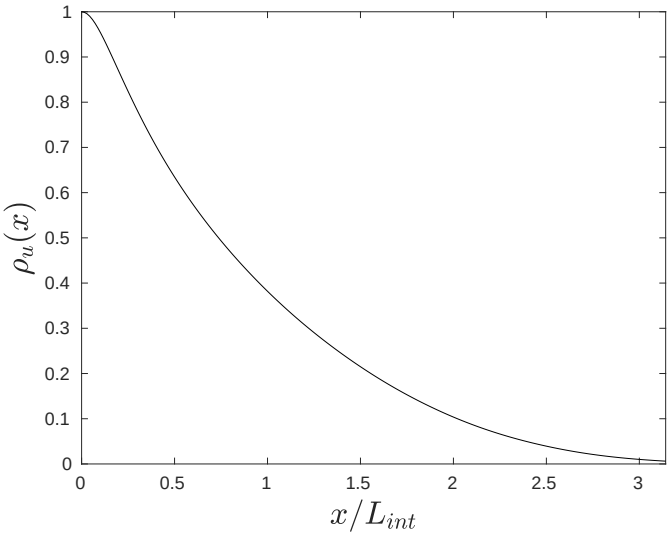

Figure 2.1: The longitudinal correlation function (-) THI field

The dissipation rate is denoted as ε

$$\varepsilon = \frac{1}{2}\left(\frac{\partial u_i}{\partial x_j} + \frac{\partial u_j}{\partial x_i}\right)^2$$

the mean dissipation rate can be estimated as

$$\langle\varepsilon\rangle \sim 15\nu\frac{\langle u_x^2\rangle}{\lambda^2}$$

The Taylor scale is also used as the characteristic scale to define the Reynolds number of fully developed turbulence $Re_\lambda = \frac{u_{rms}\lambda}{\nu}$, which is widely accepted the so-called micro-scale Reynolds number. The Fourier transform of the longitudinal correlation function return to one dimension density spectral of the velocity.

2.5 The Kolmogorov Theory and the Turbulence Intermittency

The idea of energy cascade model in the turbulence is widely accepted and it becomes a basic assumption in turbulence modeling. The concept was initially introduced by Richardson (1922). The fluid volume is being called eddy in this context. In such viewpoint, the turbulence can be considered to

be composed of eddies of different sizes. Eddies of size l_0 have a characteristic velocity u_0 and timescale $\tau_0 = l_0/u_0$. These eddies have energy of order u_0^2. The notion of l_0 means the energy contains scale in this context. The energy transfer in turbulence associated to the breakdown consecutively of large size eddies to smaller size of eddies at a rate of $\varepsilon_{l_0} = u_0^2/\tau_n$. During this process the energy transfer from the large eddies to small eddies. Afterward, these smaller eddies undergo a similar break-up process, and transfer their energy to even smaller eddies. This successive energy cascade or eddies breakdown process will eventually stop where the viscosity effect becomes predominant. At the smallest scale of the turbulence, the energy dissipates into heat under the viscosity. The dissipation rate denoted as ε is assumed to be approximately equal to the energy transfer rate $\varepsilon \sim \varepsilon_{l_0}$. The smallest scale is also referred as dissipative scale is a characteristic scale of turbulence. Under this frame work, Kolomogorov proposed the famous Kolmogorov turbulent theory in 1941. The turbulent theory is based on three hypotheses and one consequence of this hypothesis. The detail of these hypotheses can be found in many references. The introduction of the theory is significant. It provides tools to studies in a universal way the turbulent flow. It has answered some important questions when does this energy cascade process end. At large Reynolds number, the statistical propriety for small scale motion only depends on average dissipation rate $\langle\varepsilon\rangle$ and the kinetic viscosity η. At the smallest scale the fluid inertia forces reach equilibrium with the viscous forces with the Reynolds number based on the dissipative scale equal to unity $Re_\eta = \eta u_\eta/\nu = 1$. η is the dissipative length scale, which is often referred as the Kolmogorov dissipative scale, as well as the time scale associated with the dissipation length scale are defined.

$$\eta = (\nu^3/\langle\varepsilon\rangle)^{\frac{1}{4}}$$

$$\tau_\eta = (\nu/\langle\varepsilon\rangle)^{\frac{1}{2}}$$

The Kolomogorov scale is conventionally used to characterize the turbulence. The Kolmogorov velocity $u_\eta = \eta/\tau_\eta$ and Kolmogorov acceleration $a_\eta = u_\eta/\tau_\eta$ will also be used in the following. The Reynolds number $Re_{l_0} = l_0 u_{l_0}/\nu$ is a measurement of the scale separation, with the assumption of $\langle\varepsilon\rangle \sim u_{l_0}^3/l_0$

$$\eta/l_0 \sim Re^{-\frac{3}{4}}$$

At large Reynolds number $Re_{l_0} \gg 1$, the Kolmogorov scale is much smaller than the energy contained scale. And there exists a sub-range where the characteristic length l satisfying $\eta \ll l \ll l_0$. The sub-range is called as inertia sub-range, where the energy only transfer from large scales to small scales and is not affected by the viscosity ν. Which means that within this range the statistical properties only are affected by $\langle\varepsilon\rangle$. The study of the second order moment of velocity increment or structure function is a good illustrate

the Kolmogorov similarity hypotheses [30]. Later Kolmogorov hypothesis is refined [31, 32] by replacing $\langle\varepsilon\rangle$ by local averaged value of dissipation rates $\varepsilon_r(x)$ define in equation (2.7). The conditional probability distributions for the velocity increments depends on the local average dissipation rate ε_r.

$$\varepsilon_r(x) = \frac{3}{4\pi r^3}\int_{|h|<r}\varepsilon(x+h)dh \tag{2.7}$$

For a length scale $r \ll l_0$, the variable $\varepsilon_r(x)$ is a random variable and presents very large fluctuations and is heterogeneous. And also the small scale component of turbulent flow must also be affected by the probability distribution of ε. It has been suggested to have a log-normal distribution form. The experimental observation also suggests that the turbulence is highly intermittent [33]. The figure 2.2 shows a typical dissipation snapshot of a IHT field. We can see that, in most of the area of the field, there is no dissipation while the dissipation concentrates on a small area. The dissipation rate in the strong dissipative region can reach to five times or even larger of the root-mean-square of the dissipation rate. This means that the dissipation rate presents a very large fluctuation through the area. Now imagining a bubble drift through the boundary between strongly dissipative area and weak dissipative area, it will experience a very strong acceleration. The figure 2.3 shows that following a fluid tracer, the evolution of the instantaneous dissipation rate with time. We can find that the dissipation rate can occasionally be 100 times to its root-mean-square. The figure 2.4 shows the correlation function between two points in the space. It shows a correlation distance of order integral scale. This implies that the dissipation rate depends locally on the large scale motion of the fluid. The intermittency is mainly affected by the small-scale motion of the turbulence or namely the dissipation quantities, the Lagrangian velocity increments with a separation time scale τ in the space $\Delta_\tau \boldsymbol{u}$, for example, presents a non-Gaussian behavior in the *pdf* and the non-Gaussian behavior increased with decreasing scale [17, 18]. The intermittency of the turbulence is expected to be introduced to bubble motion by the interaction of the bubble to the small scale motion.

2.6 Stochastic characteristic of dissipation rate

As the turbulent small scale components depend on the local dissipation rate, we consider the statistical feature of the local dissipation rate ε_r. Based on the theory of self-similar breakdown of turbulent eddies model, introduced by [34]. $\varepsilon_0 = \langle\varepsilon\rangle$ is the mean energy dissipation rate in a cube with length of a typical turbulence large-eddy of characteristic length L_0. And then the large-eddy breakdown successively into n smaller sub-cube with n an

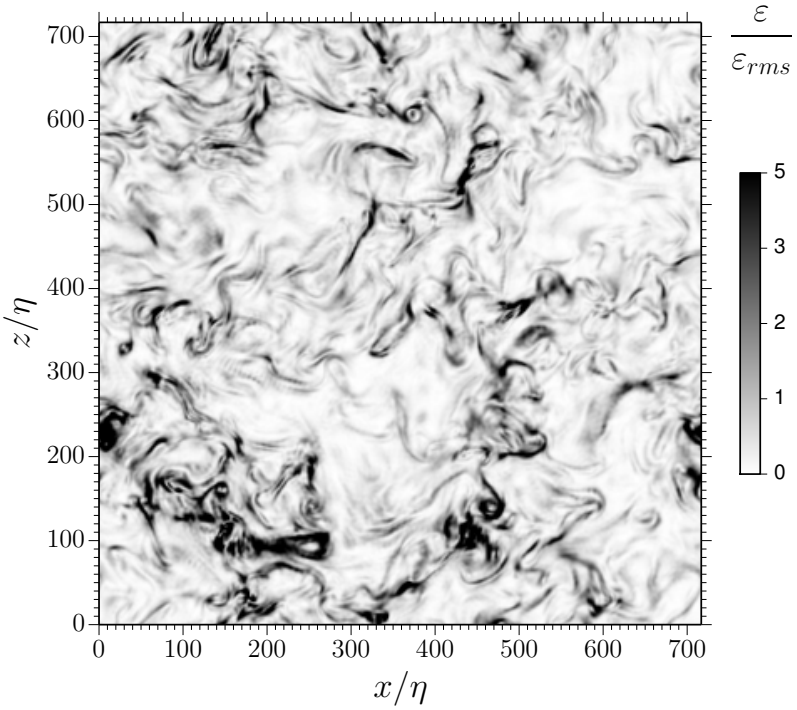

Figure 2.2: A snapshot of the dissipation rate normalized by its root-mean-square value on a xz-plan of turbulent fluid field with $Re_\lambda \simeq 200$

arbitrary number. At the j step of breakdown the length of j-order cube is $L_j = L_0 n^{-j/3}$. Let ε_j be the dissipation rate averaged over the volume of one cube of order j. Following the self-similarity, when j it is sufficiently large the variable ε_j is independent of j. Provided that the value of the ε_{j-1} is fixed, the $\alpha_j = \varepsilon_j/\varepsilon_{j-1}$ is a random variable independent of j.

$$\varepsilon_j = \varepsilon_0 \alpha_1 \alpha_2 ... \alpha_j$$

and apply a logarithm operation on both side of the equation

$$ln\varepsilon_j = ln\varepsilon_0 + \sum_{i=1}^{j} ln\alpha_i$$

Based on the central limit theorem the sum of independent random variables will have an approximately normal probability distribution with mean $\mu_j = -\sigma_j^2/2$ (to make sure $\langle \varepsilon_j \rangle = \langle \varepsilon \rangle = \exp(\mu_j + \sigma_j^2/2)$) and variance σ_j^2 depending on the deepness of the cascade process L/r_j .

The local averaged dissipation rate ε_r, for $r \ll l_0$ is therefore suggested having a log-normal probability distribution function Eq. (2.8). Which

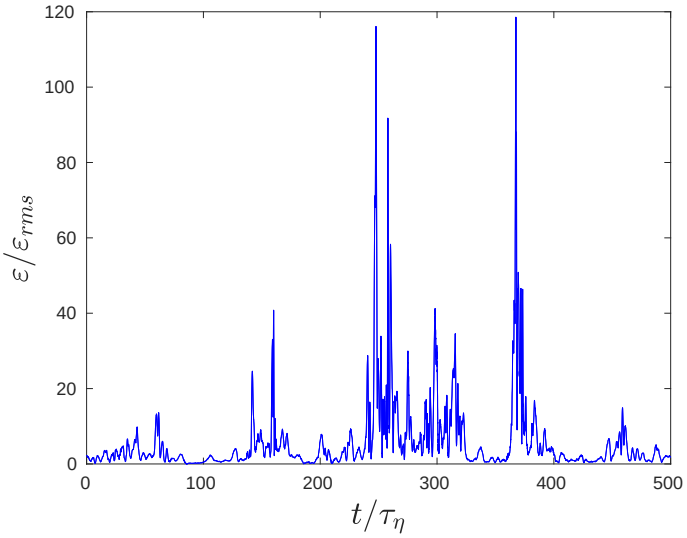

Figure 2.3: The dissipation rate at the position of a fluid tracer normalized with its root-mean-square value varies with time of turbulent with $Re_\lambda \simeq 200$.

means that the $\ln \varepsilon_r$ distribute in a normal fashion and the variance for large Reynolds number is

$$\sigma_r^2 = A(x,t) + \mu \ln(L/r)$$

where $A(x,t)$ depends on the large scale motion and L is the external turbulent length scale r is the length in the inertial range, μ is a constant.

$$pdf_{\varepsilon_r}(\varepsilon) = \frac{1}{\sqrt{2\pi\sigma_r^2}\varepsilon} \exp\left[-\frac{(\ln \varepsilon - \mu_r)^2}{2\sigma_r^2} \right] \tag{2.8}$$

2.7 Stochastic process to model dissipation rate

Inspire by the Kolmogorov theory, the dissipation rate can be modeled by an Orstein-Ulenbeck process [23, 16, 24]. The random variable $\chi = (\ln \varepsilon_*)$ have a Gaussian distribution with variance σ_χ^2 and mean value μ_χ and the stochastic process gives

$$d\chi = -(\chi - \mu_\chi)\frac{d\tau}{T_\chi} + \sqrt{\frac{2\sigma_\chi^2}{T_\chi}} dW(\tau) \tag{2.9}$$

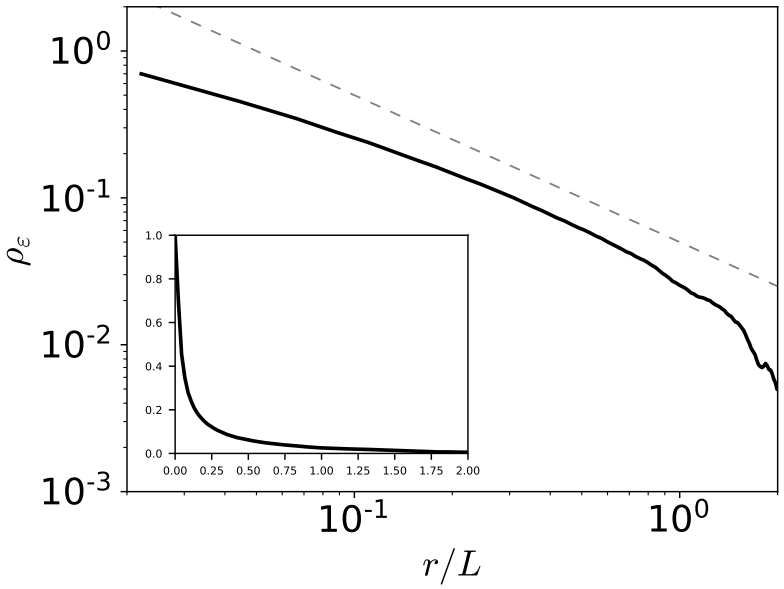

Figure 2.4: The correlation function of the dissipation rate for turbulence with $Re_\lambda \simeq 200$ presented in log-log scale, in the insertion is the normal scale

with $dW(\tau)$ the increments of the Winner process with $\langle dW(\tau)\rangle = 0$ and $\langle dW(\tau)^2\rangle = d\tau/2$. The increments of Winner process gives independent variable for different realizations. The first term on the right hand of Eq. (2.10) related to a time scale T_χ provides the correlation with the previous time step. The auto-correlation time of χ is controlled by T_χ and the auto-correlation function of χ is exponential. In the figure 2.5, the *pdf* of χ and the Lagrangian autocorrelation function ρ_χ is presented. The *pdf* is a Gaussian distribution and the ρ_χ can be fitted by $\exp(-t/T_\chi)$.

Put $\chi = (\ln \varepsilon_*)$ into the equation (2.9) and using the Itô transform of the stochastic differential equation we have

$$\frac{d\varepsilon_*}{\varepsilon_*} = (-\ln \varepsilon_* + \mu_\chi + \sigma_\chi^2)\frac{d\tau}{T_\chi} + \sqrt{\frac{2\sigma_\chi^2}{T_\chi}}dW(\tau) \tag{2.10}$$

The mean value of $\langle \varepsilon_* \rangle = \langle \varepsilon \rangle = \exp(\mu_\chi + \sigma_\chi^2/2)$. Then the parameter $\mu_\chi = \ln\langle\varepsilon\rangle - \sigma_\chi^2/2$ and $\sigma_\chi^2 \sim \ln(L/\eta)$ represent the depth of the turbulent cascade .

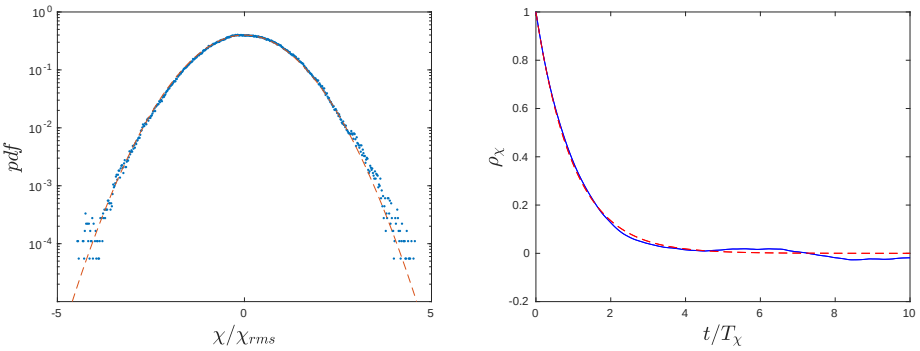

Figure 2.5: (left) The *pdf* of χ model by the Orstein-Ulenbeck process and compared to a (- -) Gaussian distribution. (right) The autocorrelation function of χ compared to an exponential function (–) is the curve of $\exp(-t/T_\chi)$

Chapter 3

Point particle approach

The Lagrangian point particle approach has a long history in numerical studies of dispersed multi-phase turbulent flow. The particle in such context generically denotes an element of the dispersed phase. The particle can physically correspond to solid particles, droplets, bubbles or material points. Each of these objects is primarily characterized by its density ρ and viscosity μ compared to the carrier phase:

$$\Phi_\rho = \rho_b/\rho_f \quad , \; \Phi_\mu = \mu_b/\mu_f \tag{3.1}$$

Typically for heavy solid particles $\Phi_\rho \gg 1$ and $\Phi_\mu \gg 1$ while for bubbles $\Phi_\rho \ll 1$ and $\Phi_\mu \ll 1$ and for a fluid particle one has $\Phi_\rho = \mathcal{O}(1)$ and $\Phi_\mu = \mathcal{O}(1)$. It should be remarked that while a dirty bubble in a contaminated liquid flow behaves like a rigid particle, a clean bubble in an uncontaminated liquid behaves quite differently, the primary difference is in the mobility of the surface of the sphere. This will affect the drag and lift coefficients. Conventionally, a clean bubble often refers to a bubble with a free stress at the interface, and a contaminated bubble refers to a bubble with an immobilized surface.

In the point particle approach (also called Euler-Lagrangian approach), the evolution of the dispersed phase is given by Newton's equation. To close this momentum balance, one need to provide an expression to calculate the various forces acting on each particle. The force acting on the particles can be decomposed into hydrodynamic force, which depends on the fluid velocity fields and its derivatives in the vicinity of the particle, and non-hydrodynamic force, which are independent of the velocity field. Thus, to compute the hydrodynamic forces, it is necessary to first compute the Eulerian fluid fields, thanks to DNS or LES, and then interpolate the value of the fields at the particle position.

The hydrodynamic force is formally the integration of fluid action (shear stress and pressure) on the surface of the particle. However, in the point particle approach the flow is not solved around the particle and we do not have access directly to the fluid stress applied on the particle. Therefore, it is necessary to use effective relations to obtain an estimation of the hydrodynamic force on a particle from the value of the resolved flow field at the particle's position. Obtaining such expressions with general validity in turbulent flow remains challenging. The usual approach is to restrict the studies to sufficiently small particles in order to consider that the flow around them is quasi-homogeneous and stationary, so that the expression obtained analytically for particles in such condition can be used. Following [5], the forces on a particle can be decomposed into several contributions

$$m_b \frac{d\boldsymbol{u}_b}{dt} = F_D + F_{Tchen} + F_{MA} + F_L + F_H + F_g \tag{3.2}$$

with bubble velocity $\boldsymbol{u}_b$, drag forces F_D and history force F_H are viscosity induced force. Force Tchen F_{Tchen} and added-mass force F_{MA} are caused by the fluid inertia, and the effect together of these two forces will be called fluid inertia force. The lift force F_L is due to the non-uniformity of surrounding flow field. And the buoyancy force F_g is induced by gravity.

Bellow we discuss each of these forces and recall usual expression for them. In order to generalize the notions, in this chapter, $\boldsymbol{u}_b$ is the generalize expression of particles (bubbles, droplets and solid particles), $\boldsymbol{u}_f$ is the generalize expression of the fluid velocity at the particle position. The Reynolds number based on the particle scale is noted as $Re_b = \frac{d_b|\boldsymbol{u}_f - \boldsymbol{u}_b|}{\nu}$ with $d_b = 2R$ is the bubble diameter.

3.1 Drag force

For a particle moving with a velocity $\boldsymbol{u}_f$ in uniform flow of velocity $\boldsymbol{u}_b$, the drag force is generally expressed as:

$$F_D = C_D \frac{\pi R^2}{2} \rho_f |\boldsymbol{u}_f - \boldsymbol{u}_b| (\boldsymbol{u}_f - \boldsymbol{u}_b) \tag{3.3}$$

The force orientation is given by $\boldsymbol{u}_f - \boldsymbol{u}_b$. C_D is the drag coefficient. It is a function Re_b, Φ_μ and Φ_ρ. For the case $Re_b \ll 1$ called Stokes regime, a solution is provided by Stokes in 1851 and has been extended later by Taylor and Acrivos (1964) to fluid particles. It is often referred as the Stokes solution.

$$F_D = 6\pi\mu R \frac{2 + 3\Phi_\mu}{3 + 3\Phi_\mu} (\boldsymbol{u}_f - \boldsymbol{u}_b) \tag{3.4}$$

which gives

$$C_D = \begin{cases} \frac{24}{Re_b} & \text{for} \quad \Phi_\mu \gg 1 \\ \frac{16}{Re_b} & \text{for} \quad \Phi_\mu \ll 1 \end{cases} \tag{3.5}$$

When Re_b increases, the Stokes solution will be far from the reality and empirical expression for the drag coefficient will be used. The drag coefficient C_D will be corrected with a function of Re_b and ϕ_μ. For small inertial effects $Re_b < 1$, Oseen (1910) has developed analytically the drag coefficient by linearizing the convection term of Navier-Stokes equations $U\nabla U = U_\infty \nabla U$. The drag coefficient is then [35]

$$C_D = \frac{24}{Re_b}\left[1 + \frac{3}{16}\left(\frac{2+3\Phi_\mu}{3+3\Phi_\mu}\right)Re_b + \frac{9}{160}\left(\frac{2+3\Phi_\mu}{3+3\Phi_\mu}\right)^2 Re_b^2 lnRe_b + \mathcal{O}(Re_b^2)\right] \tag{3.6}$$

First let's consider the case of a bubble with $Re_b \gg 1$ and assuming that the boundary layer do not detach (corresponding clean spherical bubble case), [36] have resolved an analytical coefficient in potential flow and later modified by [37].

$$C_D = \frac{48}{Re_b}[1 - 2.211 Re_b^{-1/2} + \mathcal{O}(Re_b^{-5/6})] \tag{3.7}$$

An empirical correlation of drag coefficient for bubbles (slip interface with $\Phi_\rho = 0$ and $\Phi_\mu = 0$) is proposed by asymptotically matching the C_D to low and high Re_b (for $Re_b < 1$ Eq. (3.6) and for $Re_b \gg 1$ Eq (3.7)):

$$C_D = \frac{16}{Re_b}\left[1 + \left(\frac{8}{Re_b} + \frac{1}{2}(1 + \frac{3.315}{Re_b^{1/2}})^{-1}\right)\right] \tag{3.8}$$

The correlation of [38] has been confirmed by other numerical simulation and is applicable for any value of Re_b for a clean bubble.

For solid particles the problem is more complicated, because the boundary condition is no-slip which means it is easy to have a detachment in the boundary layer. For $Re_b < 800$, Schiller and Nauman (1978) [39] proposed an empirical correlation of the drag coefficient for solid particles based on experiments:

$$C_D = \frac{24}{Re_b}(1 + 0.15 Re_b^{0.687}) \tag{3.9}$$

The drag force computed with these expressions of the drag coefficient is often called no-linear drag while the Stokes solution is called linear drag. In figure (3.1), the evolution of the drag coefficient for solid particles and for clean bubbles is plotted. We notice that the drag coefficient for a sphere with no-slip interface increases faster with the increasing of Re_b compared to the drag coefficient of a clean bubble. In Chapter 6, we will discuss the influence of these no-linear drag forces.

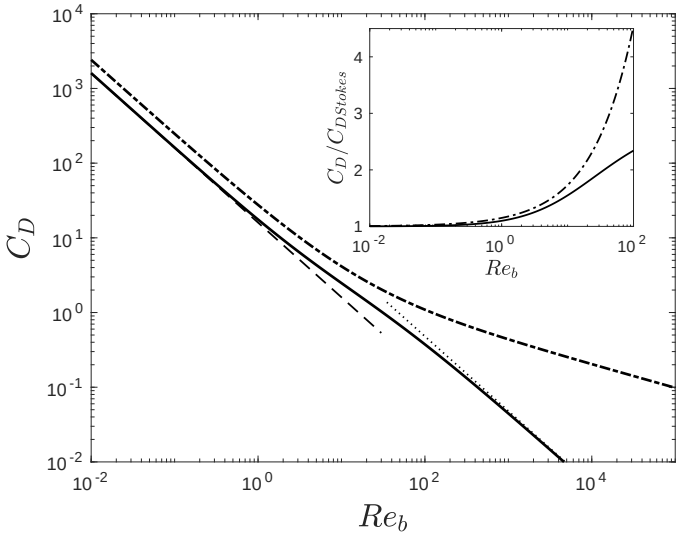

Figure 3.1: The drag coefficient versus Re_b (-) Eq. (3.8) (- ·) Eq. (3.9) (- -) clean bubbles in Stokes regime (· · ·) Stokes solid particles Eq. (3.7). Insert: compares the non-linear drag law for (-) clean bubbles and (- ·) solid particles respectively Eq. (3.8) and Eq. (3.9) to their respective Stokes drag law Eq. (3.5)

3.2 History force

The history force or Basset-Boussinesq force is an hydrodynamic force induced by viscosity and the no-stationary relative movement of the particle in the surrounding fluid. It describes the force due to the lagging boundary layer development with changing relative velocity (acceleration) of bodies moving through a fluid. The Basset term accounts for viscous effects and addresses the temporal delay in the boundary layer development as the relative velocity changes with time. In Stokes regime $Re_b \ll 1$ and uniform flow field, for a spherical body the history force can be expressed as

$$F_H = 6\pi\mu_f R \int_0^t \mathcal{K}(t-\tau)(\frac{\partial \boldsymbol{u}_f}{\partial t} - \frac{d\boldsymbol{u}_b}{dt})d\tau \tag{3.10}$$

or a more general form in non-uniform flow condition [40]

$$F_H = 6\pi\mu_f R \int_0^t \mathcal{K}(t-\tau)(\frac{\partial \boldsymbol{u}_f}{\partial t} + \boldsymbol{u}_b.\nabla \boldsymbol{u}_f - \frac{d\boldsymbol{u}_b}{dt})d\tau \tag{3.11}$$

where $\mathcal{K}(t-\tau)$ is the kernel which depends on the properties of the particle. For solid particles, Boussinesq and Basset (1885) have calculated analytically

the expression of the kernel for a solid spherical particle with a limit of $Re_b \ll 1$.

$$\mathcal{K}(t-\tau) = \frac{R}{\sqrt{\pi\nu(t-\tau)}}$$

For a clean bubble ($\Phi_\mu = 0$) and $Re_b < 1$, the expression of the kernel is [41]

$$\mathcal{K}(t-\tau) = \frac{3}{4}\exp\left[\frac{9\nu(t-\tau)}{R^2}\right] erfc\left[\sqrt{\frac{9\nu(t-\tau)}{R^2}}\right]$$

[42] have recently proposed an expression that makes possible the description of the history kernel for a fluid particle with any value of Φ_μ. [43] argues that the history force for a bubble is negligible compared to the drag force when $Re_b > 50$. And usually in numerical research, the history force is neglected for a reason of simplification as we do in the present research. Nevertheless, the historical force effect might be important for the motion of the bubble with $St \sim 1$, for fluid particles of any viscosity ratio

3.3 Fluid inertia force

F_{AM} and F_{Tchen} are two hydrodynamic forces induced by inertia effects in unsteady and non-uniform flows.
The added mass force writes

$$F_{AM} = C_M \mathcal{V}_b \rho_f \left(\frac{D\boldsymbol{u}_f}{Dt} - \frac{d\boldsymbol{u}_b}{dt}\right) \tag{3.12}$$

where $\mathcal{V}_b$ is the bubble volume. The added-mass coefficient C_M depends on the geometry of the particle, and for a spherical particle $C_M = 0.5$. The Tchen force F_{Tchen} is related directly to the fluid acceleration as:

$$F_{Tchen} = \mathcal{V}_b \rho_f \frac{D\boldsymbol{u}_f}{Dt} \tag{3.13}$$

If we write expression (3.12) and (3.13) into the force balance equation (3.2) and move the term containing the particle acceleration $\frac{d\boldsymbol{u}_b}{dt}$ to the left side we have

$$(m_b + C_M m_f)\frac{d\boldsymbol{u}_b}{dt} = (C_M + 1)m_f \frac{D\boldsymbol{u}_f}{Dt} + \sum other forces \tag{3.14}$$

with $m_b = \rho_b \mathcal{V}_b$ and $m_f = \rho_f \mathcal{V}_p$. The term containing $\frac{D\boldsymbol{u}_f}{Dt}$ depends only on the fluid inertia force at the position of the particle and will be called fluid inertia force in this manuscript. We can see that if $\Phi_\rho \gg 1$, $(m_b + C_M m_f) \simeq m_b$, and the added mass has no effect. On the contrary, if $\Phi_\rho \ll 1$, the fluid inertia effect is much more important. This is the situation of interest in the present study.

3.4 Lift force

The lift force is induced by the velocity gradient (or vorticity) in the flow field. Often it is referred as shear-induced lift force to distinct from other lift effects. The general expression of the lift force on a spherical particle in an steady simple shear flow can be written as

$$F_L = C_L \rho_f \mathcal{V}_b (\boldsymbol{u}_f - \boldsymbol{u}_b) \times \boldsymbol{\Omega}_f \tag{3.15}$$

where $\boldsymbol{\Omega}_f = \nabla \times \boldsymbol{u}_f$ is the vorticity, C_L is the lift coefficient. There have been few experimental studies able to measure the lift coefficient for a bubble or rigid particle in undistributed rotational flow or simple shear flow. In steady shear flows the coefficient is related to Re_b and the normalized shear $Sr = \frac{R|\boldsymbol{\Omega}_f|}{|\boldsymbol{u}_f - \boldsymbol{u}_b|}$.

For Stokes regime, there is no lift ($C_L = 0$).
For $Re_b < 1$ (moderate inertia), [44] has proved analytically that the coefficient can be expressed as (3.16) with the limit of $\sqrt{Re_b Sr} \ll 1$

$$C_L^{Re_b<1} = \frac{6}{\pi^2} \frac{2 + 3\Phi_\mu}{2 + 2\Phi_\mu} \frac{J(\alpha)}{\sqrt{Re_b Sr}} \tag{3.16}$$

with $\alpha = \sqrt{Sr/Re_b}$ and

$$J(\alpha) = \frac{J(\infty)}{(1 + 0.2\alpha^{-2})^{3/2}}$$

In the limit of $\Phi_\mu \to \infty$ and $\alpha \to \infty$ an analytic lift force of a solid particle can be found at $J(\infty) = 2.255$ and recover the Saffman solution [45]. The numerical simulations have proved this expression is appropriate up to $Re_b \sim 1$.
For large Reynolds numbers, $Re_b > 50$, the lift coefficient of a clean spherical bubble (particle with $\Phi_\mu \ll 1$) depends only on the Reynolds number and the empirical expression is [46]

$$C_L^{Re_b>50} = \frac{1}{2} \frac{1 + 16 Re_b^{-1}}{1 + 29 Re_b^{-1}} \tag{3.17}$$

The expression asymptotically approaches to the analytical solution of Auton for inviscid limit $C_L = 0.5$. Providing the coefficient expression for different range of Re_b, an expression for spherical bubble matching asymptotically the low (3.16) and high Reynolds number (3.17) is proposed to approximately extend the applicable range of the lift coefficient expression [46]:

$$C_L = \sqrt{(C_L^{Re_b<1})^2 + (C_L^{Re_b>50})^2} \tag{3.18}$$

Although, all the above C_L expressions are based on simple shear flow, the lift force expression in the equation (3.15) has been shown to correctly describe lift effects. In the following, the lift force coefficient of Eq. (3.18) will be used to describe the lift force over a wide range of Reynolds number.

3.5 The limit of the point particle approach

Using these force coefficient expressions along with the buoyancy force $(m_b - m_f)\boldsymbol{g}$, with $\boldsymbol{g}$ the gravity in equation (3.2) and regroup certain terms, we obtain the trajectory equation:

$$\begin{aligned}(m_b + m_f C_M)\frac{d\boldsymbol{u}_b}{dt} &= C_D\frac{\pi R^2}{2}\rho_f|\boldsymbol{u}_f - \boldsymbol{u}_b|(\boldsymbol{u}_f - \boldsymbol{u}_b)\\ &+ m_f(1 + C_M)\frac{D\boldsymbol{u}_f}{Dt}\\ &+ C_L m_f(\boldsymbol{u}_f - \boldsymbol{u}_b)\times\boldsymbol{\Omega}_f\\ &6\pi\mu_f R\int_0^t \mathcal{K}(t-\tau)(\frac{\partial \boldsymbol{u}_f}{\partial t} - \frac{d\boldsymbol{u}_b}{dt})d\tau\\ &+ (m_b - m_f)\boldsymbol{g}\end{aligned} \tag{3.19}$$

In this work, we focus on the case of a bubble, air bubble in water for example. Bubble is a specific case of the dispersed phase. First, when the liquid is pure enough, it has the possibility to slip along the surface of the bubbles, in contrast to the flow past rigid bodies where the no-slip condition is imposed. Second, owing to the very weak relative density of bubbles compared to that of the liquid, almost all the inertia is contained in the liquid, making inertia-induced hydrodynamic forces F_{Tchen} and F_{AM} particularly important in the prediction of the bubble motion. Third, the bubble is always assumed to be spherical, which is true only when the bubble is small enough that the surface tension can predominate over other forces on the bubble, typically for air bubbles in water with $d_b < 1(mm)$. All these considerations together imply that $\mu_f \gg \mu_b$, $m_f \gg m_b$ and $C_M = 0.5$. m_b in the equation can be neglected and dividing by $m_f C_M$ on both side and neglecting the historical force, the equation of motion for a bubble per unit of displaced fluid writes

$$\boldsymbol{a}_b = \frac{d\boldsymbol{u}_b}{dt} = \frac{\boldsymbol{u}_f - \boldsymbol{u}_b}{\tau_b} + 3\frac{D\boldsymbol{u}_f}{Dt} + 2C_L(\boldsymbol{u}_f - \boldsymbol{u}_b)\times\boldsymbol{\Omega}_f - 2\boldsymbol{g} \tag{3.20}$$

where $\boldsymbol{a}_b$ is the bubble acceleration and τ_b is the bubble relaxation time scale $\tau_b = \frac{2d_b^2}{3\nu C_D Re_b}$. Physically, it is the time necessary for a bubble to smooth out the relative velocity. The general assumptions of using this equation to track bubble motion in turbulent flow are:

- The fluid at the scale of the bubble must be uniform or quasi-uniform. This demands that the bubble size must be much smaller than the Kolmogorov $d_b \ll \eta$. In practical, this limit could be extended up to $d_b \sim 10\eta$ [27]. Because in practical situations the smallest structure of turbulence has a length scale of order 10η.

- Stokes regime: The Reynolds number calculate with the bubble size is much smaller than unity $Re_b = d_b|\boldsymbol{u}_f - \boldsymbol{u}_b|/\nu \ll 1$. This is the Stokes regime of the bubble. For $Re_b = 0$ the lift force is zero. This leads to a further simplification of Eq. (3.20)

$$\frac{d\boldsymbol{u}_b}{dt} = \frac{\boldsymbol{u}_f - \boldsymbol{u}_b}{\tau_b} + 3\frac{D\boldsymbol{u}_f}{Dt} - 2\boldsymbol{g} \tag{3.21}$$

  The drag coefficient is then $C_D = 16/Re_b$, the solution for a bubble in Stokes regime. The drag term is thus linear, and the relaxation time depends only on the bubble size and the viscosity of the fluid:

$$\tau_b = \frac{d_b^2}{24\nu} \tag{3.22}$$

  This assumption actually is a consequence of the first one, because for a bubble when the diameter is much smaller than the Kolmogorov scale $d_b \ll \eta$, the time that takes a bubble to relax fluid velocity is much smaller compared to the characteristic time scale of the fluid field. With the Stokes number defined as $St = \frac{\tau_b}{t_\eta} = \frac{d_b^2}{24\eta^2}$, we can see that St converge to zero at order of $(d_b/\eta)^2$. The relative velocity is suppose to be of order the Kolmogorov velocity $|u_f - u_b| \ll u_\eta$ with $u_\eta = \eta/\tau_\eta$. Then we can prove that $Re_b \ll Re_\eta = 1$.

The present study does not consider the effect of the influence of the bubble to the fluid field. Conventionally this is called "one-way coupling" of point particle approach. And this is valid when the concentration is sufficiently diluted that the bubble cannot feel the existence of the others. For a specific situation where the turbulent intensity is very intense, where the Kolomogrov acceleration is much more important than the gravity $a_\eta = u_\eta/\tau_\eta \gg |\boldsymbol{g}|$, the gravity can also be neglected. By neglecting the gravity, the motion of the bubble does not depend on direction and this provides a convenient situation for statistical study of the acceleration. All these assumptions are considered to conduct the study presented in Chapter 5.

In Chapter 6, we will discuss the influence of the non-linear drag force effect by using equation (3.21) where the relaxation time will be modified by considering different drag laws. In Chapter 7, the effect of buoyancy will be considered, while in Chapter 8 the effect of the lift force is discussed.

Chapter 4

Numerical simulation

This chapter is devoted to present the feature of the numerical solver used in this study. The solver is designed to obtain a numerical simulation of the evolution of a dispersed phase in an homogeneous and isotropic turbulent flow. It uses a spectral method to solve Navier-Stokes equations enforcing the constraint of divergence free for the velocity fields in a 3D box with periodic boundary conditions. The evolution of the bubble phase is obtained by the point particle approach. This solver has been used for several previous researches on numerical studies of heavy or light particles dispersed in turbulence [47, 24, 48, 49].

4.1 Eulerian solver

The Eulerian solver is designed to use spectral discretizations to solve Navier-Stokes (N-S)equations enforcing the divergence free constraint for the velocity fields in 3D box with periodic boundary conditions. The use of the periodic boundary conditions enable the possibility to use Fourier modes representation for the various fields leading to a very accurate and efficient way to compute the space derivative by assuming the smoothness of the physical space. It has been used extensively in the numerical study of IHT and proved to be efficient as well as having very good accuracy [50].

The $\hat{u}$ and $\hat{p}$ are the Fourier coefficients of the velocity and pressure fields, respectively. The Fourier coefficients are obtained with the fast Fourier transform algorithm. In Fourier space, the N-S equations Eq. (2.1) and Eq. (2.2), become

$$\mathrm{i}k_i\hat{u}_i = 0 \tag{4.1}$$

$$\partial_t \hat{u}_i = -\mathfrak{i} k_j \hat{U}_{ij} - \mathfrak{i} k_i \hat{p} - \nu k^2 \hat{u}_i + \hat{f}_i \tag{4.2}$$

with $\mathfrak{i}^2 = -1$ and k_j is the wave number in three directions $i, j = (1, 2, 3) = (x, y, z)$ and $k^2 = k_j k_j$, the repeated indices implicitly implying the summation (Einstein notations). $\hat{U}_{ij} = \widehat{u_i u_j}$ is the non-linear convective term. This term is obtained with pseudo-spectral approach [50, 51]. It is more efficient compared to a direct calculation of the convolution term $\hat{U}_{ij} = \hat{u}_i \star \hat{u}_j$. The pseudo-spectral technique requires an order of $3N^3 log_2 N^3$ operations to compute the non-linear term, while the direct computation of the convolution requires an order of $(N^3)^2$ operations.

The strategy is first to compute the $u_i u_j$ in the physical space. Then we compute the fast Fourier transform (FFT) $\hat{U}_{ij} = \widehat{u_i u_j}$ and then multiply $\mathfrak{i} k_j$. The problem is that the product $u_i u_j$ contained mode of wave length smaller than u_i and the subsequent FFT is prone to introduce aliasing error. It is essential to remove the aliasing since all the modes (even at large wavelength) can be affected. A de-aliasing techniques have been proposed to remove the aliasing error: zero padding 3/2-rule [52]. In practice the FFT are computed with the library P3DFFT [53], and we use the implicit zero-padding technique consisting of adjusting the size of the arrays to only keep meaningful terms, the other modes, which would have been set to zero, are discarded. This results in a significant reduction in computational time.

The pressure term can be eliminated by using divergence free constrain of the velocity. Taking the divergence of the Navier-Stokes equations, we obtain

$$\hat{p} = -\frac{k_j k_i}{k^2} \hat{U}_{ij} - i \frac{k_i}{k^2} \hat{f}_i \tag{4.3}$$

Substituting for $\hat{p}$ into the momentum equation (4.2), we have

$$\partial_t \hat{u}_i = -\nu k^2 \hat{u}_i + P_{il}(\hat{f}_l - \mathfrak{i} k_j \hat{U}_{lj}) \tag{4.4}$$

with the *projector* operator

$$P_{il} = \delta_{il} - \frac{k_i k_l}{k^2} \tag{4.5}$$

The viscous term is quite straightforward to compute in the spectral domain. The forcing term is used in this context to introduce kinetic energy to maintain the statistical stationary state of turbulent flow. The strategy is to force only the largest scale of the flow. Following the method disused in [54], the Fourier coefficient of the forcing term is proportional to the Fourier coefficient of the velocity:

$$\hat{f}_i(\vec{k}) = \alpha(k) \hat{u}_i(\vec{k}) \tag{4.6}$$

with the scale dependent coefficient α computed at each time step by the following relation:

$$\alpha(k) = \begin{cases} (\sqrt{E_{int}(k)/E(k)} - 1)/T & \text{for} \quad k\,L/2\pi < 3 \\ 0 & \text{for} \quad k\,L/2\pi > 3 \end{cases} \tag{4.7}$$

with k the modulus of the wavevector $\vec{k}$ and $E_{int}(k)$ is the user defined target energy density spectra, and $E(k)$ is the computed velocity energy spectra. As apparent from this definition of the forcing term, when the energy density of the large scales is smaller than the objective energy defined by the user, this forcing term will inject energy. On the other hand, when the computed energy density is larger than the target, the work done by the force will be negative. Note that the force term is only active at large scale.

The injected energy fluctuates over its average value that keeps the flow field in statistically steady state. These energy fluctuations distributed to all turbulent excited length scales and the spectrum of these fluctuations is shown to have a universal inertial range, proportional to the energy spectrum. Further discussion can be found in [49].

The time advancing is using 2-nd Adams Bashforth (AB2). The idea is based on approximating the integrate with a polynomial within the interval (t_{n-1}, t_{n+1}) using a k^{th} order polynomial. $\Delta t_n = t_{n+1} - t_n$ and $\Delta t_{n-1} = t_n - t_{n-1}$

$$\hat{u}_i^{n+1} = \hat{u}_i^n + \left[\partial_t \hat{u}_i^n \left(1 + \frac{0.5\Delta t_n}{\Delta t_{n-1}}\right) - \partial_t \hat{u}_i^{n-1} \frac{0.5\Delta t_n}{\Delta t_{n-1}}\right] \Delta t_n \tag{4.8}$$

The terms $\partial_t \hat{u}_i^n$ and $\partial_t \hat{u}_i^{n-1}$ are obtained from the addition of the previously discussed terms according to the Navier-Stokes equations Eq. (4.4). The AB2 method requires the information from the $(n-1)^{th}$ and the n^{th} steps to find the solution at the $(n+1)^{th}$ step. This method is explicit so it is conditionally stable.

The algorithm in one time step at instant t_n:

- Begin with computing the convection term $\rightarrow$ de-aliasing $\rightarrow$ saving it with a separate copy for further computing the material acceleration $\rightarrow$ adding to the $\partial_t \hat{u}_i^n$ which are initially set to zero,
- computing viscous terms and adding to the $\partial_t \hat{u}_i^n$,
- computing the forcing term and adding to the $\partial_t \hat{u}_i^n$
- doing time advancing to update the velocity $\hat{u}_i^{n+1}$ at the instant t_{n+1},

- projecting the velocity with Eq. (4.5) and doing a de-aliasing operation once more to make sure to remove all the wave-numbers that cause aliasing error,
- transferring the velocity in physical space and computing the acceleration.

4.2 The large eddy simulation

In the large eddy simulation approach only the large scales of the flow are explicitly computed while the influence of the small discarded scales on the resolved scales of the flow are accounted for through a model. The primary advantage of the LES is the reduced computational cost compared to a numerical simulation in which all the scales of the flow are properly resolved (usually called Direct Numerical Simulation) since one can use a much coarser computational grid. On the other hand, the spatio-temporal fluctuations of the velocity fluid corresponding to the scales above the cutoff filter can be accurately predicted by the LES approach. Typically, the characteristic size of the cutoff filter is of the order of the mesh size and should lie in the inertial range. The purpose of the subgrid scale model is to ensure the correct energy flux from the resolved scales of the flow to the unresolved one (and thus the proper mean dissipation rate.) Most models rely on the concept of the eddy viscosity.

The concept is based on the decomposition of the velocity:

$$u_i = \overline{u_i} + u_i' \tag{4.9}$$

where $\overline{u_i}$ is filtered velocity or large scale motion resolved in LES and u_i' is the residual velocity representing small scale motion which is unresolved in LES.

$$\overline{u_i}(x,t) = \int u_i(\xi,t) G_\Delta(\xi - x) d\xi \tag{4.10}$$

with G_Δ a filter. This solver use a sharp spherical truncation in which all Fourier modes having wavenumber greater than a specified cutoff k_{cutoff} are removed. The cutoff wavenumber is determined by the LES mesh size Δ. The filtered N-S equations Eq. (2.1) and Eq. (2.2) in physical space can be written as

$$\frac{\partial \overline{u}_i}{\partial x_i} = 0 \tag{4.11}$$

$$\frac{\partial \overline{u}_i}{\partial t} + \frac{\overline{u_i u_j}}{\partial x_j} = -\frac{1}{\rho}\frac{\partial \overline{P}}{\partial x_i} + \frac{\partial \overline{\tau}_{ij}}{\partial x_i} + \frac{1}{\rho}\overline{f_i} \tag{4.12}$$

with the stress tensor define as

$$\overline{\tau}_{ij} = 2\nu \overline{S}_{ij}$$

and the deformation tensor

$$\overline{S}_{ij} = \frac{1}{2}\left(\frac{\partial \overline{u}_i}{\partial x_j} + \frac{\partial \overline{u}_j}{\partial x_i}\right)$$

Here we suppose that the filter operation can be put in the differential operation. This is validated only when the filter cutoff wavenumber is based on the mesh size. Applying the scale decomposition Eq. (4.9) into the convection term on the left side of Eq. (4.12) is

$$\overline{u_i u_j} = \overline{(\overline{u_i} + u_i')(\overline{u_j} + u_j')}$$

The equation (4.11) becomes

$$\frac{\partial \overline{u}_i}{\partial t} + \frac{\partial(\overline{u_i}\ \overline{u_j})}{\partial x_j} = -\frac{1}{\rho}\frac{\partial \overline{P}}{\partial x_i} + \frac{\partial(\overline{\tau_{ij}} - \tau_{ij}^{SGS})}{\partial x_i} + \frac{1}{\rho}\overline{f_i} \tag{4.13}$$

where the tensor $\tau_{ij}^{SGS} = \overline{u_i u_j} - \overline{u_i}\ \overline{u_j}$ is the sub-grid contribution of the constraint and can be decomposed as:

$$\tau_{ij}^{SGS} = \underbrace{\overline{\overline{u_i}\ \overline{u_j}} - \overline{u_i}\ \overline{u_j}}_{I} + \underbrace{\overline{\overline{u_i} u_j'} + \overline{\overline{u_j} u_i'}}_{II} + \underbrace{\overline{u_i' u_j'}}_{III} \tag{4.14}$$

The term I is the interaction between two vortices of resolved scale and will transfer its energy to smaller scales the second term (II) is the interaction between the resolved motion and the unresolved motion (sub-grid motion). Due to this interaction, the kinetic energy could transfer to two directions but in average the energy transfer to smaller scales. The third term (III) is the interaction between the sub-grid motion and it contributes to the energy transfer from the small scales to large scales. In practice, in order to compute the filtered convection term $\overline{u_i}\ \overline{u_j}$, one need to double the mesh number which are needed to compute other terms [15]. Thus it is convenient to define the sub-grid stress tensor as $\tau_{ij}^{SGS} = \overline{u_i u_j} - \overline{\overline{u_i}\ \overline{u_j}}$. In Eq. (4.14) only II and III are left. The sub-grid constrain tensor can be decomposed to a contribution of isotropic and an anisotropic contribution

$$\tau_{ij}^{SGS} = \tau_{ij}^{sgs} + \frac{2}{3}\mathcal{K}\delta_{ij} \tag{4.15}$$

where τ_{ij}^{sgs} is the residual tensor of constrain an-isotropic and $\mathcal{K}$ is the residual kinetic energy of unit mass which can be expressed as

$$\mathcal{K} = \frac{1}{2}\tau_{ii}^{SGS} = \frac{1}{2}(\overline{u_i u_i} - \overline{\overline{u_i}\ \overline{u_i}}) \tag{4.16}$$

Note that the term $\frac{2}{3}\mathcal{K}\delta_{ij}$ is usually included in the pressure to form the modified pressure field $p = P + 2/3\mathcal{K}$ which is implicitly computed to ensure the divergence free of $\overline{u}_i$ Eq. (4.13) becomes

$$\frac{\partial \overline{u}_i}{\partial t} + \frac{\partial(\overline{\overline{u_i}\,\overline{u_j}})}{\partial x_j} = -\frac{\partial \overline{p}}{\partial x_i} + \nu \frac{\partial^2 \overline{u_i}}{\partial x_j \partial x_j} + \frac{1}{\rho}\overline{f_i} - \frac{\partial \tau_{ij}^{sgs}}{\partial x_i} \tag{4.17}$$

with $\overline{p} = \frac{\overline{P}}{\rho} + \frac{2}{3}\mathcal{K}$ is the modified pressure.

The usual approach is to approximate the sub-grid scale stresses with an eddy viscosity model. With this model, it is assumed that the off-diagonal terms of the stress tensor are proportional to the resolved rate of strain tensor $\overline{S}_{ij} = \frac{1}{2}(\frac{\partial \overline{u}_i}{\partial x_l} + \frac{\partial \overline{u}_l}{\partial x_i})$.

$$\tau_{ij}^{sgs} + \frac{2}{3}\mathcal{K}\delta_{ij} = 2\nu_t \overline{S}_{ij} \tag{4.18}$$

The trace of $\tau_{ij}^{sgs} + \frac{2}{3}\mathcal{K}\delta_{ij}$ is zero by construction as the trace of $\overline{S}_{ij}$ which is zero due to incompressibility condition. The proportionality coefficient is the eddy viscosity (or turbulent viscosity), ν_t, and fluctuate a priori in space and time.

The turbulent viscosity ν_t can be estimated base on Prandtl's mixing length hypothesis, giving the so-called Smagorinski model. The mixing length is given by the characteristic size of the largest unresolved scales of the flow motion which is the filter length Δ_f, and the characteristic velocity of the flow at this scale is locally estimated as $\Delta\sqrt{2\overline{S}_{ij}\overline{S}_{ji}}$, giving:

$$\nu_t = (C_s \Delta_f)^2 \sqrt{2\overline{S}_{ij}\overline{S}_{ji}} \tag{4.19}$$

with $C_s = 0.2$ a constant of the model [51].

Validation of the Eulerian solver: Firstly, the energy conservation test is by resolving the equation (4.4) and setting the viscosity and the external force to zero. We can see that the energy is fluctuating with an amplitude negligible, see in figure 4.1. And the energy spectral tend to have a equilibrium of energy throughout all the wave-numbers figure 4.2. This means that at each shell of the wavenumbers containing the same amount of energy

$$\int_{|k_i|<k<|k_i+1|} E(k)dk = Cst$$

The second test is designed to demonstrate that with the proposed energy

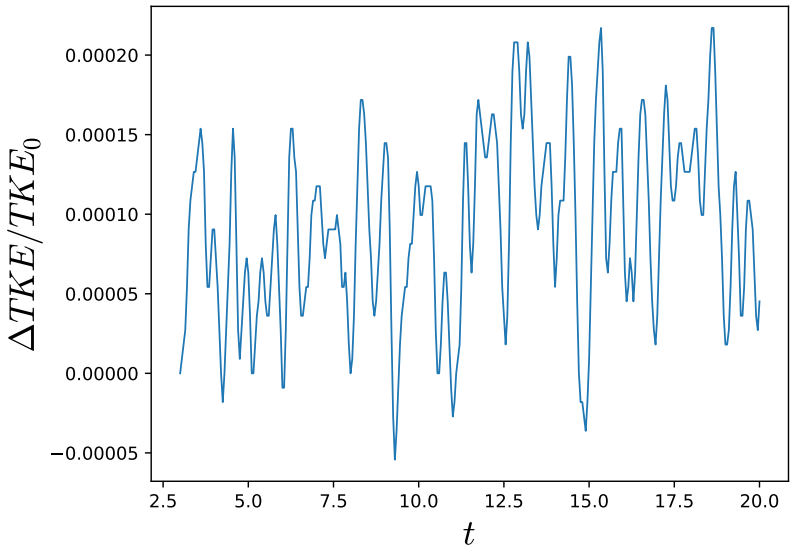

Figure 4.1: The evolution of turbulent kinetic energy fluctuations, by setting the viscosity and the forcing term to zero in N-S equations, versus time. with $\Delta TKE = TKE(t) - TKE(t_0)$ and $TKE_0 = TKE(t_0)$

injection the fluid field will tend to have a statistical stationary state. The fluid field is resolved with the forcing term Eq. (4.6) with $Re_\lambda \simeq 200$ and ratio of dissipative scale to the smallest resolved scale $\eta/\Delta \simeq 0.88$, with AB2 time advancing with the current number $CFL = 0.3$ and a deterministic forcing term Eq. (4.6). The flow field reaches a statistical stationary regime by $8 \sim 10$ times of the large eddy turn over time, where the fluctuations do not exceed $\pm 2.5\%$ of the estimated mean kinetic energy, see figure 4.1.

In order to test the model of LES, another direct simulation with a higher $Re_\lambda \simeq 200$ with a resolution of $N = 1024^3$ with $\eta/\Delta \simeq 0.725$ is computed. The velocity 3D spectral is shown in figure 4.4. In the same figure the spectral of LES with $Re_\lambda \simeq 200$ $N = 64^3$ with $\eta/\Delta \simeq 0.046$ is plotted. We can see that the spectral is cutoff at $k\eta \simeq 0.1$.

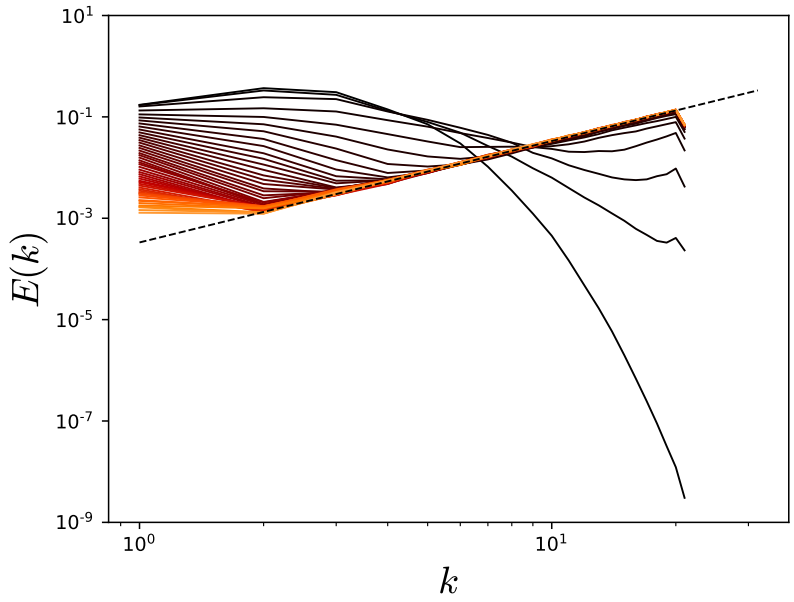

Figure 4.2: The evolution of energy spectral, by setting the viscosity and the forcing term to zero in N-S equation, with time. For the line with color black, is the initialized spectral. With time increases, the spectral tend asymptotically to power law the dash line (–) is $E(k) = k$. The color from back to orange is the time increasing sense.

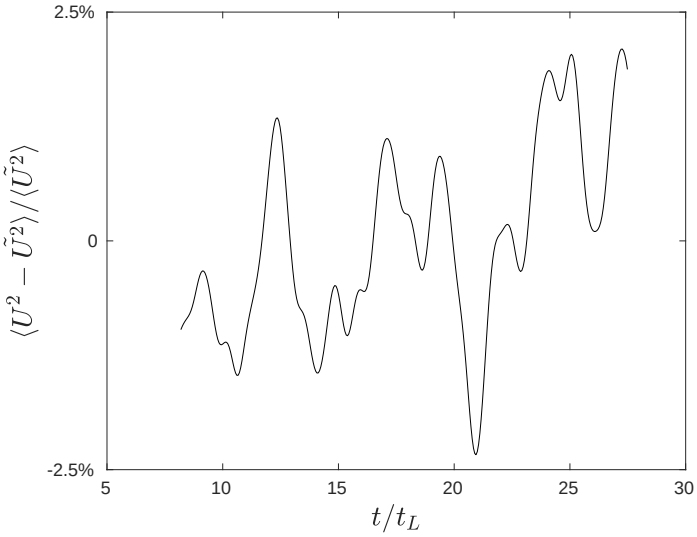

Figure 4.3: Kinetic energy statistics in all the computational domain with deterministic forcing keeping the volume-averaged energy at the large scales: t_L is the large eddy turn over time scale and U^2 is the kinetic energy at the instant t and $\tilde{U^2}$ is the estimated kinetic energy.

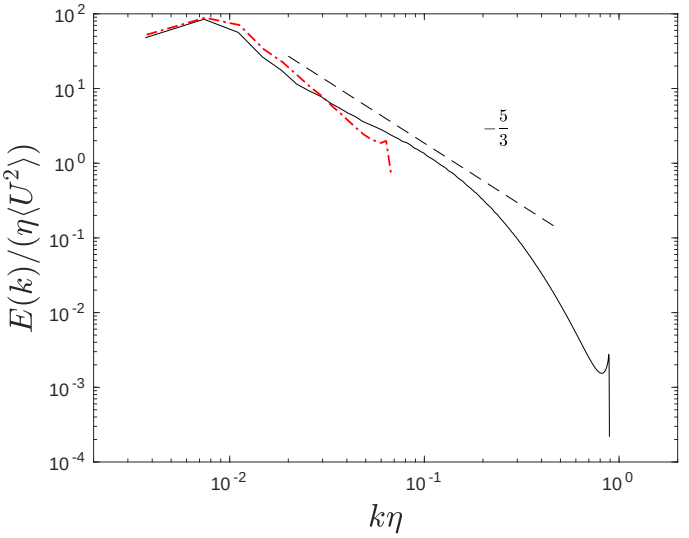

Figure 4.4: Velocity 3D spectral for $Re_\lambda \simeq 200$, (-) DNS ($-\cdot$), LES, (- -) is the power law of $-5/3$.

4.3 The Lagrangian solver

The solver gives the evolution of the bubbles with the point particle approach by solving the force balance equation (3.2). By knowing the Eulerian field and the position of the bubble at the beginning of the time step, the necessary information velocity, acceleration and vorticity can be interpolated at the positions of the bubbles. Then the ordinary differential equations (ODE) describing the motion of each of these bubbles are integrated in time accounting for the value of the carrier phase. The Lagrangian solver is paralleled with domain decomposition: each process takes care of the bubbles that are in his sub-domain. The following steps are done to obtain the dynamic of the bubbles:

- First, the value of the Eulerian fields is interpolated at the position of the bubble. This is generally required to compute the "right hand side" of the ODE. The interpolation is performed with a 4^{th}-order cubic spline. In figure 4.5, the material acceleration at the position of the fluid tracer $D_t \boldsymbol{u}_f$ and the acceleration of the fluid tracer $\frac{d\boldsymbol{u}_t}{dt}(t)$ is compared. We can see that the interpolating scheme provides a reasonable accuracy of the interpolation.

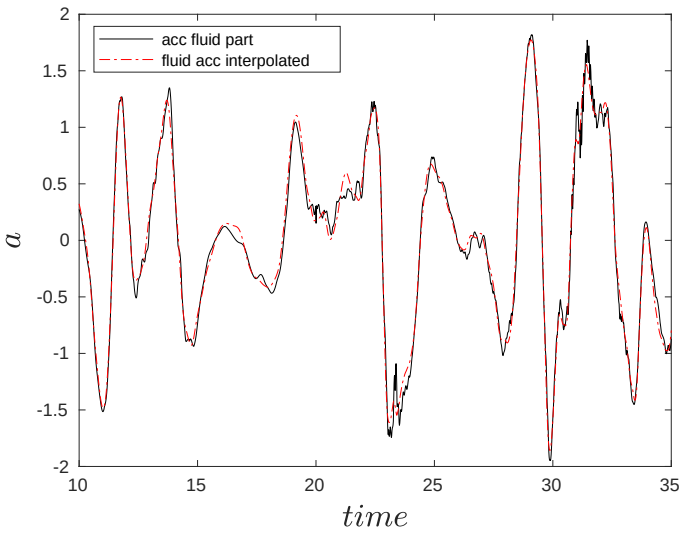

Figure 4.5: Compare of (- ·) fluid acceleration $D_t \boldsymbol{u}_f$ at the position of the tracer and (-) the tracer acceleration $\frac{d\boldsymbol{u}_t}{dt}(t)$.

- Second, integrate in time to obtain the new position, and velocity of the bubbles. Again the time advance scheme is AB2.

- Third, if a bubble has crossed the boundary of a sub-domain: this bubble is sent to the MPI task managing the sub-domain where the bubble is arrived.

Results of fluid tracer: The normalized fluid tracer velocity has a *pdf* close to the Gaussian distribution, figure 4.6. The fluid tracer acceleration

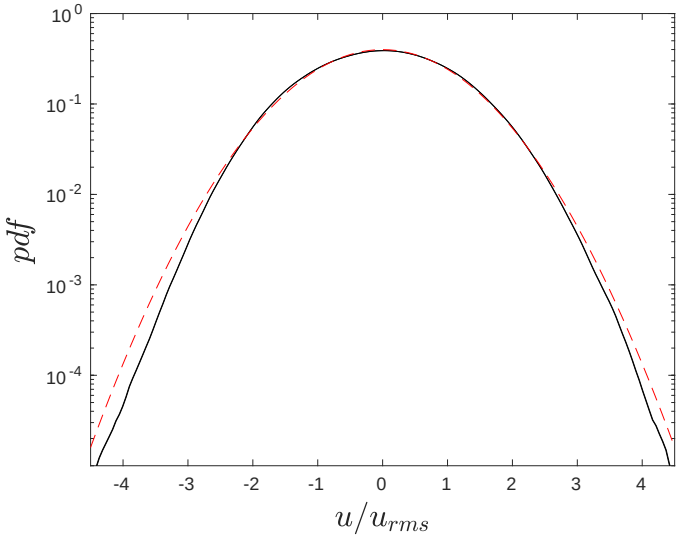

Figure 4.6: The probability density function of the fluid tracer velocity

probability distribution function is shown in figure 4.7. The acceleration *pdf* has been already known to have a no-Gaussian distribution with large stretched exponential tails corresponding to fluctuations much larger than the root-mean-value a_{rms} [20, 27]. This implies that the acceleration is as well a highly intermittent quantity in turbulence. The observation has also been reported in experimental study of fluid tracer acceleration [18] and numerical study [55]. The *pdf* of the fluid tracer x-component acceleration can be fitted with the relation (4.20). This relation is obtained by assuming that the amplitude of the acceleration has a log-normal distribution and the orientation of the acceleration vector being isotropic [18, 55]

$$pdf(a_i) = \frac{1}{2}\int_{|a_i|}^{\infty} \frac{pdf_{|a_i|}(a)}{a} da$$

The *pdf* function of the acceleration magnitude is

$$pdf_{|a_i|}(a) = \frac{1}{as\sqrt{2\pi}} \exp(-\frac{(\ln(a/\mu))^2}{2s^2})$$

with $\mu = \langle |a| \rangle$ and s is a parameter that depends on Re_λ. The acceleration *pdf* computed with LES lose the intermittency, the distribution form will tend to a Gaussian distribution if the cut off wavenumber continually decreases.

$$pdf_{a_i}(x) = \frac{\exp(1.5s^2)}{4\sqrt{3}} \left[1 - erf\left(\frac{\ln(|x/\sqrt{3}|) + 2s^2)}{s\sqrt{2}} \right) \right] \tag{4.20}$$

The acceleration variances resolved with LES are smaller than that of DNS

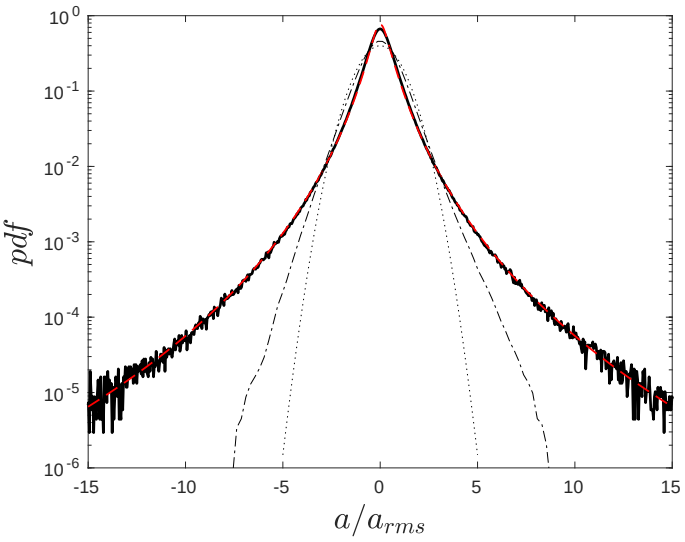

Figure 4.7: Acceleration *pdf*s of fluid tracer acceleration of $Re_\lambda \simeq 100$: (-)DNS (-·) LES $(\cdots)$ standard Gaussian distribution,(–) The relation (4.20) obtained by assuming the acceleration magnitude has a log-normal distribution.

is shown in figure 4.8. This difference can be explained by the Kolmogorov scale separation. The basic concept is to define the fluid acceleration as the smallest velocity increment resolved by the corresponding resolution dividing the corresponding time scale $a \sim \delta_\tau \boldsymbol{u}/\tau$. Consider a fluid tracer adverting in the turbulence with velocity $\boldsymbol{u}$ after a time lag τ, the fluid tracer appears at a different place with a distance of r to its position at the instant t. The velocity increment of time is equal to the velocity increment in the space $\delta_\tau \boldsymbol{u} = \delta_r \boldsymbol{u}$. According to the similarity of Kolmogorov, the velocity fluctuation at scale $\eta < r < L$ in the inertial range has the velocity increment $\delta_r \boldsymbol{u} \sim (r/L)^{1/3}$ and with corresponding time scale $\tau \sim (r/L)^{2/3}$. The acceleration of the resolved fluid field is $a \sim (r/L)^{-1/3}$. Then we have $a_f^2/a_\eta^2 \sim (r/\eta)^{-2/3}$. This result is proven with our simulation data, as shown in figure. 4.8.

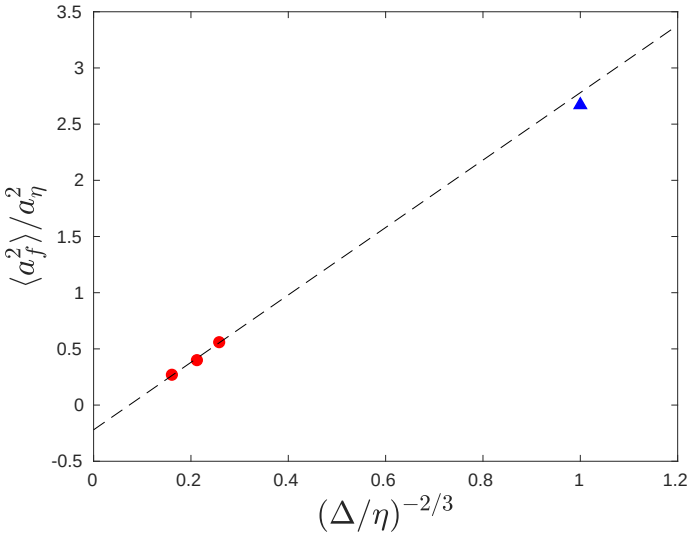

Figure 4.8: The acceleration variance of fluid particles from left to right with respectively the resolution of (LES)$N = 32^2$, $N = 48^2$, $N = 64^3$, and (DNS)$N = 512^3$for $Re_\lambda \simeq 100$ (- -) is a linear fitting with a bent of 5/2.

The Lagrangian auto-correlation is shown in figure 4.9. The acceleration fluctuation de-correlates much faster than the velocity fluctuation. The characteristic of correlation time scale is about the Kolmogorov time scale τ_η while the velocity correlation time is the energy containing time scale t_L.

4.4 Conclusions

In this chapter, the numerical code used to solve the homogeneous isotropic turbulence has been presented. The Eulerian solver is designed to use spectral discretizations to solve Navier-Stokes equations enforcing the divergence free constraint for the velocity fields in 3D box with periodic boundary conditions. The Lagrangian solver uses the point-wise particle method to track the bubble trajectory.

Besides, we also present the simulation results resolved with this code for a fluid tracer. Comparing the results of the fluid tracer with literature [18, 55], the code is proved to have a good performance. In the following studies, this code will be used.

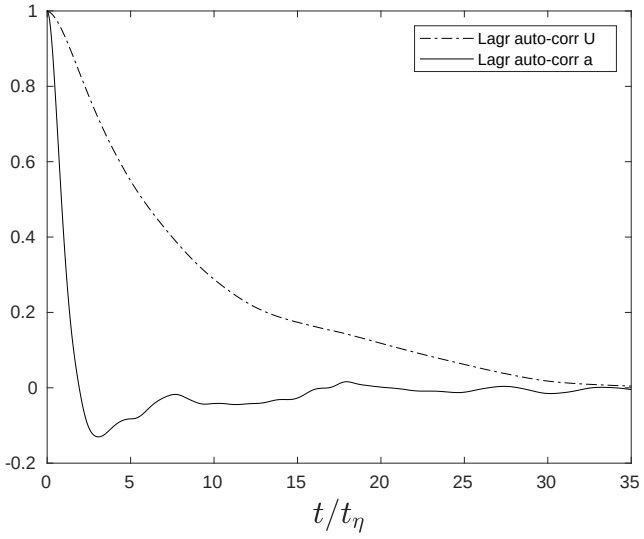

Figure 4.9: The Lagrangian auto-correlation of (- -) fluid particle velocity, and of (-) fluid particle acceleration

Chapter 5

Model for the dynamics of micro-bubbles in high-Reynolds-number flows

This chapter is presented in the form of a standalone article. We performed DNS for turbulence with $Re_\lambda \simeq 200$ and used the one-way coupling point-wise particle method considering the drag and the fluid inertia forces to study the bubble dynamics in turbulent flows. We propose a model for the acceleration of micro-bubbles (smaller than the dissipative scale of the flow) in a homogeneous and isotropic turbulent flow. Furthermore, we propose a sub-grid stochastic model, within the LES framework, as an extension of the approach of [24] in order to account for the unresolved fluid turbulent fluctuations in the dynamics of micro-bubbles for locally homogeneous and isotropic high-Reynolds number flows.

J. Fluid Mech. (2019), *vol.* 879, *pp.* 554–578.
doi:10.1017/jfm.2019.662

Model for the dynamics of micro-bubbles in high-Reynolds-number flows

Zhentong Zhang[1], Dominique Legendre[1] and Rémi Zamansky[1,†]

[1]Institut de Mécanique des Fluides de Toulouse (IMFT), Université de Toulouse, CNRS, INPT, UPS, Toulouse, France

(Received 20 December 2018; revised 8 August 2019; accepted 8 August 2019)

We propose a model for the acceleration of micro-bubbles (smaller than the dissipative scale of the flow) subjected to the drag and fluid inertia forces in a homogeneous and isotropic turbulent flow. This model, that depends on the Stokes number, Reynolds number and the density ratio, reproduces the evolution of the acceleration variance as well as the relative importance and alignment of the two forces as observed from direct numerical simulations (DNS). We also report that the bubble acceleration statistics conditioned on the local kinetic energy dissipation rate are invariant with the Stokes number and the dissipation rate. Based on this observation, we propose a stochastic model for the instantaneous bubble acceleration vector accounting for the small-scale intermittency of the turbulent flows. The norm of the bubble acceleration is obtained by modelling the dissipation rate along the bubble trajectory from a log-normal stochastic process, whereas its orientation is given by two coupled random walks on a unit sphere in order to model the evolution of the joint orientation of the drag and inertia forces acting on the bubble. Furthermore, the proposed stochastic model for the bubble acceleration is used in the context of large eddy simulations (LES) of turbulent flows laden with small bubbles. To account for the turbulent motion at scales smaller than the mesh resolution, we decompose the instantaneous bubble acceleration in its resolved and residual parts. The first part is given by the drag and fluid inertia forces computed from the resolved velocity field, and the second term refers to the random contribution of small unresolved turbulent scales and is estimated with the stochastic model proposed in the paper. Comparisons with DNS and standard LES, show that the proposed model improves significantly the statistics of the bubbly phase.

Key words: bubble dynamics, particle/fluid flow, isotropic turbulence

1. Introduction

In various industrial set-ups, such as chemical reactors, water treatment, steam generators and systems for drag reduction, the presence of a bubble phase plays an essential role. The further improvement of these applications rely on our ability to predict the dynamics of the bubbles in highly turbulent flows. However, even if the equation for the dynamics of micro-bubbles (i.e. bubbles smaller than the

† Email address for correspondence: remi.zamansky@imft.fr

dissipative scale of the flow) is well known and only depends on the local velocity of the fluid and its derivatives (Gatignol 1983; Maxey & Riley 1983; Magnaudet & Eames 2000), it remains challenging to precisely estimate the statistics of the bubble acceleration in turbulent flows. These difficulties arise because all the flow scales affect the bubble motion. In particular, the small scales of the flow play an essential role. Indeed, for small bubbles, the dominance of the fluid inertia term in the bubble dynamics equation leads to an increase of the bubble acceleration variance with the bubble diameter (Calzavarini *et al.* 2009; Prakash *et al.* 2012; Mathai *et al.* 2016) in contrast with inertial particles for which the fluid inertia terms can be neglected. Further, the non-Gaussian acceleration probability density functions (p.d.f.s) with broad probability tails of high bubble acceleration events observed experimentally and numerically (Mazzitelli & Lohse 2004; Volk *et al.* 2008*a*; Prakash *et al.* 2012) stress the importance of the intermittent fluctuations characteristic of the small scales of the flow. In addition, the specificity of bubble acceleration statistics has been shown to affect, among other important statistical quantities, their dispersion and clustering properties (Mazzitelli & Lohse 2004; Calzavarini *et al.* 2008; Tagawa *et al.* 2012, 2013).

For very large Reynolds-number flows, it remains impossible to resolve all the turbulent scales with direct numerical simulations (DNS). This is why, when the large scale features of the flow mainly depend on the specific configuration, the large eddy simulations (LES) approach is commonly used. In such approaches, the effective action of the small-scale motions on the large-scale evolution is parameterized. Models based on the turbulent viscosity have proved to reasonably achieve such parameterization of the energy transfer rate below the resolved scale (Meneveau & Katz 2000; Sagaut 2002). Following this procedure, one obtains the evolution of a coarse-grained filtered velocity field, $\overline{u}_f$. Within this framework, the standard approach to perform LES with Lagrangian tracking for the dispersion of micro-bubbles in a turbulent flow is to substitute the local fluid velocity by the filtered velocity field in the bubble dynamics equation (Climent & Magnaudet 1999; van den Hengel, Deen & Kuipers 2005; Hu & Celik 2008; Dhotre *et al.* 2013). However, doing so, the small (unresolved) scales of the flow are discarded from the bubble dynamics, resulting in strong underestimation of the bubble acceleration.

Different approaches were considered to account for the unresolved scales in the calculation of the drag force on small inertial particles. Most of them rely on the stochastic estimation of the subgrid fluid velocity along the Lagrangian trajectory of the particles (Fede & Simonin 2006; Berrouk *et al.* 2007; Pozorski & Apte 2009; Minier, Chibbaro & Pope 2014; Breuer & Hoppe 2017; Johnson & Meneveau 2017; Sawford 1991; Sawford & Guest 1991; Park *et al.* 2017). Nevertheless, none of these approaches addressed the issue of the fluid inertia force, which is essential for bubble dynamics. Aside, approaches have been proposed to reconstruct the fluid fluctuations in the Eulerian fields which can in turn be used to advect the dispersed phase (Kerstein 1999; Burton & Dahm 2005*a*,*b*; Ghate & Lele 2017). Among them Sabel'nikov, Chtab & Gorokhovski (2007) introduced the decomposition of the instantaneous fluid acceleration field into a filtered contribution and a random contribution to account for the intermittency at small, unresolved, scales (see also Sabel'nikov, Chtab-Desportes & Gorokhovski 2011; Zamansky, Vinkovic & Gorokhovski 2013; Sabelnikov, Barge & Gorokhovski 2019). Recently, Gorokhovski & Zamansky (2018) considered a similar decomposition for the instantaneous acceleration of dispersed objects,

$$\boldsymbol{a}_b = \underbrace{\overline{\boldsymbol{a}}_b}_{\substack{\textit{large-scale}\\ \textit{contribution}}} + \underbrace{\boldsymbol{a}_b^*}_{\substack{\textit{small-scale random}\\ \textit{contribution}}} . \tag{1.1}$$

The temporally and spatially filtered force is obtained from the resolved velocity field, $\overline{u}_f$, while the random force accounts for fluctuations at unresolved scales. The filtered contribution presents much less intense fluctuations than the total acceleration as can be verified in Lalescu & Wilczek (2018). In line with the Kolmogorov hypothesis, it is assumed that the main source of randomness in the acceleration is attributed to the fluctuation of the local energy transfer rate. We then propose to approximate the instantaneous small scale contribution of the acceleration by the acceleration conditionally averaged on the local value of the dissipation rate as 'seen' along the Lagrangian path $\varepsilon_* : \boldsymbol{a}_b^* \approx \langle \boldsymbol{a}_b \mid \varepsilon_* \rangle$. Within the LES framework, ε_* has to be modelled since its wide fluctuations cannot be resolved from the filtered velocity field. For solid inertial particles solely subject to the Stokes drag force, Gorokhovski & Zamansky (2018) proposed such a model along with a log-normal stochastic process as a surrogate to the local dissipation rate. In the present paper, we extend this approach to the dynamics of micro-bubbles dispersed in turbulent flows. We first use DNS to analyse the statistics of the bubble acceleration and of the two main forces acting on the bubble (drag and fluid inertia forces). Specifically, we investigate the evolution of the magnitude of the two forces with the bubble diameter and their relative orientation, as well as the statistics of the bubble acceleration conditioned on the local dissipation rate. To estimate the magnitude of the acceleration, we propose a model based on the bubble spectral response to the fluid velocity fluctuation initially proposed by Tchen (1947). Further, consistently with the time scale separation between the evolution of the norm and the orientation (Pope 1990; Mordant, Crawford & Bodenschatz 2004), our modelling is supplemented with a stochastic process for the orientation, $\boldsymbol{a}_b^* = |a^*|\boldsymbol{e}^*$. The proposed model accounts for intermittency effects, as well as the correlation and alignment between the drag force and the fluid inertia force.

The outline of the paper is as follows: in § 2 we provide the numerical details of the DNS and the LES of statistically stationary homogeneous and isotropic turbulent flows. In § 3, we report the statistics of the acceleration and of the forces obtained from the DNS for various Stokes numbers. We also present a model describing the dependence of these statistics. Section 4 gives the formulation of the stochastic models accounting for the unresolved fluid acceleration. Subsequently the coupling of this model with LES is assessed by comparison with DNS and standard LES.

2. Details of the numerical simulations

We consider very small bubbles dispersed in an isotropic homogeneous turbulent flow. The continuous liquid phase is given by the incompressible Navier–Stokes equation and the dispersed phase is treated with a point particle approach. The feedback of the bubbles on the carrier phase is disregarded. The carrier flow field is computed with a pseudo-spectral method in a periodic box (Zamansky *et al.* 2016; Gorokhovski & Zamansky 2018; Bos & Zamansky 2019). In order to maintain a statistically stationary state, a forcing term active at the smallest wavenumbers is applied to the Navier–Stokes equation (Chen *et al.* 1993). The flow field is simulated by DNS and LES for the same Reynolds number, and the details of the simulation parameters are given in table 1. For the LES, the turbulent viscosity is estimated by the standard Smagorinsky model, $\nu_\Delta = C_s \Delta |\overline{S_{ij}}|$, where $\overline{S_{ij}}$ is the filtered rate of strain tensor, Δ is the cutoff scale and C_s is the model parameter. With the Smagorinsky model, the energy transfer rate from scale Δ, $\varepsilon_\Delta = 2(\nu + \nu_\Delta)\overline{S}_{ij}\overline{S}_{ij}$ can give a relatively good estimate of the average energy flux, $\langle \varepsilon_\Delta \rangle = \langle \varepsilon \rangle$, with ε being the local rate of kinetic energy dissipation. However, the energy transfer rate from scale Δ typically

Method	N	Re_H	Re_λ	τ_L/τ_η	$\frac{\langle\varepsilon\rangle H}{K^{3/2}}$	L/η	η/Δ	ν_Δ/ν	τ_Δ/τ_η
DNS	1024^3	10 600	216	55.8	1.9	418	0.8	—	—
LES	64^3	10 100	193	51.3	2.09	367	0.045	9.7	52
LES	48^3	9 800	187	48.4	2.3	336	0.034	14.6	59
LES	32^3	9 381	175	45.5	2.47	307	0.02	25	80

TABLE 1. The numerical parameters of the DNS and LES. The number of grid points in each direction is given by N. The size of numerical domain is $H = 2\pi$, $\tau_L = (2/3K)/\varepsilon$ is the eddy turnover time, $L = (2/3K)^{3/2}/\varepsilon$ is the scale of the large eddies, K is the average turbulent kinetic energy and ε is the average dissipation rate. The Reynolds number based on the large scale of the flow is given by Re_H, Re_λ is Reynolds number based on the Taylor length scale, η and τ_η are the Kolmogorov length and time scale and $\tau_\Delta = \Delta^2/\nu_\Delta$.

presents much less intense fluctuations compared to ε when $\Delta \gg \eta$. In the following, it is shown that ε is able to characterize the bubble dynamics, and we use a stochastic process to estimate the value of ε from ε_Δ.

For micro-bubbles in turbulence, the bubble equation of motion is essentially given by the drag force and the inertia force (Gatignol 1983; Maxey & Riley 1983; Magnaudet & Eames 2000),

$$\boldsymbol{a}_b(t) = \frac{\mathrm{d}\boldsymbol{u}_b(t)}{\mathrm{d}t} = -\frac{\boldsymbol{u}_b(t) - \boldsymbol{u}_f(\boldsymbol{x} = \boldsymbol{x}_b(t), t)}{\tau_b} + \beta \frac{\mathrm{D}\boldsymbol{u}_f}{\mathrm{D}t}(\boldsymbol{x} = \boldsymbol{x}_b(t), t); \qquad \frac{\mathrm{d}\boldsymbol{x}_b(t)}{\mathrm{d}t} = \boldsymbol{u}_b(t), \tag{2.1a,b}$$

where $\boldsymbol{a}_b$, $\boldsymbol{u}_b$ and $\boldsymbol{x}_b$ are the bubble acceleration, velocity and position, $\boldsymbol{u}_f$ is the fluid velocity field and $\mathrm{D}\boldsymbol{u}_f/\mathrm{D}t = \partial\boldsymbol{u}_f/\partial t + \boldsymbol{u}_f \cdot \boldsymbol{\nabla}\boldsymbol{u}_f$ is its material derivative. The parameter β, which compares the mass accelerated by the fluid to the mass accelerated by the bubble, is defined as $\beta = (1 + C_m)/(\Gamma + C_m)$, where Γ is the density ratio and C_m is the added mass coefficient ($C_m = 1/2$ for a sphere in an unbounded environment). For a bubble $\tau_b = d_b^2/(24\nu)$, with ν the kinematic viscosity and d_b the bubble diameter, and $\beta = 3$, assuming that the gas–liquid density ratio is vanishing, and that the bubbles are non-deformable spheres with free slip at the liquid interface. For a solid body with no slip at the interface one has $\tau_b = (\Gamma + C_m)d_b^2/(18\nu)$ and for large density ratio $\beta \approx 0$. In (2.1) the history and lift forces are discarded as they appear less important (Legendre & Magnaudet 1997, 1998; Magnaudet & Eames 2000; Mazzitelli, Lohse & Toschi 2003; Calzavarini *et al.* 2008). Also as shown by Mathai *et al.* (2016) the effect of gravity is negligible on the bubble dynamics as long as $St/Fr \ll 1$, with $St = \tau_b/\tau_\eta$ and $Fr = a_\eta/g$ being the Stokes and Froude numbers, respectively, $\tau_\eta = \sqrt{\nu/\langle\varepsilon\rangle}$ and $a_\eta = \sqrt{\langle\varepsilon\rangle/\tau_\eta}$ being the Kolmogorov time and acceleration scales, respectively. To evaluate the right-hand side of (2.1) the value of fluid velocity and total acceleration fields at the bubble positions are interpolated from the computational grid with the Hermite interpolation scheme. For each Stokes number we track 1 628 000 bubbles per Stokes number for the DNS and 62 800 for the LES. In table 2 we give the Stokes number for our seven sets of simulations. For a bubble with $\Gamma = 0$, the only possibility to vary the Stokes number is to change d_b/η through the relation $d_b/\eta = \sqrt{24St}$. As apparent, for the largest Stokes numbers considered here, the point particles approach appear unrealistic as $d_b/\eta > 1$. Note, however, that according to Calzavarini *et al.* (2009), the finite volume effects appear to be significant for $d_b/\eta > 10$. Moreover, as seen in table 2 for the largest Stokes numbers, the bubble Reynolds number, $Re_b =$

St	0.021	0.074	0.20	0.45	1.01	1.55	2.07
$d_b\eta$	0.70	1.33	2.19	3.29	4.93	6.10	7.04
Re_b	0.06	0.36	1.4	4.2	11.3	18.4	25.1

TABLE 2. The Stokes numbers and non-dimensional diameters of the bubbles used for the DNS and LES, and the bubble Reynolds numbers computed from the DNS.

$\sqrt{\langle(\boldsymbol{u}_f-\boldsymbol{u}_b)^2\rangle}d_b/\nu$, becomes significant, and the Stokes drag law is not strictly valid for those Stokes numbers. Nevertheless, the drag of a spherical clean bubble needs corrected by a function of Re ranging between 1 and 3 in the limit of infinite Reynolds number. Typically for the maximum value reported in table 2, the correction is 1.9. So we do not expect a qualitative change on the behaviour of the results presented below. Therefore, we choose to keep a simple drag law in order to simplify the analysis. Finally let us mention that from a dimensional point of view to have $St=1$ and $Fr=1$ for bubbles in water, with normal gravity ($g=9.81$ m s^{-2}), requires $d_b\approx 0.0002$ m and $\varepsilon\approx 0.2$ m^2 s^{-3}.

The DNS results are detailed in the next section. They will serve as the basis for the discussion of the stochastic modelling developed in § 4.

3. Statistics of the bubble acceleration and of the fluid forces on the bubbles

Response of small bubbles and particles to turbulence is known to depend on both Stokes number and β. This is illustrated in figure 1 which presents the normalized acceleration variance against the Stokes number for various value of β. In this figure we report the data obtained from our DNS for micro-bubbles ($\beta=3$), the DNS for Calzavarini *et al.* (2009) for light particles ($\beta=2.5$) and heavy particles ($\beta=0.14$) and the DNS of Bec *et al.* (2010) for heavy particles ($\beta=0$). For the heavy particles ($\beta<1$), it is observed that the acceleration variance decreases when the Stokes number increases. This is in contrast to the case of bubbles and light particles ($\beta>1$) in which the bubble normalized acceleration variance increases with St.

Based on the dynamics of the bubble given by (2.1) and following the approach of Tchen (1947) (see also Hinze 1975), one can derive a response function of the bubble velocity fluctuations to the fluid fluctuations, $H_u(\omega)$,

$$E_b(\omega)=H_u^2(\omega)E_f(\omega);\quad H_u^2(\omega)=\frac{1+\beta^2\omega^2\tau_b^2}{1+\omega^2\tau_b^2},\tag{3.1a,b}$$

with ω the pulsation, and where $E_b(\omega)=\hat{\boldsymbol{u}}_b(\omega)\hat{\boldsymbol{u}}_b(-\omega)$ and $E_f(\omega)=\hat{\boldsymbol{u}}_f(\omega)\hat{\boldsymbol{u}}_f(-\omega)$ are the Lagrangian spectra of the bubble and fluid velocity and circumflexes are used to denote the Fourier coefficients. To obtain this relation we assume that the trajectory of the bubble does not deviate significantly from the trajectory of a fluid element as we substitute the material derivative of the fluid velocity by its time derivative along the bubble trajectory. This assumption is questionable as soon as the Stokes number of the bubble is not vanishingly small, and will be discussed later. Anyway, it enables us to easily obtain the qualitative behaviour of the bubble dynamics since in that case, it is not explicitly dependent on the fluid velocity gradient. As shown in the inset of figure 1, the response function differs significantly for a bubble ($\beta=3$) and a heavy particle ($\beta=0$). While for $\beta=0$, the inertia of the particle filters the high frequency fluctuations of the fluid, for a bubble the high frequency fluctuations

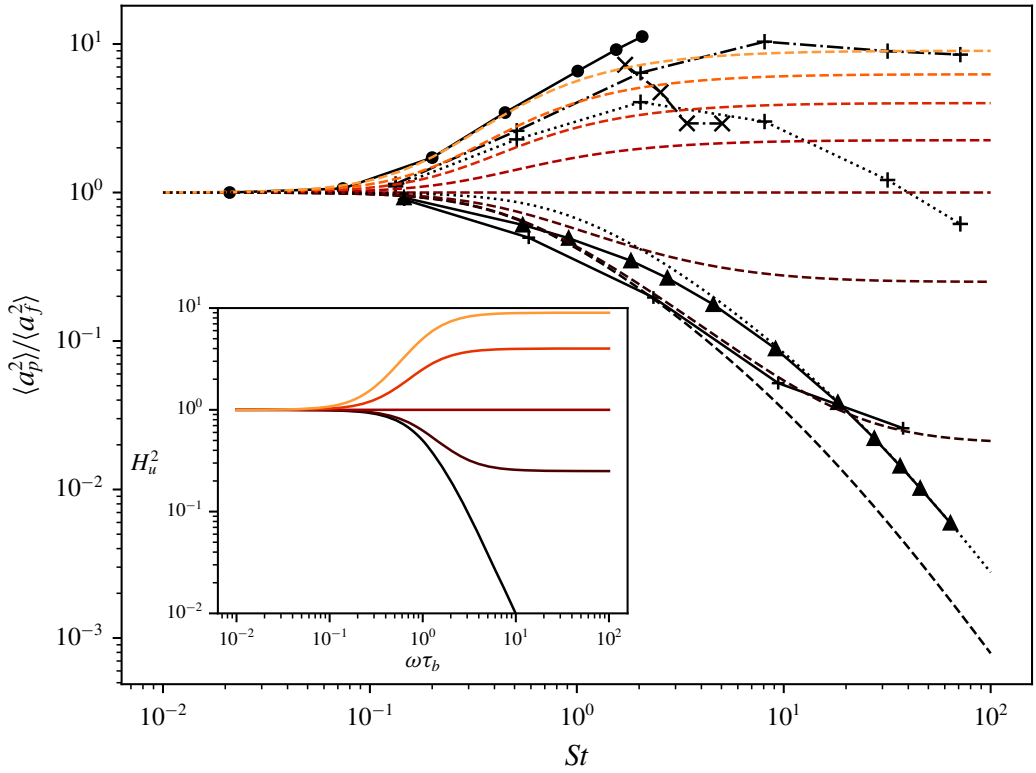

FIGURE 1. (Colour online) Acceleration variance normalized by the fluid tracer acceleration variance from our DNS for bubbles (● and continuous line), the DNS data of Bec *et al.* (2010) and Lanotte (2011) for heavy inertial particles $\beta = 0$, $Re_\lambda = 400$ (▲ and continuous line), the DNS from Calzavarini *et al.* (2009) for $\beta = 2.5$ and $Re_\lambda = 180$, with and without the Faxén correction (+ with dotted and dot-dashed lines, respectively), and $\beta = 0.14$ (+ with continuous line), the experimental measurements from Prakash (2013) for $Re_\lambda = 145 - 230$ and $\beta \approx 3$ (× with dashed lines). Comparison with the relation (3.4), $\langle \boldsymbol{a}_b^2\rangle(St, \beta, Re_0)/\langle \boldsymbol{a}_b^2\rangle(0, 1, Re_0)$ with $c_1 = 2.8$ and $Re_0^{1/2} = 0.08Re_\lambda = 16$ for $\beta = 0$, 0.14, 0.5, 1, 1.5, 2, 2.5 and 3 from black to orange, in dashed lines, and with $c_1 = 2.8$ and $Re_0^{1/2} = 0.08Re_\lambda = 32$, $\beta = 0$ in black dotted line. The inset is the response function (3.1) as a function of $\omega\tau_b$ for $\beta = 0$, 0.5, 1, 2 and 3 from black to orange, respectively.

of the fluid are amplified. From this relation one can also obtain the response function relating the bubble acceleration fluctuations to the fluid velocity fluctuations along the bubble trajectory, $H_a(\omega)$,

$$E_a(\omega) = H_a^2(\omega)E_f(\omega); \quad H_a^2 = \omega^2 H_u^2(\omega), \tag{3.2a,b}$$

with E_a the Lagrangian spectrum of the bubble acceleration. The bubble acceleration variance is given by $\langle \boldsymbol{a}_b^2\rangle = 2\int_0^\infty E_a(\omega)\,\mathrm{d}\omega$. To compute the variance, one needs to prescribe the Lagrangian fluid velocity spectrum along the bubble trajectory. For a fluid tracer the Lagrangian spectrum presents a power law for intermediate frequencies, $E_f(\omega) \sim \langle\varepsilon\rangle\omega^{-2}$ (Tennekes & Lumley 1972; Yeung 2001). To account for finite Reynolds number effects, and to have a finite energy density for $\omega \to 0$ we consider the form for the Lagrangian spectra (Hinze 1975; Mordant, Metz & Michel 2001) as follows:

$$E_f(\omega) \approx \frac{k_0\langle\varepsilon\rangle}{\omega^2 + \omega_0^2}, \tag{3.3}$$

with k_0 a constant, and ω_0^{-1} the Lagrangian integral time scale. Note that the relation (3.3) gives, for the velocity Lagrangian autocorrelation, $\rho(\tau) = \exp(-\omega_0\tau)$. As shown by Sawford & Yeung (2011), one has $(\tau_\eta\omega_0)^{-1} = (\omega_\eta/\omega_0)/2\pi \approx 0.08Re_\lambda$, with $\omega_\eta = 2\pi/\tau_\eta$. For convenience we note in the following $Re_0^{1/2} = (\tau_\eta\omega_0)^{-1}$. Furthermore the normalizing condition of the spectra, $\langle \boldsymbol{u}_f^2\rangle = 2\int_0^\infty E_f(\omega)\,\mathrm{d}\omega$, gives after integration $\langle \boldsymbol{u}_f^2\rangle = \pi k_0\langle\varepsilon\rangle/\omega_0$ that imposes $k_0 = 2(\tau_L/\tau_\eta)(\omega_0/\omega_\eta) \approx 4(\tau_L/\tau_\eta)Re_\lambda^{-1}$ with $\tau_L = \langle \boldsymbol{u}_f^2\rangle/\langle\varepsilon\rangle$ the large eddy time scale. This constant is computed from the DNS to be $k_0 \approx 1.04$ (see table 1). As seen from figure 2(*a*), with $k_0 = 1.03$ and $\omega_0/\omega_\eta = 0.0092$, the relation (3.3) provides a very good estimation of E_f for the various Stokes number considered here, for $\omega \ll \omega_\eta$. Nevertheless, the high frequency part of the spectra, which presents dependence on the Stokes number, is not predicted correctly by (3.3), an increase in inertia leads to more energy at high frequency. Let us note that for $\beta > 0$ the previous integral only converges if $E_f(\omega)$ decreases fast enough at large ω. Therefore to ensure its convergence, the integral is truncated above $k_1\omega_\eta$, independently of the Stokes number. This gives for the bubble acceleration variance the following relation:

$$\langle \boldsymbol{a}_b^2\rangle \approx c_0 a_\eta^2 \left[\beta^2 + \frac{1-\beta^2}{1-St_0^2}\frac{\tan^{-1}(c_1St)}{c_1St} - \frac{1-\beta^2St_0^2}{1-St_0^2}\frac{\tan^{-1}(c_1Re_0^{1/2})}{c_1Re_0^{1/2}}\right], \tag{3.4}$$

with $c_1 = 2\pi k_1$, $c_0 = 4\pi k_1 k_0$ and $St_0 = St/Re_0^{1/2}$ a Stokes number based on the large eddy time scale. Note that the previous relation does not present singularities for $St_0 = 1$ since in this case the last two terms cancel. Also $\langle \boldsymbol{a}_b^2\rangle$ remains positive for all St, Re_0 and β. Nevertheless, the assumptions used to derive (3.4) are *a priori* satisfied for $Re_0 \gg St^2$ and $Re_0 \gg 1$, and in this limit (3.4) becomes

$$\langle \boldsymbol{a}_b^2\rangle \approx c_0 a_\eta^2 \left[\beta^2 + (1-\beta^2)\frac{\tan^{-1}(c_1St)}{c_1St}\right]. \tag{3.5}$$

A similar relation is proposed by Zaichik & Alipchenkov (2011). Their derivation is based on the same approximation for the fluid acceleration and assumes the fluid velocity correlation in physical space that include a viscous cutoff at small scale contrary to the relation (3.3) used here. The relation (3.4) with $c_1 = 2.8$ and $Re_0^{1/2} = 16$ is plotted in figure 1 for various St and β. In this figure, the bubble acceleration variance is normalized by the acceleration variance of fluid tracers estimated from the model (3.4) by setting $St = 0$ and $\beta = 1$. It is seen that (3.4) is overall in good agreement with the DNS data sets for $\beta = 3$, 2.5, 0.14 and 0. The discrepancy between the DNS and relation (3.4) observed for the inertial particles around $St = 1$, is attributed to the preferential concentration of particles, since this effect is not accounted for in the model. For the inertial particles at $St \approx 0.5$ the model overestimates the acceleration by approximately 20 %. It is also observed that for $St > 1$, (3.4) underestimates the DNS when $\beta = 3$ and 2.5. Note also that the evolution of the acceleration variance with St and β given by the model (3.4) appears qualitatively similar to the DNS data presented by Volk *et al.* (2008*a*). As expected, the acceleration variance normalized by the acceleration variance of fluid tracer tends to unity when St goes to 0 for every value of β, indicating that bubbles with bubbles with extremely small diameter effectively behave as fluid tracers. According to (3.4) for $\beta = 0$, the decrease of the acceleration variance with the Stokes number presents the same scaling as the relation proposed by Gorokhovski & Zamansky (2018), namely $\langle \boldsymbol{a}_b^2\rangle/a_\eta^2 \approx 1$ for $St \ll 1$, $\langle \boldsymbol{a}_b^2\rangle/a_\eta^2 \sim St^{-1}$ for $1 \ll St \ll \sqrt{Re_0}$ and $\langle \boldsymbol{a}_b^2\rangle/a_\eta^2 \sim St^{-2}$ for $St \gg \sqrt{Re_0}$ and appears consistent with the relation proposed by Bec *et al.* (2006).

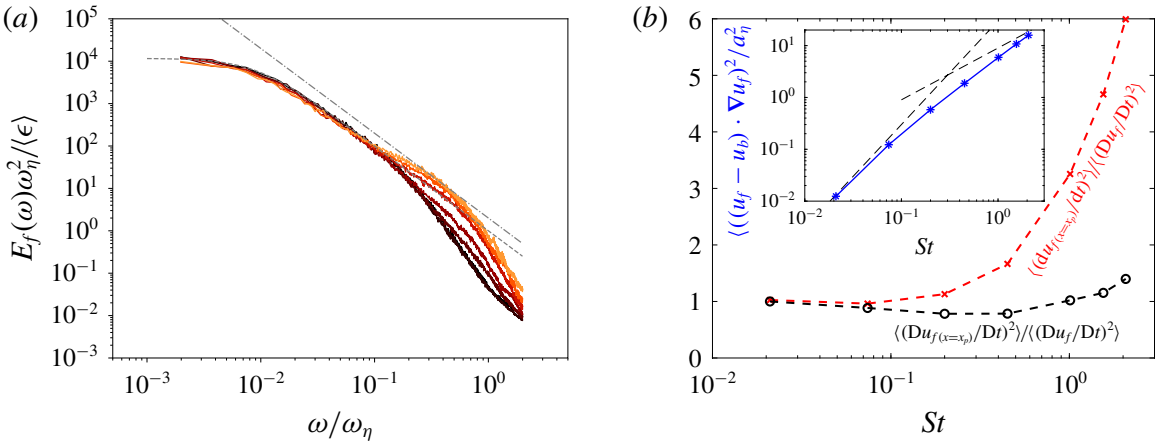

FIGURE 2. (Colour online) (*a*) Lagrangian fluid velocity spectra along the bubble trajectory from the DNS for $St = 0.02$, 0.074, 0.20, 0.45, 1.01, 1.55 and 2.07 (from black to red, respectively). Comparison with the power law ω^{-2} and the relation (3.3), $k_0/((\omega/\omega_\eta)^2 + (\omega_0/\omega_\eta)^2)$ with $k_0 = 1$ and $\omega_0/\omega_\eta = 0.0092$ in grey dot-dashed and dashed lines, respectively. (*b*) Evolution with the Stokes number of the variance of the material derivative of fluid velocity at the bubble position (black circles) and of the Lagrangian time derivative along the bubble trajectories of the fluid velocity (red crosses). Both quantities are normalized by the global variance of the fluid tracer acceleration. The inset is the variance of the difference between these two quantities in logarithmic scales normalized by the Kolmogorov acceleration and comparison with the St and $St^{1/2}$ power laws.

In contrast, for a bubble ($\beta = 3$), according to (3.4), the normalized acceleration variance increases as $\langle \boldsymbol{a}_b^2\rangle/a_\eta^2 - 1 \sim St^2$ and saturates to β^2 for $St \gg 1$. Note, however, that the limit $St \gg 1$ does not make sense, since for a bubble it implies $d_b^2/\eta^2 \gg 1$ which disagrees with the pointwise model. From the experimental results of Prakash *et al.* (2012) and the numerical simulations with a Faxén correction term (Calzavarini *et al.* 2009), also plotted in figure 1 for completeness, it appears that the finite size effect becomes important from $St \approx 2$ or $d_b/\eta \approx 7$, and leads to a decrease of the acceleration variance with a further increase of the bubble diameter (or Stokes number).

To analyse the substitution of the fluid velocity material derivative at the bubble position, $\mathrm{D}\boldsymbol{u}_f/\mathrm{D}t$, by its Lagrangian derivative along the bubble trajectory, $\mathrm{d}\boldsymbol{u}_f/\mathrm{d}t$, implied in (3.1), we remark that the material derivative can be written as $\mathrm{D}\boldsymbol{u}_f/\mathrm{D}t = \mathrm{d}\boldsymbol{u}_f/\mathrm{d}t + (\boldsymbol{u}_f - \boldsymbol{u}_p)\cdot\nabla\boldsymbol{u}_f$. We estimate that the order of magnitude of the last term is $O((\boldsymbol{u}_f - \boldsymbol{u}_p)\cdot\nabla\boldsymbol{u}_f) = \langle \boldsymbol{F}_d^2\rangle^{1/2} St$, $\boldsymbol{F}_d$ being the drag force. Therefore, based on the previously disused scaling of the inertial particle acceleration we expect that this term grows linearly with St for $St \ll 1$ and as $St^{1/2}$ for $1 \ll St \ll \sqrt{Re_0}$ (see also the relation for the variance of the drag force proposed latter in (3.6)). Note that to obtain the previous estimation we have assumed that velocity gradients are of order $1/\tau_\eta$ and thus we neglected intermittency effects which probably leads to an underestimation at large Reynolds numbers. As shown in the inset of figure 2(*b*) the proposed scaling for the difference appears to be consistent with the DNS. To analyse further the error due to the simplification of the fluid inertia term we have computed, from the DNS, the variances of $\mathrm{D}\boldsymbol{u}_f/\mathrm{D}t$ and $\mathrm{d}\boldsymbol{u}_f/\mathrm{d}t$. It is seen in figure 2(*b*) that for $St < 0.2$ the variance of the time derivative of the fluid velocity along the bubble trajectory remains sizable to the variance of the fluid acceleration at the

bubble position (around 10 % of difference) while, for $St = 1$, it is larger by a factor of roughly 3. Moreover, the normalized p.d.f. of these two quantities (not shown) remains quite similar even for the largest Stokes number considered here. We can then conclude that our approximation is reasonable for $St < 1$ and could lead to an overestimation of the fluid inertia term for larger St. Nevertheless, the range of validity of the substitution and of the pointwise bubble approximation are seen to coincide.

The expression (3.5) does not include any intermittency effects and Reynolds number dependence (Yeung *et al.* 2006). The intermittent behaviour of the dissipation rate which is accounted for by the stochastic models discussed in § 4 is associated with large fluctuations of the acceleration (Kolmogorov 1962; Castaing, Gagne & Hopfinger 1990; Lukassen & Wilczek 2017). This is seen in figure 3 presenting the bubble acceleration p.d.f. obtained from the DNS. It is observed that the bubble acceleration p.d.f. clearly presents a non-Gaussian behaviour with stretched tails indicating the occurrence of very intense acceleration events as pointed by Volk *et al.* (2008*a*), Prakash *et al.* (2012) and Loisy & Naso (2017). For intermediate Stokes number ($St \approx 0.5$) the bubble acceleration p.d.f. appears even more stretched than the p.d.f. of fluid tracer acceleration. While a further increase of St gives again a p.d.f. very similar to the p.d.f. of fluid tracer acceleration. Correspondingly, figure 3(*b*) shows that the bubble acceleration flatness ($Fl_a = \langle(\boldsymbol{a}_b - \langle \boldsymbol{a}_b\rangle)^4\rangle / \langle(\boldsymbol{a}_b - \langle \boldsymbol{a}_b\rangle)^2\rangle^2$) presents a maximum for a Stokes number around 0.2. Note that a peak was also observed in Calzavarini *et al.* (2009) but with a smaller maximum value and for a larger value of St. The difference is attributed to the smaller value of β and Re_λ ($\beta = 2.5$ and $Re_\lambda = 75$) used in Calzavarini *et al.* (2009). In this figure we also compare the flatness of fluid acceleration at the bubble position (or equivalently the flatness of the inertia force). It is observed that its value increases with St, but remains much smaller than the bubble acceleration flatness for intermediate Stokes numbers. As discussed below, the non-monotonic evolution of the bubble acceleration flatness is attributed to specific geometrical arrangements of the hydrodynamic forces applied to the bubble, rather than to a preferential concentration of bubbles in special regions of the flow (Calzavarini *et al.* 2008; Tagawa *et al.* 2012). Given the very large values taken by the flatness, this statistic might not be well converged, nevertheless there is no doubt that the flatness of the acceleration of the bubbles is much greater than that of the acceleration of the fluid at the bubble position.

From the relation (3.1) it is as well possible to obtain an estimate for the variance of the two terms on the right-hand side of (2.1), the drag force $\boldsymbol{F}_D = -(1/\tau_b)(\boldsymbol{u}_b(t) - \boldsymbol{u}_f(\boldsymbol{x} = \boldsymbol{x}_b(t), t))$, and the fluid inertia effect $\boldsymbol{F}_I = \beta(\mathrm{D}\boldsymbol{u}_f/\mathrm{D}t)(\boldsymbol{x} = \boldsymbol{x}_b(t), t)$,

$$\begin{aligned}\langle \boldsymbol{F}_D^2 \rangle &\approx \int_0^{k_1\omega_\eta} E_f(\omega) \frac{\omega^2(1-\beta)^2}{1+\omega^2\tau_b^2}\,\mathrm{d}\omega \\ &\approx c_0 a_\eta^2 \frac{(1-\beta)^2}{1-St_0^2}\left(\frac{\tan^{-1}(c_1 St)}{c_1 St} - \frac{\tan^{-1}(c_1 Re_0^{1/2})}{c_1 Re_0^{1/2}}\right) \end{aligned} \tag{3.6}$$

$$\begin{aligned}\langle \boldsymbol{F}_I^2 \rangle &\approx \int_0^{k_1\omega_\eta} E_f(\omega)\omega^2\beta^2\,\mathrm{d}\omega \\ &\approx c_0 a_\eta^2 \beta^2 \left(1 - \frac{\tan^{-1}(c_1 Re_0^{1/2})}{c_1 Re_0^{1/2}}\right). \end{aligned} \tag{3.7}$$

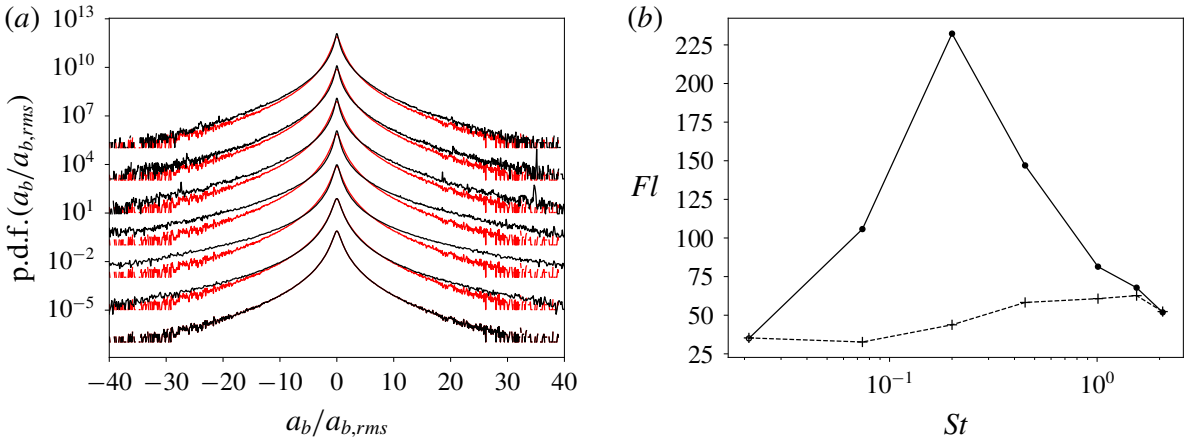

FIGURE 3. (Colour online) (*a*) The p.d.f.s of the bubble acceleration normalized by its root-mean-square value in black for $St = 0.02$, 0.074, 0.20, 0.45, 1.01, 1.55 and 2.07 (shifted upward by two decades from each other for clarity, respectively) and comparison with the p.d.f.s of the acceleration of fluid tracers in red. (*b*) Flatness of the bubble acceleration (●) and of the fluid acceleration at the bubble position (+) against St from our DNS.

These relations are plotted in figure 4(*a*) and are compared with the variance of the forces obtained from our DNS. Similar to the estimation of the acceleration variance expressions (3.6) and (3.7) are seen to provide a good estimation of the variances of $\boldsymbol{F}_D$ and $\boldsymbol{F}_I$ although the drag force is overestimated and the inertia force given by (3.7) is independent of the Stokes number which disagrees with the observation of figure 2(*b*). It is seen that for small Stokes numbers the variance of the two forces are commensurate, although the fluid inertia effect is dominant. Precisely, for $St \to 0$ the variance of the drag force is $(2/3)^2$ of that of the inertia term. It is also observed that the sum of the variance of the two forces is much larger than the variance of the bubble acceleration indicating a significant correlation between the two terms. As expected, when the Stokes number is increased, the drag force becomes negligible and the bubble acceleration is essentially given by the fluid inertia term.

Figure 4(*b*) presents the p.d.f. of both drag and fluid inertia forces for the various Stokes numbers. It is observed that for vanishingly small Stokes numbers ($St = 0.02$) the p.d.f.s of the two forces are essentially identical, and present both developed tails. The increase of the Stokes number results in a significant reduction of the tails of the drag force's p.d.f. whereas the p.d.f. of the inertia force presents very little variation (see also its flatness in figure 3). It is also worth mentioning that the p.d.f. of both forces remain symmetrical for all Stokes number indicating that the average and the skewness values of the two forces are zero. Because the bubbles sample regions of the flow in which the fluid acceleration variance is slightly below its overall value (see figure 2) and that the p.d.f. of the fluid acceleration at the bubble position is nearly invariant with the Stokes number, we conclude that the maximum of the bubble acceleration flatness is not caused by preferential concentration effects but is rather due to the alignment of the hydrodynamic forces on the bubble.

In figure 5(*a*), we plot the evolution of the correlation between $\boldsymbol{F}_D$ and $\boldsymbol{F}_I$ with the Stokes number obtained from the DNS. It is seen that for small St the two forces are completely anticorrelated, while they progressively decorrelate as St increases. Indeed requiring that for $St = 0$ the acceleration is equal to the acceleration of a fluid tracer, we obtain from (2.1) that $\boldsymbol{F}_D = (1 - \beta)/\beta \boldsymbol{F}_I$, that gives an anti-alignment for $\beta > 1$.

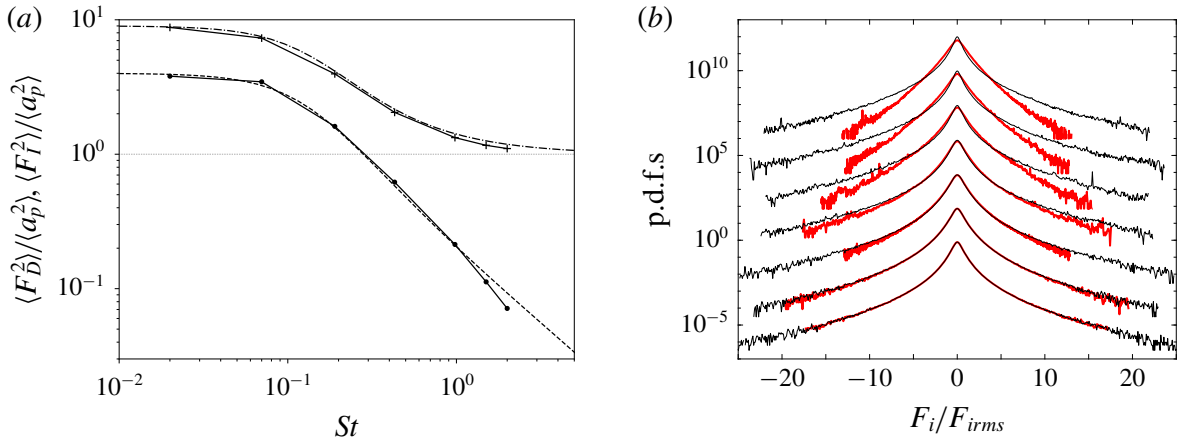

FIGURE 4. (Colour online) (*a*) Evolution with the Stokes number of the variance of the drag force (circle) and inertia force (crosses) relative to the bubble acceleration variance according to our DNS and comparison with (3.6) and (3.7) normalized by (3.4) with $c_1 = 2.8$ and $Re_0^{1/2} = 16$ in dashed and dot-dashed lines, respectively. (*b*) The p.d.f. of the fluid inertia forces (black) and of the drag force (red) normalized by their root-mean-square value for $St = 0.02$, 0.074, 0.20, 0.45, 1.01, 1.55 and 2.07 (shifted upward by one decade from each other for clarity, respectively).

Further, the correlation can also be readily estimated for larger Stokes numbers from (3.6), (3.7) and (3.4) as follows:

$$\langle \boldsymbol{F}_D \cdot \boldsymbol{F}_I \rangle \approx c_0 a_\eta^2 \frac{\beta(1-\beta)}{1-St_0^2} \left(\frac{\tan^{-1}(c_1 St)}{c_1 St} - \frac{\tan^{-1}(c_1 Re_0^{1/2})}{c_1 Re_0^{1/2}} \right). \tag{3.8}$$

Figure 5(*a*) shows that the relation (3.8) is in good agreement with the DNS results. Further, if the persistence of the temporal autocorrelation of the norms of the two forces is much longer than for their orientation, then the correlation between the two forces could be approximated by their relative orientation,

$$\langle \boldsymbol{F}_D \cdot \boldsymbol{F}_I \rangle \approx \langle \cos\theta \rangle (\langle \boldsymbol{F}_D^2 \rangle \langle \boldsymbol{F}_I^2 \rangle)^{1/2}, \tag{3.9}$$

where θ is defined as $\cos\theta = \boldsymbol{F}_D \cdot \boldsymbol{F}_I / |\boldsymbol{F}_D||\boldsymbol{F}_I| = \boldsymbol{e}_I \cdot \boldsymbol{e}_D$, with $\boldsymbol{e}_I$ and $\boldsymbol{e}_D$ the orientation vectors of the inertia term and of the drag force, respectively. This is confirmed in figure 5(*a*) that indeed $\langle \cos\theta \rangle$ remains quite close to $\langle \boldsymbol{F}_D \cdot \boldsymbol{F}_I \rangle (\langle \boldsymbol{F}_D^2 \rangle \langle \boldsymbol{F}_I^2 \rangle)^{-1/2}$. Figure 5(*b*) reports the evolution with the Stokes number of the p.d.f. of $\cos\theta$. For small Stokes numbers, the two forces appear to be essentially anti-aligned as the p.d.f. presents a sharp peak around -1 consistent with its averaged value. When the Stokes number is increased, the distribution of $\cos\theta$ becomes flatter, indicating that the relative orientation of the two forces becomes progressively statistically isotropic. Note that according to (3.8) we should expect a positive correlation between the two forces for $\beta < 1$ and small St.

In figure 6(*a*), we present the evolution of the Lagrangian autocorrelation of the bubble acceleration for the various Stokes numbers. It is observed that an increase of the Stokes number produces a faster decorrelation, as already reported by Volk *et al.* (2008*b*), although for $0 < St < 2$ it is seen that the correlation time remains of order τ_η. It is worth mentioning that this behaviour departs significantly from the evolution of inertial particles which present larger correlation time with increasing St (Gorokhovski

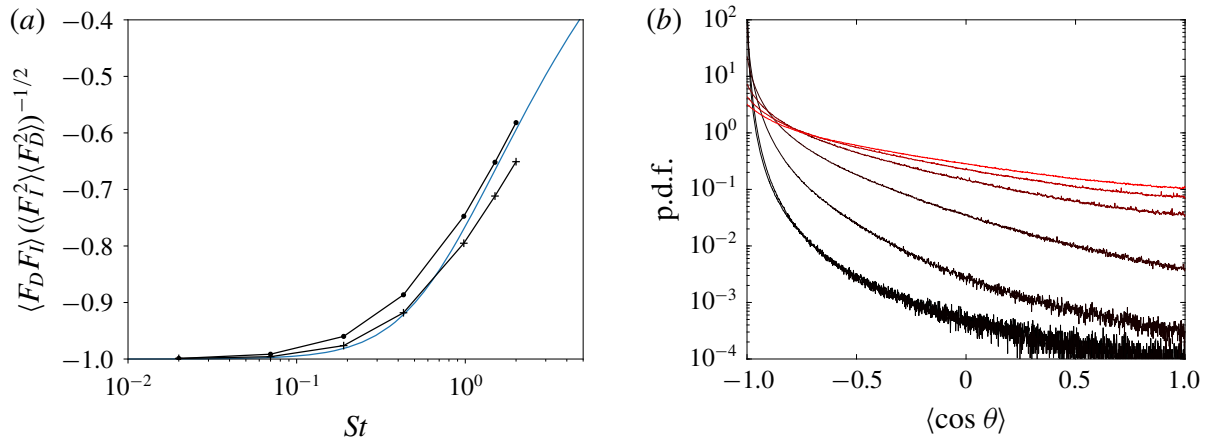

FIGURE 5. (Colour online) (*a*) Evolution with St of the coefficient of correlation between the drag and inertia forces (dots) and of $\langle \cos\theta \rangle$ (θ being the relative orientation of the forces) (crosses) from the DNS and comparison with relation (3.8) normalized by (3.6) and (3.7) with $c_1 = 2.8$ and $Re_0^{1/2} = 16$ in blue lines. (*b*) The p.d.f.s of the cosine of the angle θ between the two forces, for $St = 0.02$, 0.074, 0.20, 0.45, 1.01, 1.55 and 2.07 (from black to red, respectively).

& Zamansky 2018). To further analyse this point, we also present, in figure 6(*a*), the autocorrelation along the bubble trajectory of the two forces acting on the bubble. It is observed that for vanishingly small Stokes number, the two forces present exactly the same evolution of their Lagrangian correlation, because of the almost instantaneous response of the drag force to the inertia force. With increasing the Stokes number, one sees a clear difference in the autocorrelation of the drag force and of the inertia forces. Increasing the Stokes number gives a longer persistence time for the drag forces which can be directly attributed to the increase of τ_b. On the other hand, the faster decorrelation of the inertia force is explained by the deviation of the bubble trajectories from the fluid tracer trajectories.

The response of the drag force to the inertia term is analysed in figure 6(*b*) which presents the plot of the cross correlation of the orientation of the two forces along the bubble trajectory. The cross-correlation is defined as $\rho_{e_D,e_I} = \langle -\boldsymbol{e}_I(t) \cdot \boldsymbol{e}_D(t+\tau) \rangle / (\langle \boldsymbol{e}_I^2 \rangle \langle \boldsymbol{e}_D^2 \rangle)^{1/2}$. This figure confirms that the orientation of the drag forces responds to the inertia term. The temporal lag between the two forces can be estimated from the time shift of the peak, $\max_\tau(\rho_{e_D,e_I}(\tau)) = \rho_{e_D,e_I}(\tau_{lag})$. In the inset of figure 6(*a*), we present the evolution of τ_{lag} with St. It is seen that τ_{lag} presents a linear evolution for small τ_b. Indeed for vanishingly small Stokes number, the drag responds instantaneously. For larger Stokes number, the growth rate of τ_{lag} reduces. We observe that $\tau_{lag} \approx \tau_\eta(\beta - 1)^{-1} \tan^{-1}((\beta - 1)St)$ is a relatively good approximation of the lag of the drag force compared to the inertia effect. Clearly a further check of this speculative relation would require simulations for different values of β. We remark that one could estimate the autocorrelation of the bubble acceleration or hydrodynamic forces as well as the cross-correlation presented in figure 6 from the spectral response model of (3.1). However, this would require a more precise estimation of the Lagrangian fluid velocity spectra at high frequency than the relation (3.3), as the decorrelation is controlled by the dissipative range of the spectra which depend on St as seen in figure 2.

The anti-alignment of the forces at small Stokes can be explained as follows. For vanishingly small Stokes number, the relaxation time τ_b of the bubble velocity to the

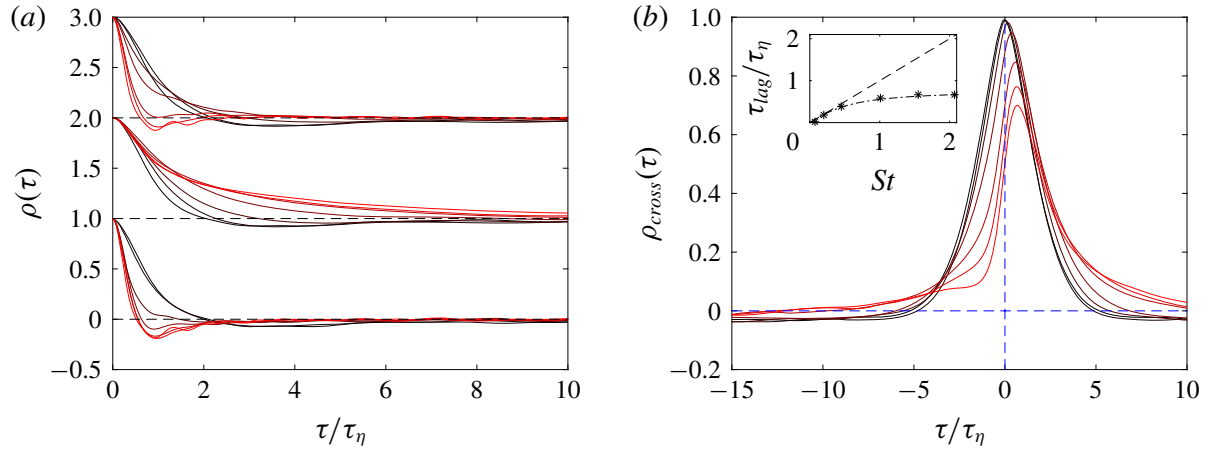

FIGURE 6. (Colour online) (*a*) Autocorrelation coefficient of the bubble acceleration, drag force and fluid inertia terms (shifted upward by one unit from each other, respectively, for clarity) from our DNS. (*b*) Cross-correlation between the drag force and the fluid inertia term as given by our DNS. The inset is the evolution of the time lag (defined as the time of the peak of cross-correlation) with St, and comparison with the $\tau_{lag}/\tau_\eta = St$ and $\tau_{lag}/\tau_\eta = (\beta-1)^{-1}\tan^{-1}((\beta-1)St)$. For both figures $St = 0.02$, 0.074, 0.20, 0.45, 1.01, 1.55 and 2.07 (from black to red, respectively).

local fluid velocity is much smaller than the persistence time of the fluid inertia term, which is of order τ_η (Pope 1990; Mordant *et al.* 2004). Therefore, the drag force will very quickly respond, leading it to be statistically opposed to the fluid inertia term. On the other hand, for $St \gg 1$ we should expect that the orientation of the two forces becomes independent because the relaxation time of the particle becomes much larger than τ_η. In the meantime, we have observed that the amplitude of the drag forces becomes negligible as the Stokes number is increased. This conjunction of the evolution of the relative orientation and magnitude of the two forces, leads to the increases of the bubble acceleration flatness, observed in figure 3 for St around 0.5. For these Stokes numbers, the amplitude of the drag forces remains significant while its orientation already presents a wide distribution, leading to the strong intermittency of the acceleration, when the two forces, of similar magnitude, are anti-aligned the acceleration will be close to zero whereas in case of an alignment of the forces intense acceleration will result.

We have proposed above a relation between the bubble acceleration variance and the average dissipation rate. However, in line with the Kolmogorov theory, the instantaneous acceleration depends *a priori* on the local energy dissipation rate ε. To discuss this point we present in figure 7 statistics of the bubble acceleration conditioned on the local value of the dissipation rate. This is also motivated to provide supports for a stochastic modelling of the bubble acceleration that accounts for the large fluid fluctuations in small-scale motions, as discuss in the following section. We consider in figure 7(*a*) the variance of the bubble acceleration conditioned on the local dissipation rate. We first observe that for ε larger than its average value, $\langle \boldsymbol{a}_b^2|\varepsilon\rangle$ appears to be independent of the Stokes number, and increases as $\varepsilon^{3/2}$, while it presents little dependence on both ε and St for small value of ε,

$$\langle \boldsymbol{a}_b^2|\varepsilon\rangle \approx \langle \boldsymbol{a}_b^2\rangle \left(\frac{\varepsilon}{\langle\varepsilon\rangle}\right)^{3/2}; \quad \varepsilon > \langle\varepsilon\rangle. \tag{3.10}$$

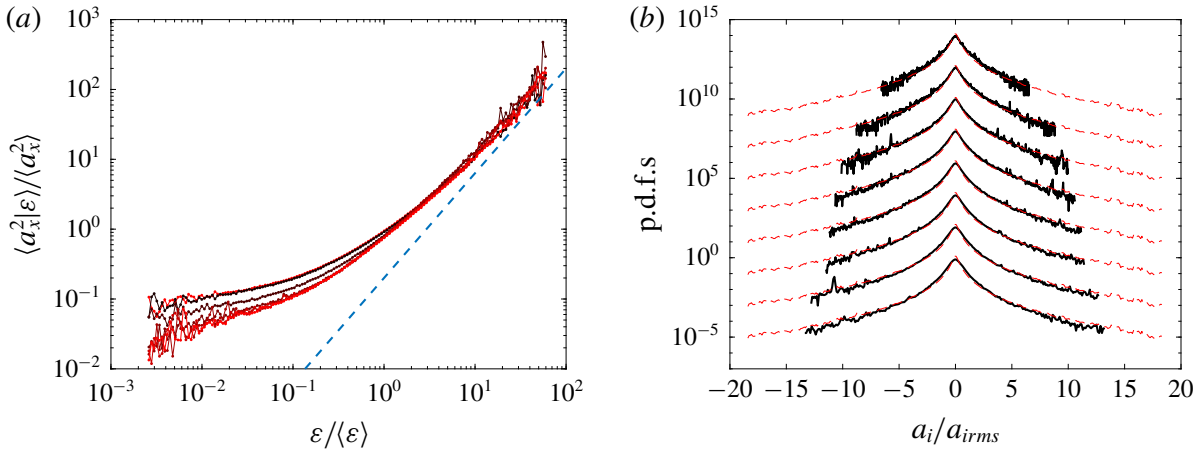

FIGURE 7. (Colour online) (*a*) Variance of the bubble acceleration conditioned on the local value of the dissipation rate ε for the various Stokes number $St = 0.02$, 0.074, 0.20, 0.45, 1.01, 1.55 and 2.07 (from black to red, respectively) normalized by unconditional bubble acceleration variance, and comparison with the relation $\langle \boldsymbol{a}_b^2|\varepsilon\rangle/\langle \boldsymbol{a}_b^2\rangle = (\varepsilon/\langle\varepsilon\rangle)^{3/2}$ with a dashed line. (*b*) The p.d.f.s of acceleration conditioned on the dissipation rate for $St = 1$. Eight values of ε are reported, $\varepsilon/\langle\varepsilon\rangle = 0.17$, 0.28, 0.46, 0.77, 1.3, 2.1, 3.5 and 5.8 (shifted upward by two decades from each other, respectively) and comparison with unconditioned bubble acceleration p.d.f. with dashed lines.

This behaviour is similar to previous observations for fluid tracers from Yeung *et al.* (2006). The invariance with *St* observed for the micro-bubbles is therefore attributed to dominance of the fluid inertia term. It was reported by Yeung *et al.* (2006) that the exponent of the power law for the conditional acceleration is reduced for low values of Reynolds numbers. Also Yeung *et al.* (2006) showed that the value at which the acceleration variance converge for $\varepsilon \to 0$ decreases with Reynolds number, indicating that the acceleration in the weakly dissipative regions is primarily influenced by the large-scale sweeping. In figure 7(*b*) the conditional p.d.f. normalized by its standard deviation is shown to be approximately self-similar with ε. The conditional p.d.f.s present slightly less developed tails than the unconditional p.d.f., similarly to the observation of Yeung *et al.* (2006) for fluid particles. Note that in figure 7(*b*), the conditional p.d.f.s are shown for $St = 1$ but a similar conclusion holds for the other Stokes number studied here.

4. Stochastic modelling of the dynamics of micro-bubbles

Following the proposition of Gorokhovski & Zamansky (2018) (see also Sabel'nikov *et al.* 2007, 2011; Zamansky *et al.* 2013), the instantaneous acceleration of each bubble is decomposed into filtered and stochastic parts. The first term corresponds to the contribution to the sweep imposed by the large (resolved) scales of the flow, and the second term accounts for the unresolved fluctuations of the carrier phase

$$\boldsymbol{a}_b = \overline{\boldsymbol{a}}_b + \boldsymbol{a}^*. \tag{4.1}$$

The residual contribution $\boldsymbol{a}^*$ is determined by the drag forces and the fluid inertia effect (added mass and Tchen force), $\boldsymbol{a}^* = \boldsymbol{F}_D^* + \boldsymbol{F}_I^*$, which are both considered as random processes. The stochastic forces are both decomposed into a norm and an orientation process, $\boldsymbol{F}_D^* = |\boldsymbol{F}_D^*|\boldsymbol{e}_D^*$ and $\boldsymbol{F}_I^* = |\boldsymbol{F}_I^*|\boldsymbol{e}_I^*$. These decompositions are supported

by the separation of time scale of the evolution of the autocorrelation for the norm and the orientation, suggesting that the norm and orientation of each force can be treated as independent processes, similarly to Pope (1990), Mordant *et al.* (2004) and Sabel'nikov *et al.* (2011). However, as mentioned previously, the two forces present significant correlation (both for their norm and their orientation) and could not be considered as independent.

First, in line with the refined Kolmogorov assumption, the main source of randomness in the instantaneous norms of the forces is attributed to the local energy dissipation rate. Then by analogy with relation (3.10), we propose the following:

$$|\boldsymbol{F}_D^*| \approx \langle \boldsymbol{F}_D^{*2}|\varepsilon_*\rangle^{1/2} \approx \langle \boldsymbol{F}_D^{*2}\rangle^{1/2} \left(\frac{\varepsilon_*}{\langle\varepsilon\rangle}\right)^{3/4}, \tag{4.2}$$

$$|\boldsymbol{F}_I^*| \approx \langle \boldsymbol{F}_I^{*2}|\varepsilon_*\rangle^{1/2} \approx \langle \boldsymbol{F}_I^{*2}\rangle^{1/2} \left(\frac{\varepsilon_*}{\langle\varepsilon\rangle}\right)^{3/4}. \tag{4.3}$$

In these relations, ε_* is obtained from a stochastic process mimicking the evolution of the dissipation rate along the bubble trajectory. Since it is observed that the norm of the two forces are strongly correlated, ε_* is the same stochastic variable in both relations (4.2) and (4.3). It was indeed observed from the DNS that the norms of the two forces remain strongly correlated for all the Stokes numbers considered here, consistent with (3.9). In order to only consider the contribution from the unresolved fluctuations in the estimation of $\langle \boldsymbol{F}_D^{*2}\rangle$ and $\langle \boldsymbol{F}_I^{*2}\rangle$, the integrals (3.6) and (3.7) are truncated for $\omega < k_2 2\pi/\tau_\Delta$ with $\tau_\Delta = \Delta^2/\nu_\Delta$ the time scale of the smallest eddies resolved by the mesh. And, as before, the integrals are also truncated for $\omega > k_1\omega_\eta$ to ensure its convergence. Considering, for simplicity, the high Reynolds limit $Re_0 \gg 1$ and $Re_0 \gg St^2$, the estimation for the instantaneous norms are then given by

$$|\boldsymbol{F}_D^*| = c_0^{1/2}\varepsilon_*^{3/4}\nu^{-1/4}|1-\beta| \left(\frac{\tan^{-1}(c_1 St)}{c_1 St} - \frac{\tan^{-1}(c_1 St Re_\Delta^{-1/2})}{c_1 St}\right)^{1/2}, \tag{4.4}$$

$$|\boldsymbol{F}_I^*| = c_0^{1/2}\varepsilon_*^{3/4}\nu^{-1/4}\beta(1-Re_\Delta^{-1/2})^{1/2}, \tag{4.5}$$

where $Re_\Delta^{1/2} = (k_2/k_1)\tau_\Delta/\tau_\eta$ is a Reynolds number characteristic of the subgrid scale motion. This gives for $\boldsymbol{a}^*$,

$$\boldsymbol{a}^* = c_0^{1/2}\varepsilon_*^{3/4}\nu^{-1/4}\left[\frac{|1-\beta|}{c_1 St}\left(\tan^{-1}(c_1 St) - \tan^{-1}\left(\frac{c_1 St}{Re_\Delta^{1/2}}\right)\right)^{1/2}\boldsymbol{e}_D^* + \beta(1-Re_\Delta^{-1/2})^{1/2}\boldsymbol{e}_I^*\right]. \tag{4.6}$$

Note that when the mesh is refined ($\Delta \to \eta$), $Re_\Delta \to 1$ and the amplitude of the residual contributions vanish as expected, since for a sufficiently fine mesh the bubble dynamics should be captured by the resolved contribution. Concerning the evolution of the stochastic variable ε_*, assuming that it is given by a log-normal process that depends on the local value of ε_Δ computed from the coarse LES mesh, one obtains the following stochastic process for $\varepsilon_*^{3/4}$ similar to Pope & Chen (1990) (see also Gorokhovski & Zamansky 2018):

$$\frac{\mathrm{d}\varepsilon_*^{3/4}}{\varepsilon_*^{3/4}} = \frac{\mathrm{d}\varepsilon_\Delta^{3/4}}{\varepsilon_\Delta^{3/4}} - \left(\ln\left(\frac{\varepsilon_*^{3/4}}{\varepsilon_\Delta^{3/4}}\right) - \frac{3}{16}\sigma^2\right)\frac{\mathrm{d}t}{\tau_\Delta} + \sqrt{\frac{9}{8}\frac{\sigma^2}{\tau_\Delta}}\,\mathrm{d}W, \tag{4.7}$$

where $\mathrm{d}W$ is the increment of the Wiener process and $d\varepsilon_\Delta^{3/4}$ is the increment of $\varepsilon_\Delta^{3/4}$ along the bubble trajectory. This stochastic process ensures that $\langle\varepsilon_*\rangle = \langle\varepsilon_\Delta\rangle$ (see the details in Gorokhovski & Zamansky (2018)), and the parameter σ is given by $\sigma^2 = 0.36 \ln Re_\Delta^{1/2}$ materializing the depth of the cascade process (Kolmogorov 1962; Castaing 1996), with the value of the coefficient in front of the logarithm set in order to reproduce the Reynolds number dependence reported by Yeung *et al.* (2006). The time scale τ_Δ imposes the temporal correlation of ε_*. Note that more sophisticated multiplicative models have been proposed for ε_* (Pereira, Moriconi & Chevillard 2018); however, in the present paper we have used the simple log-normal process (4.7).

The orientation vectors $\boldsymbol{e}_D^*$ and $\boldsymbol{e}_I^*$ appearing in (4.6) are given by two joint stochastic random walks on the unit sphere

$$d\boldsymbol{e}_I^* = \gamma_I \boldsymbol{e}_I^* \times \boldsymbol{\alpha}_I \,\mathrm{d}t + (\gamma_I - 1)\boldsymbol{e}_I^*, \tag{4.8}$$

$$d\boldsymbol{e}_D^* = \gamma_D \boldsymbol{e}_D^* \times \boldsymbol{\alpha}_D \,\mathrm{d}t + (\gamma_D - 1)\boldsymbol{e}_D^*, \tag{4.9}$$

with $\boldsymbol{\alpha}_I$ and $\boldsymbol{\alpha}_D$ the angular velocities of the evolution of $\boldsymbol{e}_I^*$ and $\boldsymbol{e}_D^*$ on the sphere and where the factors $\gamma_I = (1 + \boldsymbol{\alpha}_I.\boldsymbol{\alpha}_I \,\mathrm{d}t^2 - (\boldsymbol{\alpha}_I \cdot \boldsymbol{e}_I^*)^2 \,\mathrm{d}t^2)^{-1/2}$ and $\gamma_D = (1 + \boldsymbol{\alpha}_D.\boldsymbol{\alpha}_D \,\mathrm{d}t^2 - (\boldsymbol{\alpha}_D \cdot \boldsymbol{e}_D^*)^2 \,\mathrm{d}t^2)^{-1/2}$ correspond to a projection ensuring that the norms of both $\boldsymbol{e}_I^*$ and $\boldsymbol{e}_D^*$ remain unity (Gorokhovski & Zamansky 2018). The coupling of these two random walks, through the evolution of their angular velocities, is intended to reproduce the anti-alignment between the two orientation vectors observed for small Stokes number, and their decorrelation when St is increased as well as the correlation of the orientation with the coarse-grained (resolved) fluid acceleration. Moreover the temporal evolution of the random walks provides a temporal autocorrelation for the two orientations. The evolution of $\boldsymbol{\alpha}_I$ and $\boldsymbol{\alpha}_D$ is given by the following Ornstein–Uhlenbeck process presenting restoring terms, damping terms and diffusion terms:

$$\mathrm{d}\boldsymbol{\alpha}_I = -\boldsymbol{e}_I^* \times \frac{\mathrm{D}_t \overline{\boldsymbol{u}}_f}{\Delta} \,\mathrm{d}t - \boldsymbol{\alpha}_I \frac{\mathrm{d}t}{\tau_I} + \sqrt{\frac{\sigma_I^2}{\tau_I}} \,\mathrm{d}\boldsymbol{W}_I, \tag{4.10}$$

$$\mathrm{d}\boldsymbol{\alpha}_D = -\boldsymbol{e}_D^* \times \boldsymbol{e}_I^* \frac{\mathrm{d}t}{\tau_r^2} - \boldsymbol{\alpha}_D \frac{\mathrm{d}t}{\tau_D} + \sqrt{\frac{\sigma_D^2}{\tau_D}} \,\mathrm{d}\boldsymbol{W}_D, \tag{4.11}$$

with $\mathrm{d}\boldsymbol{W}_I$ and $\mathrm{d}\boldsymbol{W}_D$ the increments of two independent three-dimensional Wiener processes. The diffusion terms provide a return to isotropy of both orientations as the randomness of the angular velocities lead $\boldsymbol{e}_D^*$ and $\boldsymbol{e}_I^*$ to visit every point of the sphere. The temporal autocorrelation of both $\boldsymbol{e}_D^*$ and $\boldsymbol{e}_I^*$ is then related to the diffusion coefficient of the angular velocity. On the other hand, the restoring terms tend to align $\boldsymbol{e}_D^*$ and $\boldsymbol{e}_I^*$ with some equilibrium orientation.

For small values of τ_Δ/τ_η, we expect to have an alignment of the fluid acceleration model onto the coarse-grained fluid acceleration, while for τ_Δ/τ_η large, the alignment with the resolved acceleration should be weak, in agreement with the local isotropy assumption (Kolmogorov 1941). Therefore, in our model, we propose to have an alignment of the orientations of the subgrid contribution of the fluid acceleration to the coarse-grained fluid acceleration orientation $\overline{D_t \boldsymbol{u}}_f / |\overline{D_t \boldsymbol{u}}_f|$. The alignment between them is controlled by the restoring term in (4.10) and the time scale $(|\overline{D_t \boldsymbol{u}}_f|/\Delta)^{-1/2} \approx \tau_\Delta$.

The restoring term in (4.11) will tend to align $\boldsymbol{e}_D^*$ on $-\boldsymbol{e}_I^*$ in agreement with the observations of § 3. The rate of alignment is given by the parameters τ_r. Since the

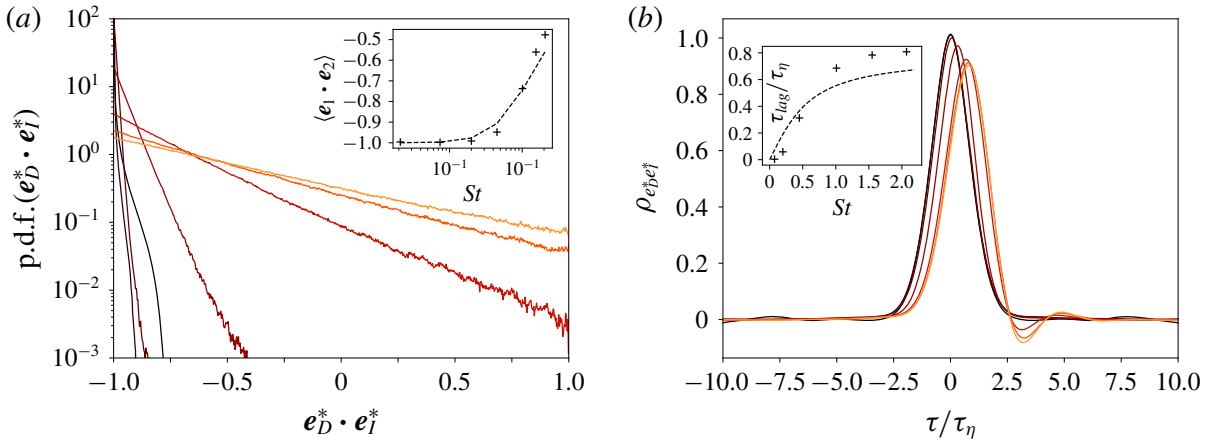

FIGURE 8. (Colour online) (*a*) The p.d.f.s of $\boldsymbol{e}_I^* \cdot \boldsymbol{e}_D^*$ for $St = 0.02$, 0.074, 0.20, 0.45, 1.01, 1.55 and 2.07 (from black to red, respectively) as obtained from model (4.8)–(4.11). The inset is the evolution of $\langle \boldsymbol{e}_D^* \cdot \boldsymbol{e}_I^* \rangle$ with St as given by the stochastic model, and comparison with the relation (3.8). (*b*) Cross-correlation between $\boldsymbol{e}_D^*$ and $\boldsymbol{e}_I^*$ obtained from the model (4.8)–(4.11). The inset is the evolution of the time lag between $\boldsymbol{e}_D^*$ and $\boldsymbol{e}_I^*$ against St, and comparison with $\tau_\eta(\beta-1)^{-1}\tan^{-1}((\beta-1)St)$.

latter should coincide with the time lag observed in the cross-correlation between the orientation of the two forces (see figure 6), we set $\tau_r = \tau_\eta(\beta-1)^{-1}\tan^{-1}((\beta-1)St)$. This ensures that the drag force correlation time increases with the Stokes number as observed in figure 6.

The other parameters in (4.10) are set to $\tau_I = \tau_\eta$ and $\sigma_I^2 = \tau_\eta^{-2}$ which ensure that the temporal autocorrelation of the fluid acceleration orientation is of the order of τ_η in agreement with the experimental findings of Mordant *et al.* (2004) and our DNS (see figure 6). In (4.11) the parameters are set to $\tau_D = (\tau_b + \tau_\eta)/4$ and $\sigma_D^2 = (\tau_b + \tau_\eta)^{-2}/2$ consistent with Gorokhovski & Zamansky (2018).

Figure 8(*a*) presents the evolution of the p.d.f. of the relative orientation between the two forces $\cos\theta^* = \boldsymbol{e}_D^* \cdot \boldsymbol{e}_I^*$, obtained from numerical integration of the stochastic orientation model (4.8)–(4.11) (and setting $D_t\overline{\boldsymbol{u}}_f = 0$ in (4.8)). We clearly observe that at small Stokes number the model predicts an anti-alignment between the two orientation vectors while their relative orientation becomes more isotropic when the Stokes number increases. This behaviour is in agreement with the statistics computed from the DNS (see figure 5*b*), although the p.d.f. from the DNS present a more stretched tail. It is also confirmed in the inset of figure 8(*a*) that the proposed stochastic model gives the correct evolution of the average relative orientation with the Stokes number, since as in the DNS case $\langle \cos\theta^* \rangle$ follow the relation (3.8). The cross-correlation between $\boldsymbol{e}_D^*$ and $\boldsymbol{e}_I^*$ is also presented in figure 8(*b*). The behaviour of the DNS observed in figure 6 can be qualitatively reproduced by the stochastic model with an increase of the time lag with the Stokes number.

The resolved contribution in (4.1) is obtained from a spatially and temporarily averaged version of (2.1). The spatial average arises from substituting the actual velocity field $\boldsymbol{u}_f$ to the coarse-grained velocity field $\overline{\boldsymbol{u}}_f$ in this equation. In addition, a temporal filter is also explicitly applied to prevent the term $\overline{\boldsymbol{a}}$ developing high frequencies that would correlate with the residual term. Removing the frequencies above $1/\tau_\Delta$ results in the following expression for $\overline{\boldsymbol{a}}$ (see also Gorokhovski & Zamansky 2018):

$$\overline{\boldsymbol{a}} = -\frac{\boldsymbol{u}_b - \overline{\boldsymbol{u}}_f}{\max(\tau_b, \tau_\Delta)} + \beta\frac{\mathrm{D}\overline{\boldsymbol{u}}_f}{\mathrm{D}t}, \tag{4.12}$$

where $D_t\overline{\boldsymbol{u}}_f = \partial_t\overline{\boldsymbol{u}}_f + \overline{\boldsymbol{u}}_f \cdot \boldsymbol{\nabla}\overline{\boldsymbol{u}}_f$ is the fluid total acceleration computed from the coarse mesh. Note that one does not have to necessarily consider the coupling with the LES to use the proposed model. Indeed, by considering the limit $\Delta \to L$, L being the integral length scale, the term $\overline{\boldsymbol{a}}$ vanishes and (4.1) becomes $\boldsymbol{a}_b = \boldsymbol{a}^*$. As well, in this limit one can replace $\varepsilon_\Delta(t)$ in (4.7) by the constant value $\langle\varepsilon\rangle$. For example, one can estimate the Reynolds number dependence for the intermittency correction in (3.5) from the moments of a log-normal variable, to be $\langle \boldsymbol{a}_b^2\rangle/a_\eta^2 \propto \exp(3/8\,\sigma^2) = Re_\lambda^{0.135}$, as proposed by Yeung *et al.* (2006).

In order to assess the approach (4.1) as well as the stochastic model proposed in (4.6)–(4.11), we present a comparison of the statistics of the bubble dynamics obtained from the DNS, the standard LES (without modelling of the residual bubble acceleration i.e. setting $\boldsymbol{a}^* = 0$ in (4.1)), and the LES with the proposed model. All the comparisons are made for $Re_\lambda \approx 200$ and three resolutions are used for the LES (32^3, 48^3 and 64^3) while the resolution of the DNS is 1024^3. The details of the LES are given in § 2.

We first present in figure 9(*a*) the evolution of the bubble acceleration variance with the Stokes number. We observe that the standard LES largely underestimates the bubble acceleration variance compared to the DNS. As expected the discrepancy increases as the mesh resolution is made coarser. This points out that the residual term in (4.1) is dominant. In contrast, the LES supplemented by the stochastic modelling is in very good agreement with the DNS. Moreover, with the stochastic model, the LES presents a very small dependence on the grid resolution. This confirms that the effects of the unresolved small scales of the flow are correctly accounted for by the model.

Figure 9(*b*) presents the p.d.f. of the bubble acceleration for the various Stokes numbers. It is seen that the standard LES predicts p.d.f.s that depart significantly from the DNS and remain much closer to the Gaussian distribution. On the other hand, the p.d.f.s from the LES with the stochastic model overlap very well with the p.d.f.s of the DNS over the whole range of Stokes numbers considered here. This shows that the intermittent behaviour of the bubble acceleration can be reproduced with the proposed stochastic model.

We consider in figure 10 the autocorrelation of the acceleration component. As illustrated for $St = 1$, the decorrelation of the acceleration is much slower from the LES than from the DNS. This is expected since the decorrelation of the acceleration component is attributed to the small-scale motions of the flow which are discarded in the LES. For the LES supplemented with the model the evolution of the correlation coefficient presents qualitative agreement with the DNS. This behaviour is confirmed in the inset of figure 10 which presents the correlation time, defined as the zero crossing time, against the Stokes number. It is observed that the correlation times obtained from the DNS and from the LES with the model both remain of the order of τ_η, whereas the standard LES predicts a much larger correlation time. We observe that the orientation model plays an essential role in obtaining an accurate estimation of the decorrelation time, and it is likely that an improvement of the model given by (4.8)–(4.11) could reduce the small discrepancies seen between the LES using the model and the DNS.

To evaluate the capability of the stochastic approach to accurately reproduce the time structure of the bubble velocity, we report in figure 11 the statistic of the velocity increments along the bubble trajectory. For that, we consider the structure function for a component of the bubble velocity $S_q(\tau) = \langle (u_{b,x}(t+\tau) - u_{b,x}(t))^q\rangle$. In figure 11(*a*) we present the evolution of the variance of the velocity increments, S_2,

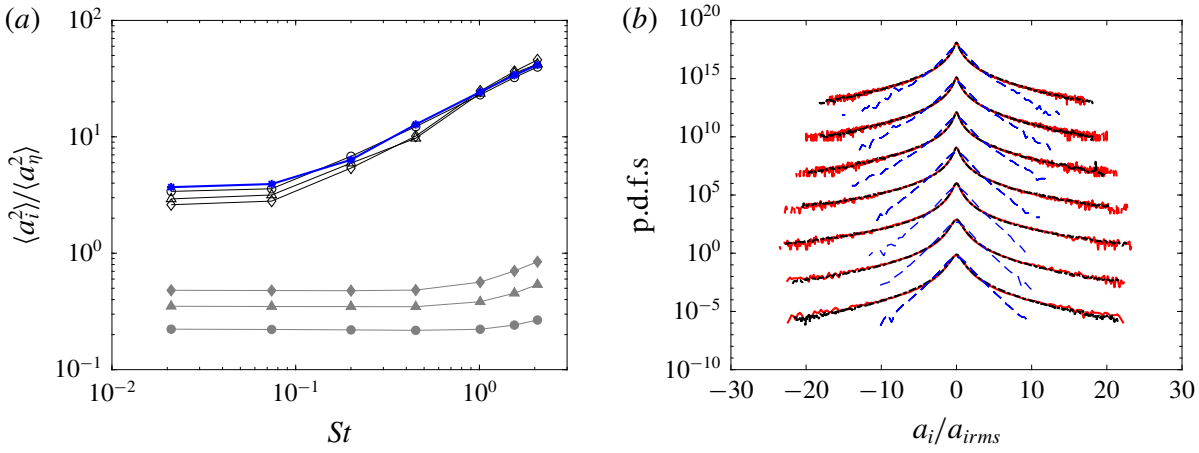

FIGURE 9. (Colour online) (*a*) Bubble acceleration variance normalized by the Kolmogorov acceleration (a_η^2) versus Stokes number in logarithm scale. Open symbols are LES with the proposed model; filled symbols are LES without model; for the three meshes we have 32^3 (circles), 48^3 (triangles) and 64^3 (diamonds). Comparison with our DNS blue stars. (*b*) The p.d.f. of the bubble acceleration normalized by its variance for $St = 0.02$, 0.074, 0.20, 0.45, 1.01, 1.55 and 2.07 (shifted upward by one decade each other, respectively). The DNS is a dashed black line, LES with the proposed model for 64^3 is a solid red line and LES without model for 64^3 is a blue dashed line.

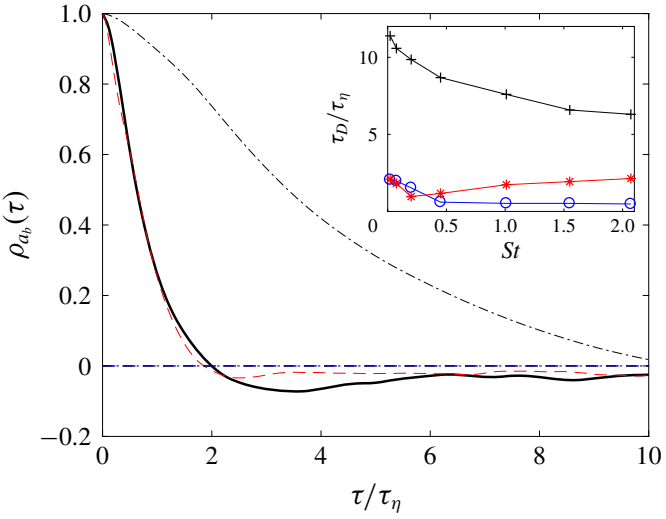

FIGURE 10. (Colour online) Autocorrelation of the bubble acceleration for $St = 0.07$. The DNS is a solid black line, LES with model for 64^3 is a dashed red line and LES without model for 64^3 is a dot-dashed black line. The inset is the evolution of the corresponding integral time scale normalized by the Kolmogorov time with the Stokes number. The DNS are circles, LES with the proposed model are stars, LES without model are crosses. The mesh size for the LES is 64^3.

with the time shift. The results from the LES with the proposed model follow very well those obtained from the DNS, whereas with the standard LES, the variance of the velocity increments is largely underestimated. Moreover, we observe that with the stochastic model the LES can reproduce the inertial range as observed from the DNS contrary to the standard LES. Figure 11(*b*) shows the evolution of the flatness of the bubble velocity increments, S_4/S_2^2. We see that with the standard LES the flatness

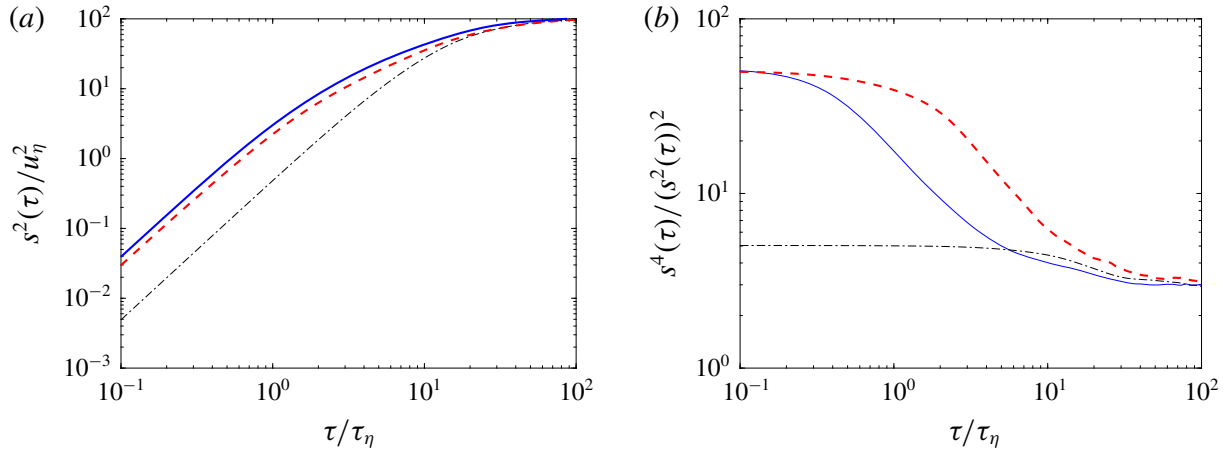

FIGURE 11. (Colour online) (*a*) Evolution of the second-order Lagrangian structure function with the time lag. (*b*) Evolution of the flatness of the Lagrangian velocity increments with the time lag. Comparison between the DNS (solid blue line), the Standard LES (black dot-dashed lines) and LES with the proposed model (dashed red lines). For both figures, for $St = 0.02$, the mesh size for the LES is 64^3.

remains close to its Gaussian value at all time shifts. In contrast, the LES with the proposed model gives an evolution of the flatness in agreement with the DNS, presenting a value close to 3 at large τ and a significant increase with a reduction of the time shift. One can then conclude that intermittency effects associated with the small scales of the velocity field can be captured by the LES supplemented by the proposed model. Note that in figure 11 we have presented the evolution of the structure function for $St = 1$, but the same behaviour is obtained for the other values of Stokes number considered here.

We present in figure 12, $\langle \boldsymbol{a}_b^2 | \varepsilon_* \rangle$, the variance of the bubble acceleration conditioned on the value of the instantaneous value of the dissipation rate ε_* estimated from the stochastic model (4.7). It is observed that similar to the DNS results reported in the figure 7, the bubble acceleration from the LES with the model increases as $\varepsilon_*^{3/2}$ for large values of the dissipation rate, and is independent on ε_* for the small values of the latter. This behaviour shows that the acceleration of the bubbles in the weakly dissipative regions can be computed by the resolved contribution $\bar{\boldsymbol{a}}_b$, indicating the influence of the large-scale sweeps, while the largest fluctuation of the acceleration are correctly estimated with the stochastic model.

5. Conclusion

In this paper, we study the statistics of the acceleration and forces of micro-bubbles ($\eta > d_b$) subject to the drag and fluid inertia forces in a homogenous and isotropic turbulent flow. For small Stokes numbers, the two forces are commensurate and are found to be preferentially anti-aligned, whereas for larger Stokes numbers the drag force becomes negligible and the bubble acceleration is essentially given by the fluid inertia forces resulting in a bubble acceleration variance larger than for fluid tracers. We propose an analytical model, depending on the Stokes number, Reynolds number and the density ratio, describing qualitatively these observations. The model based on the spectral response of the bubble to the fluid fluctuations (similar to the Tchen theory) assumes firstly the shape for the frequency spectra of the fluid velocity along the bubble position (with a ω^{-2} power law), and secondly that the material derivative

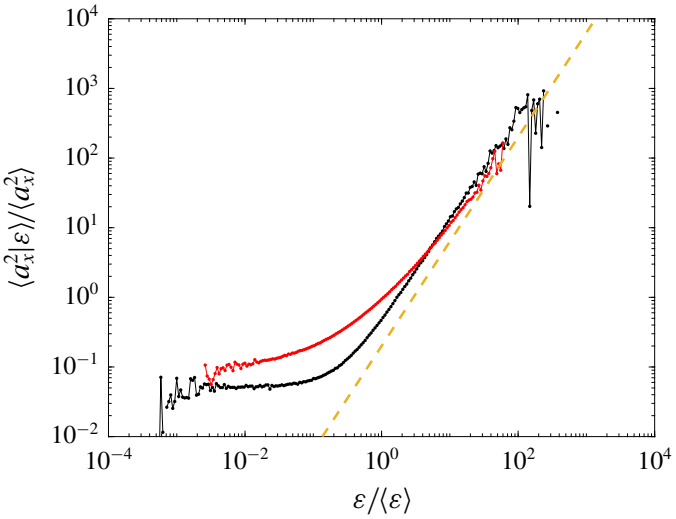

FIGURE 12. (Colour online) Variance of the total bubble acceleration $\boldsymbol{a}_b = \bar{\boldsymbol{a}}_b + \boldsymbol{a}_*$ conditioned on the stochastic value of the dissipation rate ε_* obtained from the LES with the stochastic model (black line) and comparison with the bubble acceleration variance conditioned on the local dissipation rate obtained from the DNS (red line), with $St = 0.02$ and a mesh size of 48^3 for the LES.

of the fluid velocity at the bubble position can be substituted by the time derivative along the bubble trajectories. These assumptions lead to fairly accurate estimations for small St, and some deviations are observed for $St \approx 1$ as the preferential concentration of bubbles is not accounted for. This effect could be taken into account in the model, by providing more precise, St dependent, estimation of the high frequency part of the Lagrangian fluid velocity spectra and of the fluid acceleration variance at the bubble position. It is further observed that the micro-bubble acceleration conditioned on the local dissipation rate presents a surprising invariance. For values of the local dissipation rate similar or larger than the average one, the conditional acceleration variance appears to be invariant with the Stokes number and increases with the dissipation rate, whereas the conditional p.d.f. are observed to be nearly invariant with the dissipation rate and the Stokes number when normalized by the conditional variance. Such invariance was not expected because of the very intense clustering of the bubbles reported by Calzavarini *et al.* (2008) around $St = 1$. Indeed, at small Stokes number the bubbles behave like fluid tracers, whereas for Stokes numbers of order 1 (for which one can neglect the drag force) the acceleration of a bubble is roughly $\beta = 3$ times that of a tracer at the same position. Nevertheless the near invariance of the conditional statistics implies that in the two cases the bubbles sample fluid regions in which the fluid acceleration conditional statistics are the same as in the entire domain. This observation can provide some help in studying the β and St dependence of the clustering morphology of the bubbles presented by Calzavarini *et al.* (2008).

Based on these observations, we propose, within the LES framework, an extension of the approach of Gorokhovski & Zamansky (2018) in order to account for the unresolved fluid turbulent fluctuations in the dynamics of micro-bubbles for locally homogenous and isotropic high-Reynolds numbers flows. To this end, the instantaneous acceleration of the bubble is decomposed into a filtered contribution given by the resolved fluid velocity field and a random contribution. The stochastic part is given by the sum of two correlated random processes, one for the drag forces

and the second for the fluid inertia terms. For the instantaneous norm of both forces, we consider the fluctuations of the energy transfer rate, relying on the fact that the fluctuations of the norm are self-similar for a given value of the energy transfer rate. For the latter a surrogate is obtained by a log-normal stochastic process evolving along the bubble trajectory. Whereas the former, which is observed to be invariant, is estimated from the variance of the forces conditioned on the dissipation rate as obtained from the model derived in this paper. The residual part is supplemented by a stochastic process for the orientations of the two forces. The model is given by two coupled random walks on the surface of the unit sphere, which enables us to reproduce the progressive decorrelation of the force components, their correlation with the large-scale motion, as well as the return to local isotropy for sufficiently large-scale separation, and the preferential anti-alignment of the two forces observed for $St < 1$. To summarize, the model depends on the Stokes number and the β parameter of the bubbles as well as a local Reynolds number Re_Δ based on the mesh size. In addition few parameters of the model need to be prescribed from the DNS.

The comparisons of the statistics obtained with LES supplemented by the proposed stochastic model with the ones obtained from DNS confirmed that the dynamics of the bubbles can be accurately computed by this approach even for very coarse meshes while the standard LES approach (without stochastic modelling for the high frequency fluctuations) fails to reproduce the statistics of the DNS. Nevertheless, the bubble clustering at subgrid scales or short-time relative dispersion are not improved by the modelling presented in this paper because the estimation of the dissipation rates along each bubble trajectory is obtained by independent stochastic processes.

The derivation of the proposed model is made for arbitrary density ratio, although, in this paper we only focus on the micro-bubble regime ($\beta = 3$). It can be shown that for $\beta = 0$ our model becomes equivalent to the formulation proposed for inertial particles in Gorokhovski & Zamansky (2018). Moreover, for neutrally dense particles ($\beta = 1$), the proposed model would provide results equivalent to those obtained for vanishingly small Stokes number, as expected for particles much smaller than the Kolmogorov scales. The assessment of the model for intermediate values of β is also interesting but is postponed for future work. Also interesting is to account for other forces that can have a non-negligible role on the bubble dynamics (buoyancy, lift and history). As well, accounting for the deformation of the bubbles is necessary if one is interested in bubbles larger than the micro-scale of the flow ($d_b > \eta$). Finally, we have focused on the modelling of the subgrid scale for homogenous and isotropic turbulent flow. Nevertheless, we think that the model proposed in this paper could provide acceptable results for flows that can be considered locally isotropic and homogenous at the scale of the mesh, since the main parameters of the model are defined locally.

Acknowledgements

The authors are grateful to M. Gorokhovski for enlightening discussions. This work was performed using high-performance computing resources from GENCI-CINES and CALMIP Center of the University of Toulouse.

REFERENCES

Bec, J., Biferale, L., Boffetta, G., Celani, A., Cencini, M., Lanotte, A., Musacchio, S. & Toschi, F. 2006 Acceleration statistics of heavy particles in turbulence. *J. Fluid Mech.* **550**, 349–358.

BEC, J., BIFERALE, L., CENCINI, M., LANOTTE, A. & TOSCHI, F. 2010 Intermittency in the velocity distribution of heavy particles in turbulence. *J. Fluid Mech.* **646**, 527–536.

BERROUK, A. S., LAURENCE, D., RILEY, J. J. & STOCK, D. E. 2007 Stochastic modelling of inertial particle dispersion by subgrid motion for les of high Reynolds number pipe flow. *J. Turbul.* **8**, N50.

BOS, W. J. T. & ZAMANSKY, R. 2019 Power fluctuations in turbulence. *Phys. Rev. Lett.* **122** (12), 124504.

BREUER, M. & HOPPE, F. 2017 Influence of a cost–efficient Langevin subgrid-scale model on the dispersed phase of large–eddy simulations of turbulent bubble–laden and particle–laden flows. *Intl J. Multiphase Flow* **89**, 23–44.

BURTON, G. C. & DAHM, W. J. A. 2005*a* Multifractal subgrid-scale modeling for large-eddy simulation. I. Model development and *a priori* testing. *Phys. Fluids* **17**, 075111.

BURTON, G. C. & DAHM, W. J. A. 2005*b* Multifractal subgrid-scale modeling for large-eddy simulation. II. Backscatter limiting and a posteriori evaluation. *Phys. Fluids* **17**, 075112.

CALZAVARINI, E., KERSCHER, M., LOHSE, D. & TOSCHI, F. 2008 Dimensionality and morphology of particle and bubble clusters in turbulent flow. *J. Fluid Mech.* **607**, 13–24.

CALZAVARINI, E., VOLK, R., BOURGOIN, M., LÉVÊQUE, E., PINTON, J.-F. & TOSCHI, F. 2009 Acceleration statistics of finite-sized particles in turbulent flow: the role of Faxén forces. *J. Fluid Mech.* **630**, 179–189.

CASTAING, B. 1996 The temperature of turbulent flows. *J. Phys. II* **6**, 105–114.

CASTAING, B., GAGNE, Y. & HOPFINGER, E. J. 1990 Velocity probability density functions of high Reynolds number turbulence. *Physica* D **46** (2), 177–200.

CHEN, S., DOOLEN, G. D., KRAICHNAN, R. H. & SHE, Z.-S. 1993 On statistical correlations between velocity increments and locally averaged dissipation in homogeneous turbulence. *Phys. Fluids* **5** (2), 458–463.

CLIMENT, E. & MAGNAUDET, J. 1999 Large-scale simulations of bubble-induced convection in a liquid layer. *Phys. Rev. Lett.* **82**, 4827–4830.

DHOTRE, M. T., DEEN, N. G., NICENO, B., KHAN, Z. & JOSHI, J. B. 2013 Large eddy simulation for dispersed bubbly flows: a review. *Intl J. Chem. Engng* **2013**, 343276.

FEDE, P. & SIMONIN, O. 2006 Numerical study of the subgrid fluid turbulence effects on the statistics of heavy colliding particles. *Phys. Fluids* **18** (4), 045103.

GATIGNOL, R. 1983 The Faxén formulae for a rigid particle in an unsteady non-uniform Stokes flow. *J. Méc. Théor. Appl.* **1**, 143–160.

GHATE, A. S. & LELE, S. K. 2017 Subfilter-scale enrichment of planetary boundary layer large eddy simulation using discrete fourier–gabor modes. *J. Fluid Mech.* **819**, 494–539.

GOROKHOVSKI, M. & ZAMANSKY, R. 2018 Modeling the effects of small turbulent scales on the drag force for particles below and above the Kolmogorov scale. *Phys. Rev. Fluids* **3** (3), 1–23.

VAN DEN HENGEL, E. I. V., DEEN, N. G. & KUIPERS, J. A. M. 2005 Application of coalescence and breakup models in a discrete bubble model for bubble columns. *Ind. Engng Chem. Res.* **44** (14), 5233–5245.

HINZE, J. O. 1975 *Turbulence*, 2nd edn. McGraw-Hill.

HU, G. & CELIK, I. 2008 Eulerian–Lagrangian based large-eddy simulation of a partially aerated flat bubble column. *Chem. Engng Sci.* **63** (1), 253–271.

JOHNSON, P. L. & MENEVEAU, C. 2017 Predicting viscous-range velocity gradient dynamics in large-eddy simulations of turbulence. *J. Fluid Mech.* **837**, 80–114.

KERSTEIN, A. R. 1999 One-dimensional turbulence: model formulation and application to homogeneous turbulence, shear flows, and buoyant stratified flows. *J. Fluid Mech.* **392**, 277–334.

KOLMOGOROV, A. N. 1941 The local structure of turbulence in incompressible viscous fluid for very large Reynolds numbers. *Dokl. Akad. Nauk SSSR* **434**, 9–13, translation by V. Levin 1991 *Phil. Trans. R. Soc. Lond.* A **434**, 9–13.

KOLMOGOROV, A. N. 1962 A refinement of previous hypotheses concerning the local structure of turbulence in a viscous incompressible fluid at high Reynolds number. *J. Fluid Mech.* **13**, 82–85.

LALESCU, C. C. & WILCZEK, M. 2018 Acceleration statistics of tracer particles in filtered turbulent fields. *J. Fluid Mech.* **847**, R2.

LANOTTE, A., CALZAVARINI, E., TOSCHI, F., BEC, J., BIFERALE, L. & CENCINI, M. 2011 Heavy particles in turbulent flows. International CFD Database, RM-2007-GRAD-2048.St0. iCFDdatabase.

LEGENDRE, D. & MAGNAUDET, J. 1997 A note on the lift force on a spherical bubble or drop in a low-Reynolds-number shear flow. *Phys. Fluids* **9** (11), 3572–3574.

LEGENDRE, D. & MAGNAUDET, J. 1998 The lift force on a spherical bubble in a viscous linear shear flow. *J. Fluid Mech.* **368**, 81–126.

LOISY, A. & NASO, A. 2017 Interaction between a large buoyant bubble and turbulence. *Phys. Rev. Fluids* **2**, 014606.

LUKASSEN, L. J. & WILCZEK, M. 2017 Lagrangian intermittency based on an ensemble of Gaussian velocity time series. In *Progress in Turbulence VII* (ed. R. Örlü, A. Talamelli, M. Oberlack & J. Peinke), pp. 23–29. Springer International Publishing.

MAGNAUDET, J. & EAMES, I. 2000 The motion of high-Reynolds-number bubbles in inhomogeneous flows. *Annu. Rev. Fluid Mech.* **32**, 659–708.

MATHAI, V., CALZAVARINI, E., BRONS, J., SUN, C. & LOHSE, D. 2016 Microbubbles and microparticles are not faithful tracers of turbulent acceleration. *Phys. Rev. Lett.* **117**, 024501.

MAXEY, M. R. & RILEY, J. J. 1983 Equation of motion for a small rigid sphere in a nonuniform flow. *Phys. Fluids* **26** (4), 883–889.

MAZZITELLI, I. M. & LOHSE, D. 2004 Lagrangian statistics for fluid particles and bubbles in turbulence. *New J. Phys.* **6** (1), 203.

MAZZITELLI, I. M., LOHSE, D. & TOSCHI, F. 2003 On the relevance of the lift force in bubbly turbulence. *J. Fluid Mech.* **488**, 283–313.

MENEVEAU, C. & KATZ, J. 2000 Scale-invariance and turbulence models for large-eddy simulation. *Annu. Rev. Fluid Mech.* **32**, 1–32.

MINIER, J.-P., CHIBBARO, S. & POPE, S. B. 2014 Guidelines for the formulation of Llagrangian stochastic models for particle simulations of single-phase and dispersed two-phase turbulent flows. *Phys. Fluids* **26**, 113303.

MORDANT, N., CRAWFORD, A. M. & BODENSCHATZ, E. 2004 Three-dimensional structure of the Lagrangian acceleration in turbulent flows. *Phys. Rev. Lett.* **93** (21), 214501.

MORDANT, N., METZ, P. & MICHEL, O. 2001 Measurement of Lagrangian velocity in fully developed turbulence. *Phys. Rev. Lett.* **21**, 214501.

PARK, G. I., BASSENNE, M., URZAY, J. & MOIN, P. 2017 A simple dynamic subgrid-scale model for les of particle-laden turbulence. *Phys. Rev. Fluids* **2** (4), 044301.

PEREIRA, R. M., MORICONI, L. & CHEVILLARD, L. 2018 A multifractal model for the velocity gradient dynamics in turbulent flows. *J. Fluid Mech.* **839**, 430–467.

POPE, S. B. 1990 Lagrangian microscales in turbulence. *Phil. Trans. R. Soc. Lond.* A **333** (1631), 309–319.

POPE, S. B. & CHEN, Y. L. 1990 The velocity-dissipation probability density function model for turbulent flows. *Phys. Fluids* **2** (8), 1437–1449.

POZORSKI, J. & APTE, S. V. 2009 Filtered particle tracking in isotropic turbulence and stochastic modeling of subgrid-scale dispersion. *Intl J. Multiphase Flow* **35** (2), 118–128.

PRAKASH, V. N. 2013 Light particles in turbulence. PhD thesis, University of Twente, Enschede.

PRAKASH, V. N., TAGAWA, Y., CALZAVARINI, E., MERCADO, J. M., TOSCHI, F., LOHSE, D. & SUN, C. 2012 How gravity and size affect the acceleration statistics of bubbles in turbulence. *New J. Phys.* **14** (10), 105017.

SABELNIKOV, V., BARGE, A. & GOROKHOVSKI, M. 2019 Stochastic modeling of fluid acceleration on residual scales and dynamics of suspended inertial particles in turbulence. *Phys. Rev. Fluids* **4** (4), 044301.

SABEL'NIKOV, V., CHTAB, A. & GOROKHOVSKI, M. 2007 The coupled LES – sub-grid stochastic acceleration model (LES-SSAM) of a high Reynolds number flows. In *Advances in Turbulence XI*, vol. 117, pp. 209–211; 11th EUROMECH European Turbulence Conference, June 25–28, 2007, Porto, Portugal: Springer Proceedings in Physics.

SABEL'NIKOV, V., CHTAB-DESPORTES, A. & GOROKHOVSKI, M. 2011 New sub-grid stochastic acceleration model in LES of high-Reynolds-number flows. *Eur. Phys. J.* B **80** (2), 177–187.

SAGAUT, P. 2002 *Large Eddy Simulation for Incompressible Flows: An Introduction*, 2nd edn. Springer.

SAWFORD, B. L. 1991 Reynolds number effects in Lagrangian stochastic models of turbulent dispersion. *Phys. Fluids* A **3**, 1577–1588.

SAWFORD, B. L. & GUEST, F. M. 1991 Lagrangian statistical simulation of the turbulent motion of heavy particles. *Boundary-Layer Meteorol.* **54** (1–2), 147–166.

SAWFORD, B. L. & YEUNG, P. K. 2011 Kolmogorov similarity scaling for one-particle Lagrangian statistics. *Phys. Fluids* **23** (9), 091704.

TAGAWA, Y., MERCADO, J. M., PRAKASH, V. N., CALZAVARINI, E., SUN, C. & LOHSE, D. 2012 Three-dimensional Lagrangian Voronoï analysis for clustering of particles and bubbles in turbulence. *J. Fluid Mech.* **693**, 201–215.

TAGAWA, Y., ROGHAIR, I., PRAKASH, V. N., VAN SINT ANNALAND, M., KUIPERS, H., SUN, C. & LOHSE, D. 2013 The clustering morphology of freely rising deformable bubbles. *J. Fluid Mech.* **721**, R2.

TCHEN, C. M. 1947 Mean value and correlation problems connected with the motion of small particles suspended in a turbulent fluid. PhD thesis, Delft University, Netherlands.

TENNEKES, H. & LUMLEY, J. L. 1972 *A First Course in Turbulence*. MIT Press.

VOLK, R., CALZAVARINI, E., VERHILLE, G., LOHSE, D., MORDANT, N., PINTON, J.-F. & TOSCHI, F. 2008*a* Acceleration of heavy and light particles in turbulence: comparison between experiments and direct numerical simulations. *Physica* D **237** (14–17), 2084–2089.

VOLK, R., MORDANT, N., VERHILLE, G. & PINTON, J.-F. 2008*b* Laser doppler measurement of inertial particle and bubble accelerations in turbulence. *Eur. Phys. Lett.* **81**, 34002.

YEUNG, P. K. 2001 Lagrangian characteristics of turbulence and scalar transport in direct numerical simulations. *J. Fluid Mech.* **427**, 241–274.

YEUNG, P. K., POPE, S. B., LAMORGESE, A. G. & DONZIS, D. A. 2006 Acceleration and dissipation statistics of numerically simulated isotropic turbulence. *Phys. Fluids* **18**, 065103.

ZAICHIK, L. I. & ALIPCHENKOV, V. M. 2011 A model for predicting the acceleration variance of arbitrary-density finite-size particles in isotropic turbulence. *Intl J. Multiphase Flow* **37** (3), 236–240.

ZAMANSKY, R., COLETTI, F., MASSOT, M. & MANI, A. 2016 Turbulent thermal convection driven by heated inertial particles. *J. Fluid Mech.* **809**, 390–437.

ZAMANSKY, R., VINKOVIC, I. & GOROKHOVSKI, M. 2013 Acceleration in turbulent channel flow: universalities in statistics, subgrid stochastic models and an application. *J. Fluid Mech.* **721**, 627–668.

Chapter 6

Influence of nonlinear drag law to the bubble dynamics

In this chapter, we will discuss the nonlinear drag law effects to the bubble dynamics (mostly the velocity and acceleration statistics). The results will enable to extend the scope of the modeling proposed in the previous chapter to larger bubbles Reynolds number for which the Stokes regime does not holds.

6.1 Statement of the problem

Let's clarify first the definition of linear drag and nonlinear drag. From the definition of the drag coefficient and the viscous relaxation time, the drag force per unit of displaced mass (i.e. accounting for added mass effect) can generally be expressed as:

$$\boldsymbol{F}_D = C_D Re_b \frac{\boldsymbol{u}_f - \boldsymbol{u}_b}{\tau_0} \tag{6.1}$$

where $\boldsymbol{u}_f$ is the velocity of the fluid at the position of the bubble and $\boldsymbol{u}_b$ is the bubble velocity and the characteristic time is $\tau_0 = \frac{4}{3}(\frac{\rho_b}{\rho_f} + C_M)\frac{d_b^2}{\nu}$. As discussed previously the drag coefficient of a bubble depends essentially on the Reynolds number $Re_b = d_b|\boldsymbol{u}_f - \boldsymbol{u}_b|/\nu$ and on the mobility of the interface (no-slip or free slip). For example, in the Stokes regimes ($Re_b \ll 1$), the drag coefficient varies as $C_D = 24/Re_b$ in case of no-slip or as $C_D = C_{D,0} = 16/Re_b$ for free-slip conditions, which gives the standard drag law for a clean bubble in Stokes regime, obtained by Hadamard and Ribczynsky in 1911 [56, 57]. This is sometimes called linear drag law

as the resulting drag force varies linearly with the relative velocity. In the following, we only consider the case of bubbles and we will therefore take the limit $\rho_b/\rho_f = 0$. We recall that for a clean spherical bubble (with free-slip condition and $C_M = 1/2$) the relaxation time was defined as $\tau_b = d_b^2/24\nu = \tau_0/C_{D,0}Re_b$. For larger value of the Reynolds number the drag coefficient varies as presented by the correlation of (3.9) for no-slip, corresponding to a fully contaminated bubble interface and the correlation of Mei for free slip, corresponding to a clean bubble interface, see equations (3.9) and (3.8) above. These drag laws are denoted as non-linear as the drag force no longer varies linearly with the relative velocity. Equation (6.1) can be re-expressed as:

$$\boldsymbol{F}_D = \frac{C_D}{C_{D,0}} \frac{\boldsymbol{u}_f - \boldsymbol{u}_b}{\tau_b} \tag{6.2}$$

where τ_b is the relaxation time of a clean bubble and $C_{D,0} = 16/Re_b$ is the drag coefficient in the stokes regime for free-slip conditions. As apparent from this equation, in this section we intend to study how the deviation of the drag coefficient from the Stokes regime affect the dynamics of the bubbles. For convenience we note $\mathcal{F}(Re_b) = \dfrac{C_D}{C_{D,0}}$. We will consider three expressions for $\mathcal{F}(Re_b)$. The Stokes regime ($Re_b < 1$):

$$\mathcal{F}(Re_b) = 1 \tag{6.3}$$

will be our reference, and correspond to the results obtained in the previous chapter. The no-slip correction:

$$\mathcal{F}(Re_b) = (1 + 0.15Re_b^{0.687}) \tag{6.4}$$

corresponds to a bubble with a fully contaminated interface for $Re_b < 800$ [39]. The free-slip case:

$$\mathcal{F}(Re_b) = 1 + \left(\frac{8}{Re_b} + \frac{1}{2}\Big(1 + \frac{3.315}{\sqrt{Re_b}}\Big) \right)^{-1} \tag{6.5}$$

is the correction to account for the modification of the drag coefficient at large Reynolds number for a clean bubble. In figure 6.1, the function $\mathcal{F}(Re_b)$ is plotted for the last two cases. We clearly see that $\mathcal{F} \geq 1$ which implies that the drag is larger than the Stokes drag would be at the same Reynolds number.

Since the Reynolds number can fluctuate along the bubble trajectory, the correction function, $\mathcal{F}(Re_b)$, also takes random values which will affect the dynamic of the bubble. In order to investigate the influence of the fluctuations of $\mathcal{F}$, we performed DNS with the various expressions proposed above, see eq. (6.3)-(6.5). In these simulations we only accounted for the drag

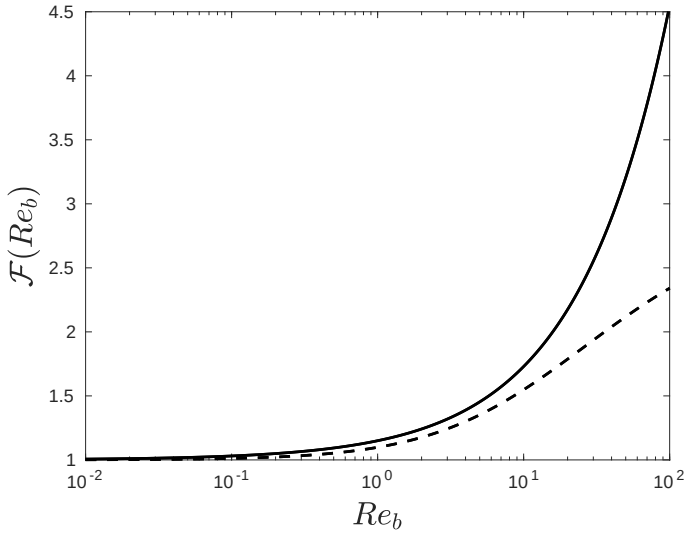

Figure 6.1: Function $\mathcal{F}(Re_b)$ from Eq. (6.3) (- -) and from Eq. (6.4)(–).

force and the fluid inertia effect, therefore the bubble momentum balance equation reads:

$$\boldsymbol{a}_b = \frac{d\boldsymbol{u}_b}{dt} = \frac{\boldsymbol{u}_f - \boldsymbol{u}_b}{\tau_b}\mathcal{F}(Re_b) + 3\frac{D\boldsymbol{u}_f}{Dt} \tag{6.6}$$

We believe that this simplified equation of motion is sufficient for a first analysis of the finite Reynolds number effects. The flow conditions are identical to the simulations of the three sets of bubbles and are reported in the table 6.1. The bubble diameters normalized by the Kolmogorov scales are listed in table 6.2. As well we define a Stokes number based on the "Stokesian clean bubble" characteristic time τ_b, $St = \tau_b/\tau_\eta$. However it is to note that for large bubble Reynolds number $\mathcal{F}$ becomes significantly larger than 1 and fluctuates therefore τ_b is not physically meaningful.

N	Re_H	Re_λ	τ_L/τ_η	$\frac{\langle\varepsilon\rangle H}{\mathcal{K}^{3/2}}$	L/η	η/Δ
512^3	2475	100	26	1.97	133	1.06

Table 6.1: The simulation parameters of the turbulent flow field, N is the number of grid points in each direction. $H = 2\pi$ is the size of numerical domain, $\tau_L = (2/3\mathcal{K})/\varepsilon$ is the eddy turnover time, $L = (2/3\mathcal{K})^{3/2}/\varepsilon$ is the scale of the large eddies, $\mathcal{K}$ is the average turbulent kinetic energy and ε is the average dissipation rate. Re_H is the Reynolds number based on the large scale of the flow, Re_λ is the Reynolds number based on the Taylor length scale, η and τ_η are the Kolmogorov length and time scale.

St	0.021	0.074	0.20	0.45	1.01	1.55	2.07
d_b/η	0.70	1.33	2.19	3.29	4.93	6.10	7.04

Table 6.2: The Stokes number of the bubble is defined as $St = \frac{\tau_b}{\tau_\eta}$ with $\tau_b = \frac{d_b^2}{24\nu}$ and τ_η is the Kolmogorov dissipative time scale, d_b is the diameter of the spherical bubble

6.2 Results

We first present the statistics of the bubbles Reynolds number. We present in figure 6.2 the evolution of the mean and standard deviation of the Reynolds number with St for the three drag law (Eq. (6.3), (6.4) and (6.5)). As expected, the relative velocity increases with the Stokes number, and both quantities are shown to increase almost linearly with St, for the range of St studied here at least, for the three drag laws. As apparent for $St > 1$, it appears that the Reynolds number can be significantly larger than 1 which confirms as discuss in the previous chapter than the drag law for Stokes regime is not valid for bubbles with large Stokes number. We also remark that the RMS is of the order of the average. Finally, when we compare the curve for the various drag laws, we can conclude that for a fixed bubble size, or St value, the relative velocity is larger with the drag law in the Stokes regime and the relative velocity is the smallest in the no-slip case.

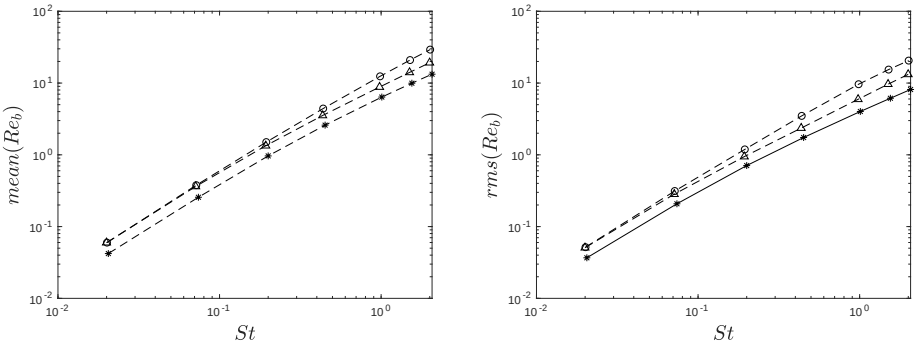

Figure 6.2: (left) mean (right) root-mean-square of the bubble Reynolds number for the three drag law considered here as a function of the Stokes number, $St = (d_b/24\eta)^2$. ($\circ$) obtained with the drag law for clean bubbles in Stokes regime (6.3) ($*$) obtained with drag law (6.4), ($\triangle$) obtained with drag law (6.5), such that the root-mean-square value of both distribution is unity.

In figure 6.3 we show the *pdf* of the bubble Reynolds number obtained in the case of the slip drag law (6.5). It is observed that the form of the *pdf*

of Re_b normalized by its standard deviation depends weakly on the Stokes number. With increasing St, the probability of having large fluctuations of Re_b reduces a bit. But overall, the distribution is quite close to the log-normal distribution. Therefore, we could say that the bubble Reynolds number presents intermittent fluctuations. This is confirmed by comparing the Maxwell distribution, which corresponds to the norm of a vector having a Gaussian distribution.

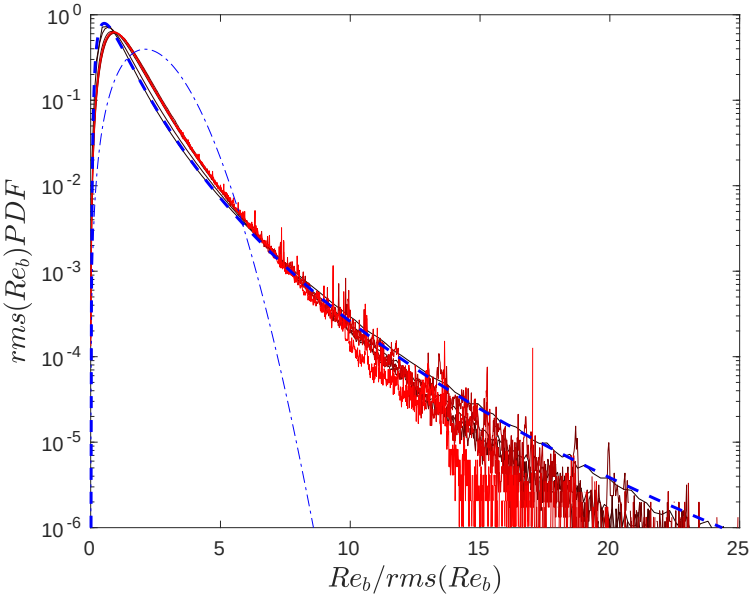

Figure 6.3: The *pdf* of Re_b from the simulation for non-linear drag force (clean bubble) and inertia force, with different St from black to red as the Stokes number increases. (- -) is a *pdf* of log-normal distribution with parameters of $\sigma^2 = \ln 2$, $\mu = -\sigma^2/2$, (- ·) is a *pdf* of Maxwell distribution with parameter $a = \sqrt{\frac{\pi}{3\pi-8}}$

We now present in figure 6.4 the influence of the drag law on the statistics of the drag forces. We can see in this figure that despite the reduction of the relative velocity reported previously, both the mean and the standard deviation of the drag forces increase when considering the non-linear drag compared to the linear drag.

We now propose to redefine the characteristic relaxation time to account for the finite bubble Reynolds number effect on the dynamics. As will be shown later, this new time scale enables to obtain a behavior similar to the one found for Stokes regime, for various statistical quantities. We proceed

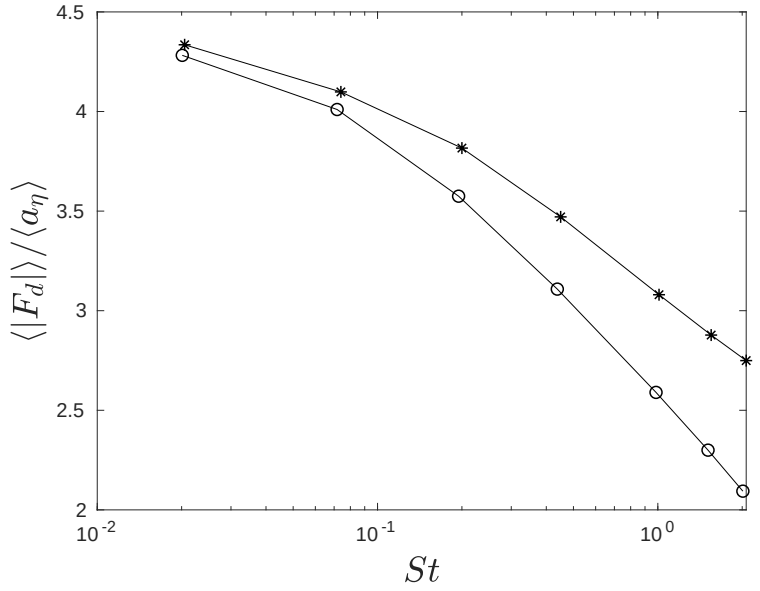

Figure 6.4: Mean value of drag force amplitude normalized by the Kolmogorov acceleration scale versus the Stokes number. ($\circ$) obtained with drag law for Stokes regime (6.3) ($*$) obtained with no-slip surface bubble law(6.4).

as follows. We decompose the bubble Reynolds number into its mean and fluctuating part: $Re_b = \langle Re_b \rangle + Re'_b$. And using a Taylor expansion of the function $\mathcal{F}$ around $\mathcal{F}(\langle Re_b \rangle)$ we can write

$$\mathcal{F}(Re_b) = \mathcal{F}(\langle Re_b \rangle) + Re'_b \mathcal{F}'(\langle Re_b \rangle) + \dots \tag{6.7}$$

with $\mathcal{F}'(\langle Re_b \rangle) = \left. \dfrac{d\mathcal{F}}{dRe_b} \right|_{Re_b = \langle Re_b \rangle}$. The drag force, can therefore be expressed as:

$$\boldsymbol{F}_D = \frac{\boldsymbol{u}_f - \boldsymbol{u}_b}{\tau_b^*} + Re'_b \mathcal{F}'(\langle Re_b \rangle) \frac{\boldsymbol{u}_f - \boldsymbol{u}_b}{\tau_b} + \dots \tag{6.8}$$

where we introduce the redefined characteristic time τ_b^*:

$$\tau_b^* = \tau_b / \mathcal{F}(\langle Re_b \rangle) \tag{6.9}$$

It is worth mentioning that this time scale does not fluctuate in time and remains constant. This is contrary to the proposition of [24], who have introduced a random relaxation time scale. Namely, for the drag law in the Stokes regime, we have:

$$\tau_b^* = \tau_b \tag{6.10}$$

while for the bubble with contaminated interface, we found:

$$\tau_b^* = \frac{R^2}{9\nu}\left(1 + 0.15\langle Re_b\rangle^{0.687}\right)^{-1} \tag{6.11}$$

and for a clean bubbles interface:

$$\tau_b^* = \frac{R^2}{6\nu}\left[1 + \left(\frac{8}{\langle Re_b\rangle} + \frac{1}{2}\left(1 + \frac{3.315}{\sqrt{\langle Re_b\rangle}}\right)\right)^{-1}\right]^{-1} \tag{6.12}$$

We will show latter how to estimate the value of $\langle Re_b\rangle$ and thus to obtain an a priori estimation of τ_b^*. In order to neglect the fluctuations of Re_b in the evolution of $\mathcal{F}(Re_b)$, we compare the magnitude of the second order and the first order term in Eq. (6.8). We plot in figure 6.5 the ratio $\frac{\langle Re_b\rangle \mathcal{F}'(\langle Re_b\rangle)}{\mathcal{F}(\langle Re_b\rangle)}$ against $\langle Re_b\rangle$. Note that we have estimated the order of magnitude of the fluctuations of Re_b as $\mathcal{O}(Re_b') = \langle Re_b\rangle$. We found that, in the simulation for free slip bubble using drag law (6.5), the largest value for the ratio is 0.2 and it is found for the bubble with $St = 1.55$, and in the simulation for no-slip surface bubble using drag law (6.5), the largest ratio 0.32 is found for the bubble with $St = 2.06$. This confirms that the second term on the right-hand side of (6.8) is negligible when focusing on the low order moments of the statistics of $\boldsymbol{F}_D$. This is also confirmed in figure 6.6 which presents the mean and variance of the norm of the relative velocity against $St^* = \tau_b^*/\tau_\eta$ for the three drag laws considered here. We observe that the three curves present a relatively good collapse. As well, figure 6.7 shows that the mean and standard deviation of the norm of the drag force present the same evolution for the non-linear drag law as the drag law for Stokes regime when plotted against St^*.

The bubble acceleration variance is reduced when taking account for the nonlinear drag law compared to the case of the drag law of Stokes regime, as presented in figure 6.9. With the increase of St, the drag force becomes more and more reduced. This may appear surprising since we observed that the drag force variance was increased when considering one of the non-linear drag laws. The explanation can be found in the correlation between the fluid inertia force and the drag force, already discussed in Chapter 5. The variance of the bubble acceleration can be decomposed as $\langle a_b^2\rangle = \langle F_D^2\rangle + 2\langle F_D F_I\rangle + \langle F_I^2\rangle$, and it appears that with the non-linear drag law the two forces are more anti-correlated, see cross-correlation between two forces in figure 6.12. In the meantime, the increase of the variance of the drag force remains small such that the sum $\langle F_D^2\rangle + 2\langle F_D F_I\rangle$ is reduced when applying the non-linear drag laws, explaining the reduction of the bubble acceleration variance.

Similarly, to the previous analysis of the statistics of the drag forces, when plotting the evolution of the acceleration variance as a function of the ef-

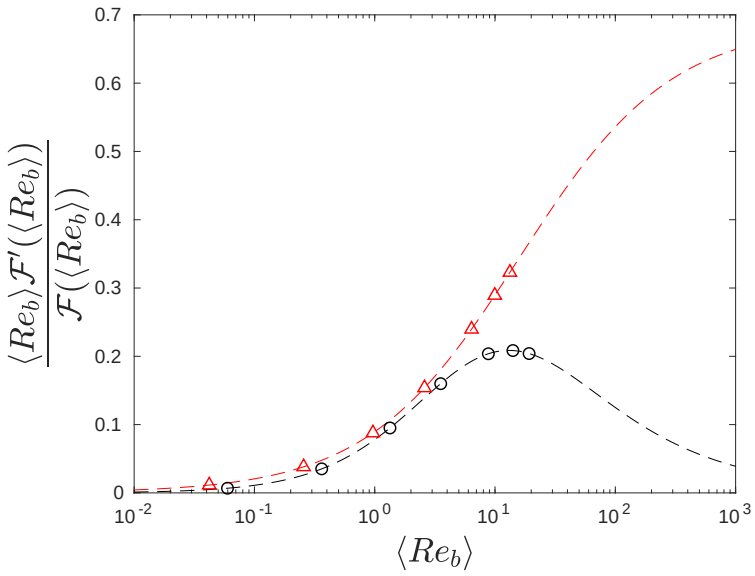

Figure 6.5: The ratio between the second term on the right-hand side of (6.8) to the first term $\frac{\langle Re_b\rangle \mathcal{F}'(\langle Re_b\rangle)}{\mathcal{F}(\langle Re_b\rangle)}$ against $\langle Re_b\rangle$, ($\triangle$) simulation with no-slip surface bubble law (6.4), ($\circ$) simulation with slip surface bubble law(6.5). (- -) Analytical results of (6.8) for (red) (6.4) and (black) (6.5).

fective relaxation time τ_b^*, it is observed in figure 6.9 that the curves of the three drag laws almost collapse when plotted with St^*. Therefore based on the estimation of the bubble acceleration variance obtained from the Tchen formula in the previous chapter, one can obtain an estimation of the acceleration variance when using the modified drag law by substituting St by St^* in formula (3.4) of Chapter 5.

It appears that the modification of the drag law has a more important influence to the higher order moment. In figure 6.10, the flatness of the bubble acceleration versus St presents the same tendency. The flatness increases firstly with St reaching a peak around $St = 0.5$ and then decrease for larger St. When the non-linear drag law is applied, the peak value is reduced and is shifted to larger St. As discuss in the previous chapter, the non-monotonous evolution of the flatness is primarily attributed to the randomness of the alignment between the two forces. When the two forces with commensurate magnitude are anti-aligned, the resulting acceleration is small. But if suddenly the forces tend to align, it results in a very strong acceleration. In case of the non-linear drag laws we measure that the anti-correlation between the two forces is stronger than with the drag law for

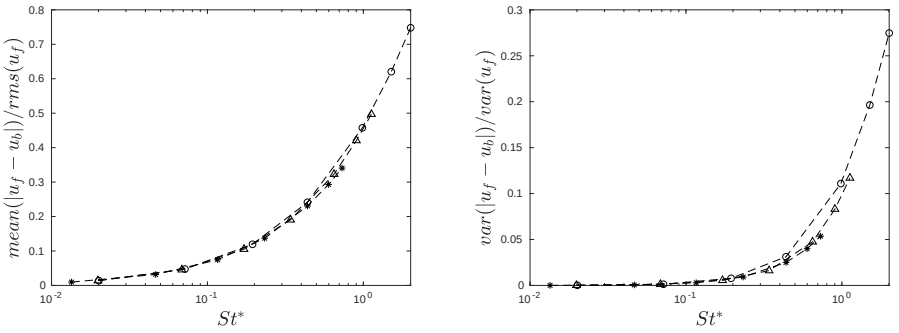

Figure 6.6: (Left) The mean value of the norm of the relative velocity normalized by the RMS of the fluid velocity, (right) The variance of the norm of the relative velocity normalized by the variance of the fluid velocity versus the modified Stokes number St^*. ($\circ$) obtained with drag law for Stokes regime (6.3) ($*$) obtained with no-slip surface bubble law (6.4), ($\triangle$) obtained with slip surface bubble law(6.5).

Stokes regime and therefore we think that the two forces are less prone to align. To confirm this point, we plot the *pdf*s of the cosine angle between the orientation of the drag force and fluid inertia force for both the simulations using slip bubble drag law (6.5) and the no-slip bubble drag law (6.4) in figure 6.8. The *pdf* of $\cos\theta$ for clean bubbles in the Stokes regime can be found in figure 5 of Chapter 5. As expected, the anti-correlation between the two forces with no-slip bubble drag law (6.4) is stronger than that with slip bubble drag law (6.5). Compared to the results of the drag law for clean bubbles in the Stokes regime in figure 5 of Chapter 5, the two forces of non-linear drag law are indeed less prone to align.

For completeness, we also present in figure 6.10 the evolution of the flatness versus St^*. We observe in this plot that the peak seems to occur for the same value of St^* which corroborate the previous explanations.

The nonlinear drag laws also have some influences on the Lagrangian statistics. The acceleration autocorrelation function for the three drags is presented in figure 6.11 for $St = 0.02$ and $St = 1$. It is observed that for small St the decorrelation of the acceleration remains quite similar for the three laws, but for $St = 1$ the Stokes regime drag laws gives the fastest decorrelation. This is attributed to the fact that the effective relaxation time τ_b^* is increased when using the non-linear drag laws.

We also present the cross-correlation function between these two forces in figure 6.12 for $St = 0.02$ and $St = 1$. Once again for $St = 0.02$ no signif-

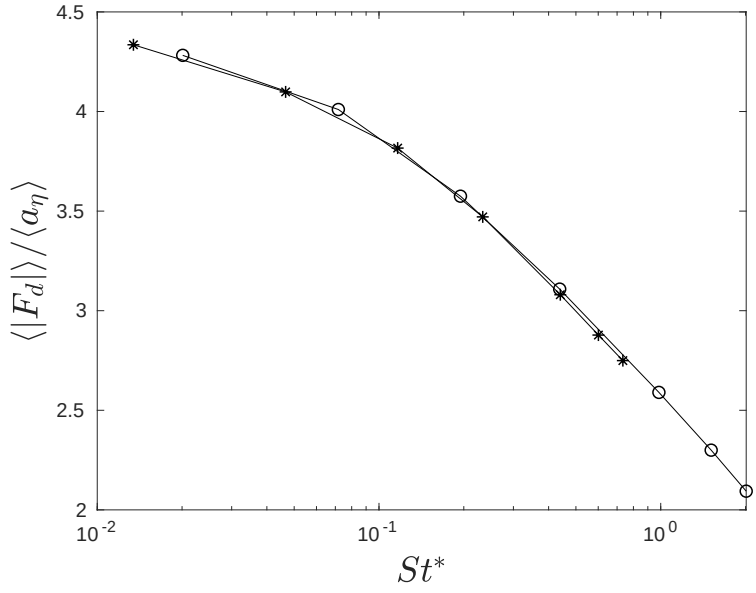

Figure 6.7: Mean value of the drag force amplitude normalized by the Kolmogorov acceleration scale versus the modified Stokes number St^*. ($\circ$) obtained with drag law for clean bubbles with Stokes regime (6.3), ($*$) obtained with no-slip surface bubble law (6.4).

icant difference is observed, as expected. But at $St = 1$, we see that with the non-linear drag law the two forces present stronger anti-correlation phenomenon, and the correlation time lag, defined as $\rho_{cross}(\tau_{lag}) = Max(\rho_{cross})$, is reduced. In figure 6.13, we plot the evolution of τ_{lag} for the three drag laws against St and St^*. We observe that the evolution of the time lag is similar when plotted against St^* which confirms once again that most of the effects of the Reynolds number correction to the drag law can be accounted for by a rescaling of the bubble relaxation time.

We now show how to estimate the value of St^* a priori, that is to say without the need to first compute the bubble trajectories with the DNS. In the previous chapter we have shown that from the Tchen theory we can predict fairly well the linear drag force variance, see the relation (3.6) and the figure 4 in Chapter 5. Therefore the relative velocity, for the Stokes regime drag case is readily estimated as

$$\langle (\boldsymbol{u}_f - \boldsymbol{u}_b)^2 \rangle = (St\tau_\eta)^2 c_0 a_\eta^2 \frac{(1-\beta)^2}{1 - St_0^2} \left(\frac{\tan^{-1}(c_1 St)}{c_1 St} - \frac{\tan^{-1}(c_1 Re_0^{1/2})}{c_1 Re_0^{1/2}} \right) \tag{6.13}$$

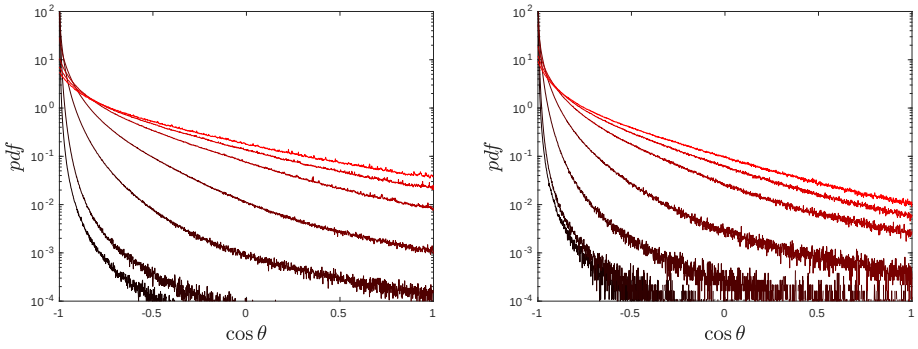

Figure 6.8: The *pdf*s of the cosine angle between the orientations of the drag force and fluid inertia force defined as $\cos\theta = \frac{F_I \cdot F_D}{|F_I||F_D|}$, (left) is obtained from the simulation using slip bubble drag law (6.5) and (right) is obtained from the simulation using the no-slip bubble drag law (6.4). For both figure, St = 0.02, 0.074, 0.020, 0.45, 1.01, 1.55 and 2.07 from black to red, respectively

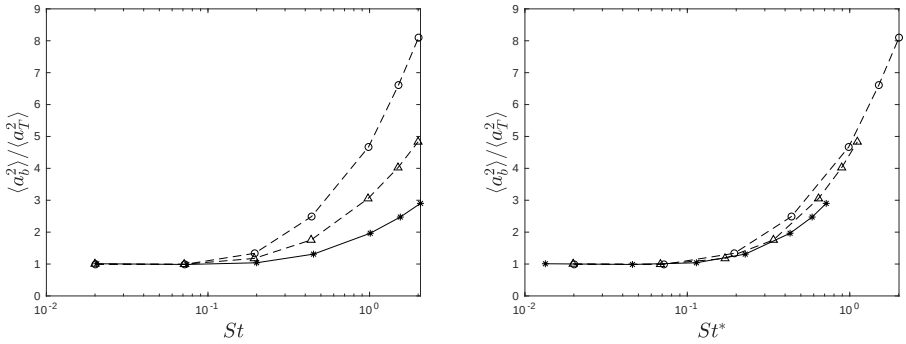

Figure 6.9: (Left) the variance of the bubble acceleration normalized by the Kolmogorov acceleration $a_\eta^2 = \epsilon^{3/4}\nu^{-1/4}$ versus St. (Right) the variance of the bubble acceleration normalized by the Kolmogorov acceleration $a_\eta^2 = \epsilon^{3/4}\nu^{-1/4}$ versus St^*. For both figures ($\circ$) is obtained with drag law for Stokes regime (6.3), ($*$) is obtained with no-slip surface bubble law (6.4), ($\triangle$)obtained with slip surface bubble law (6.5).

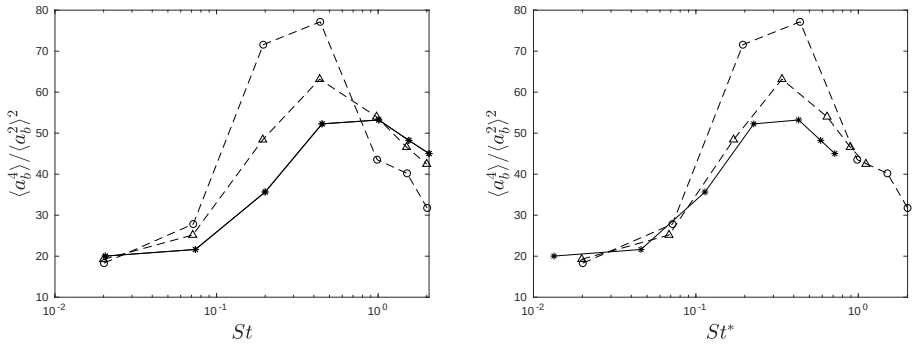

Figure 6.10: (Left) is the 4th order moment of the bubble acceleration normalized by the square value of the acceleration (flatness) versus St. (Right) is the variance of the material fluid acceleration $\frac{D\boldsymbol{u}_f}{Dt}$ at the position of the bubble normalized by the variance of Kolmogorov acceleration $a_\eta^2 = \epsilon^{3/4}\nu^{-1/4}$ versus St^*. For both figures ($\circ$) is obtained with drag law for Stokes regime (6.3), ($*$) is obtained with no-slip surface bubble law (6.4), ($\triangle$)obtained with a slip bubble interface law (6.5).

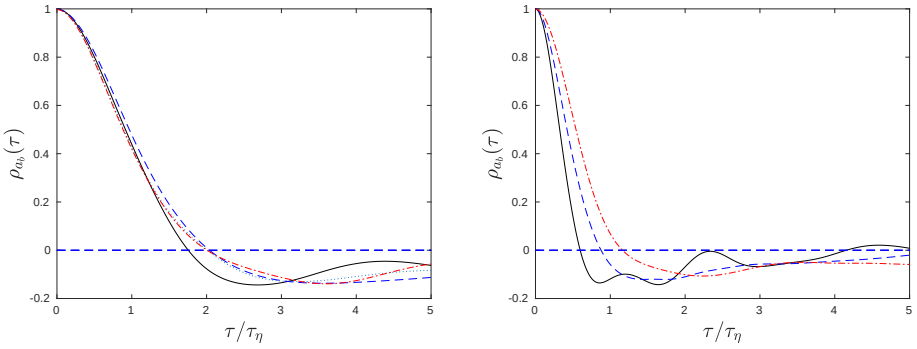

Figure 6.11: Lagrangian auto-correlation of acceleration $\frac{\langle a_{bx}(t)a_{bx}(t+\tau)}{\langle a_{bx}^2 \rangle}\rangle$ for $St = 0.02$ left figure and $St = 1$ right figure. For both figure, (-) is obtained with drag law for Stokes regime (6.3), (- $\cdot$) is obtained with no-slip surface bubble law (6.4), (- -) obtained with slip surface bubble law(6.5).

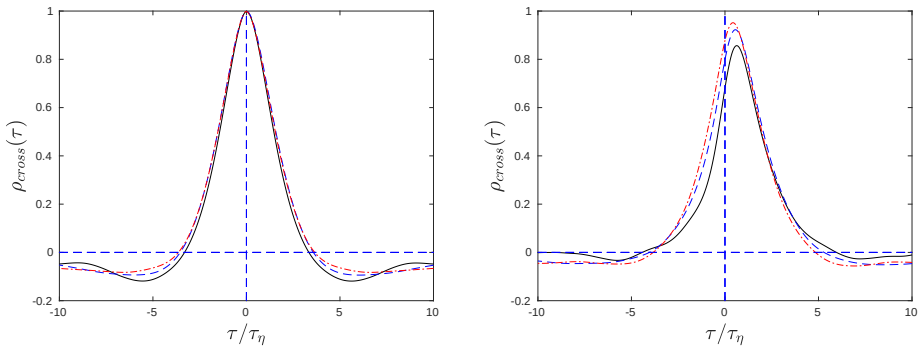

Figure 6.12: The Lagrangian cross correlation between inertia force and drag force $-\frac{\langle F_{Dx}(t+\tau)\cdot F_{Ix}(t)\rangle}{|F_D||F_I|}$ for $St = 0.02$ left figure and $St = 1$ right figure. For both figures (-) is obtained with drag law for the Stokes regime (6.3), (-·) is obtained with no-slip surface bubble law (6.4), (- -) obtained with slip surface bubble law(6.5).

On the other hand, we observe in figure 6.6 that the relative velocity from the three different drag laws collapse fairly well when plotted against St^*. This means that the relative velocity in the case of the non-linear drag laws can be estimated also from the formula (6.13) if one substitute St by St^*. We can therefore estimate the average bubble Reynolds number from the following relation:

$$\langle Re_b\rangle = (St^*\tau_\eta)\frac{d_b}{\nu}a_\eta\sqrt{c_0\frac{(1-\beta)^2}{1-St_{0,*}^2}\left(\frac{\tan^{-1}(c_1St^*)}{c_1St^*}-\frac{\tan^{-1}(c_1Re_0^{1/2})}{c_1Re_0^{1/2}}\right)} \tag{6.14}$$

Since St^* depend on the average value of the Reynolds number, $St^* = St/\mathcal{F}(\langle Re_b\rangle)$, the relation (6.14) cannot provide an explicit estimation of $\langle Re_b\rangle$. However it can easily be solved iteratively by taking as initial guess $St^* = St$. We compare the results of $\langle Re_b\rangle$ estimated with (6.14) and the results computed with DNS in figure 6.14. The results show a fairly good estimation.

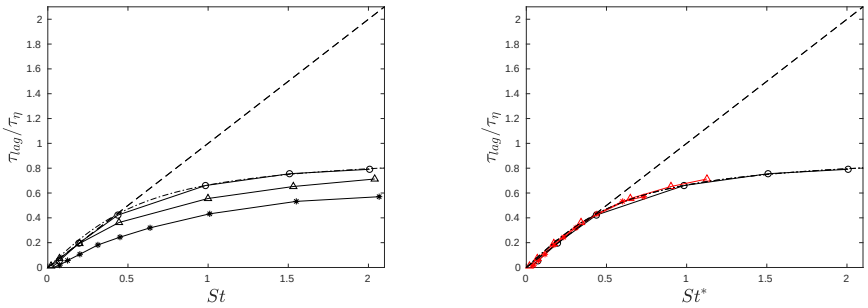

Figure 6.13: The time lag τ_{lag} defined as $\rho_{cross}(\tau_{lag}) = Max(\rho_{cross})$ versus (left) St (Right) St^*. For both figures ($\circ$) is obtained with drag law for the Stokes regime (6.3), ($*$) is obtained with no-slip surface bubble law (6.4), ($\triangle$)obtained with a slip surface bubble law (6.5).

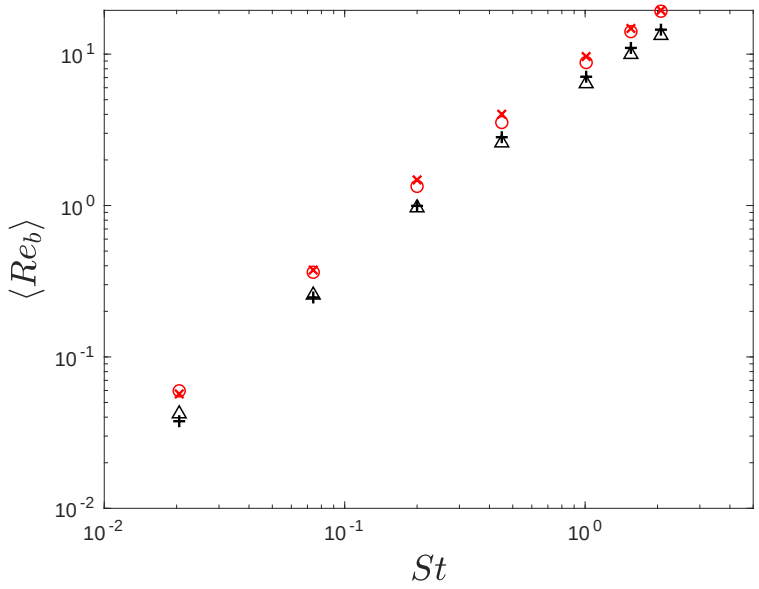

Figure 6.14: Comparison of the $\langle Re_b \rangle$ computed from DNS and estimated from (6.14). For a slip surface bubble with drag law (6.5), ($\circ$) is the value obtained from the DNS, (x) is the value estimated with (6.14). For a no-slip surface bubble with drag law (6.4), ($\triangle$) is the value obtained from the DNS, (+) is the value estimated with (6.14).

6.3 Conclusions

In this section we have considered correction to the drag force due to the effect of finite bubble Reynolds number $1 < Re_b < 200$. It has been assumed that the instantaneous drag coefficient can be estimated from empirical relations that depend on the bubble Reynolds number and on the contamination of the interfaces by surfactants. We observe that the deviations of the drag coefficient from the Stokes expression can have a significant impact on the bubble dynamics leading to a reduction of the characteristic relative velocity, an increase of the drag force variance as well as a diminution of the bubble acceleration variance. We have shown that these local Reynolds number effects could be accounted for, to first order, by rescaling the characteristic relaxation time of the bubble. This scaling factor is a function of the average bubble Reynolds number, and results in an effective relaxation time smaller than the original Stokes relaxation time.

In the derivation of these results a critical assumption was made. Indeed the validity of the above-mentioned expressions for the drag coefficient requires that the flow around the bubble is, at least locally, homogenous and stationary, which for a bubble with $St > 1$ is not the case since it also implies $d > \eta$. This important remark call for a refined treatment of the finite size effect of the bubble. Such modeling was recently proposed in [24] by introducing a random relaxation time that accounts for the turbulent structure of the flow around a solid particles. It is a priori not straightforward to extend this approach to large bubbles, since they are likely to deforms which would require to also account for the non-spherical bubble, its rotation as well as the induced lift force.

Nevertheless there is a particularly important case in which the bubbles can be considered smaller than the Kolmogorov scale but present a Reynolds number larger than one. When the bubbles are subject to the gravity force their slip velocity can become large without necessarily implying that their Stokes number becomes large. In the next section, we will study the rising of bubbles in turbulent flows capitalizing on the results presented here to account for finite bubble Reynolds number effects.

Chapter 7

Gravity effect on the bubble motion in turbulence

In this section, we discuss the buoyancy effect on a small bubble in isotropic homogeneous turbulent flow. The investigation will focus on the rising velocity and the Lagrangian statistics of acceleration under the effect of gravity, drag and fluid inertia force. The bubble rises in the opposite direction of gravity due to the buoyancy force. The rising terminal velocity in quiescent flow is then defined as

$$V_{term} = (\beta - 1)\boldsymbol{g}\tau_b \tag{7.1}$$

τ_b is the relaxation time scale of a bubble, in the Stokes regime it is defined as $\tau_b = d_b^2/24\nu$. The terminal velocity corresponds to the stationary velocity reach by a bubble (particle) rising in quiescent fluid. Note that for large bubble Reynolds numbers, due to the deformation of the bubble, the rising velocity can present path oscillation resulting in non-steady vertical velocity even in the absence of any other imposed fluctuations in the liquid [58]. A bubble rising in a turbulent flow will obviously present fluctuations in its rising velocity, due to others hydrodynamic forces, such as fluid inertia force and drag force.

It has been observed that in turbulent flows, bubbles experience a reduction of their average rising speed [11, 12, 59, 13, 60, 61]. Likewise, numerical [62, 6, 38, 63] and experimental studies [64] have shown that the settling velocity of heavy particles have been observed to be enhanced. However, recent experimental studies have also provided evidence that turbulence can reduce the settling velocity of heavy particles with large St [65]. In the experimental study of oil droplet rising in water, with $\Phi_\rho < 1$ [66], the mean rising velocity of the droplets was found to be larger or smaller than the quiescent rise velocity, depending upon the turbulence intensity, droplet

size and upon the droplet Stokes number.

Focusing back on the small bubbles, it was summarized by [67] that the reduction of their rising velocity can be attributed to the following reasons.

- The bubbles under the lift force effect tend to go to the downward stream, which causes an oversampling of negative vertical velocity (opposite direction to the buoyancy force).
- The regions where the bubbles tend to accumulate are prone to yield in a downward direction lift force component.
- Bubbles can be trapped in the strong vortex for a significant time.

We propose to study as well the influence of high Reynolds turbulent flow on the rising velocity. In this chapter we ignore the lift force [1] and consider only the buoyancy force, drag force and fluid inertia forces in the equation of motion Eq. (7.2). Specifically, we will discuss the effects of the inertia forces on the rising velocity. It is interesting because even without lift force, the average rising velocity is also observed to be smaller than the Stokes terminal velocity [60, 11].

We performed DNS of the fluid field with the same configuration as already reported in table 6.1 and the force balance equation for the bubbles reads:

$$\frac{d\boldsymbol{u}_b}{dt} = \frac{\boldsymbol{u}_f - \boldsymbol{u}_b}{\tau_b}\mathcal{F}(Re_b) + \beta\frac{D\boldsymbol{u}_f}{Dt} + (1-\beta)\boldsymbol{g} \tag{7.2}$$

We are only interested in the case of light bubbles for which $\beta = 3$. As discussed in the previous chapter, the function $\mathcal{F}(Re_b)$ stands for the finite Re_b effects in the drag force of the bubbles. Specifically, we consider the case of a bubble experiencing free slip conditions at its interface, for which the expression of $\mathcal{F}$ is given in Eq.(6.5). We denote this simulation as simulation I.

Remark that the effects of buoyancy generate a significant slip velocity (or relative velocity), and in consequence the bubble Reynolds number could mostly be larger than unity and the drag law in Stokes regime (6.3) do not hold. Nevertheless, for comparison, the DNS has also been performed with drag law for the Stokes regime, $\mathcal{F} = 1$, along with $Re_\lambda = 100$, denoted hereafter simulation II. Finally, we analyze the effect of the flow Reynolds number by performing a DNS for a larger $Re_\lambda = 200$, still with the drag law in the Stokes regime (named simulation III). The details of the carrier flows can be found in TABLE 1 of Chapter 5.

[1] Note, however, that the next chapter is dedicated to the effect of the lift force.

The gravity will be characterized using the Froude number $Fr = \frac{a_\eta}{(1-\beta)g}$ that compare the fluid acceleration at the Kolmogorov scale to the buoyancy force per unit subject to gravity. For the simulations with $Re_\lambda = 100$ (i.e. Simulations I and II) the Froude number is set to $Fr = 0.185$ while for the simulation III with $Re_\lambda = 200$ the Froude number is larger: $Fr = 0.716$ and therefore the effect of buoyancy on the bubbles is reduced because of more intense turbulent fluctuations. For each simulation, we will study the effect of the bubble Stokes number $St = \frac{\tau_b}{\tau_\eta}$ and the effect of $St^* = \frac{\tau_b^*}{\tau_\eta}$. The parameters of the simulations are shown in the tables 7.1 for the Simulation I and 7.2 for the simulations II and III.

d_b/η	0.70	1.33	1.72	2.19	2.74	3.29	3.91	4.92	6.10	7.04
St	0.02	0.074	0.12	0.20	0.31	0.45	0.64	1.01	1.55	2.07
St^*	0.02	0.07	0.11	0.17	0.24	0.32	0.41	0.58	0.81	1.01

Table 7.1: Simulation (I) using no-linear drag law for $Re_\lambda = 100$, $Fr = 0.185$

d_b/η	0.69	1.33	2.19	3.29	4.92	6.10	7.05
St	0.02	0.07	0.20	0.45	1.01	1.55	2.07
St^*	0.02	0.07	0.20	0.45	1.01	1.55	2.07

Table 7.2: Simulation (II) using drag law in the Stokes regime for $Re_\lambda = 100$, $Fr = 0.185$, and simulation (III) using drag law in the Stokes regime for $Re_\lambda = 212$, $Fr = 0.716$. Note: $St = St^*$ because using drag law in Stokes regime.

7.1 Average rising speed from DNS

From Eq. (7.2), the average force equation of a bubble reads:

$$0 = \langle \frac{\boldsymbol{u}_f - \boldsymbol{u}_b}{\tau_b} \mathcal{F}(Re_b) \rangle + \beta \langle \frac{D\boldsymbol{u}_f}{Dt} \rangle + (1-\beta)\boldsymbol{g} \tag{7.3}$$

In absence of flow, aside from the perturbation caused by the rising bubble itself, one has $\boldsymbol{u}_f = 0$ and $\frac{D\boldsymbol{u}_f}{Dt} = 0$ which allows the mean vertical bubble velocity $\langle u_{bz} \rangle$ to recover the terminal velocity given in Eq. (7.1). From this equation it is apparent that the alteration of the average rising speed can be caused by non-zero average fluid velocity and acceleration at the bubble position. Although the flow remains homogeneous and isotropic on average, the bubbles can preferentially sample certain regions of the flow which can result in non-zero average for these quantities. Another cause of alteration can be found in the Reynolds number dependence on the drag law. Of course different drag laws results in different relative velocities (keeping unchanged

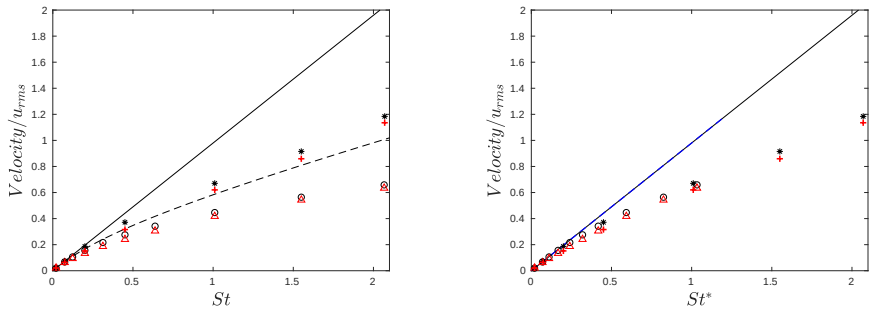

Figure 7.1: (–) terminal velocity defined as $V_{term} = (\beta - 1)\boldsymbol{g}\tau_b$ with $\tau_b = d_b^2/(24\nu)$ (- -) $V^*_{term} = (\beta - 1)\boldsymbol{g}\tau^*_b$ with τ^*_b estimated as in the previous chapter with Eq. (6.5); $(*)$ is the averaging relative velocity in the z-direction defined as $\langle W_{rel}\rangle = \langle u_{bz} - u_{fz}\rangle$ from simulation II considering the drag force in the Stokes regime, $(+)$ is $\langle u_{bz}\rangle$ from simulation II, $(\circ)$ is $\langle W_{rel}\rangle$ of the nonlinear drag law from simulation I and $(\triangle)$ is $\langle u_{bz}\rangle$ from simulation I. (Left) Evolution with $St = \tau_b/\tau_\eta$, (right) the evolution with $St^* = \tau^*_b/\tau_\eta$. Note that in the evolution with St^*, V_{term} (-) and V^*_{term} (- -) collapse on the same curve. All of the velocity values in this figure are normalized with the RMS of turbulent velocity fluctuations u_{rms}.

every other parameters). As a follow-up of the previous chapter, we compare in this section the average rising velocity of bubbles subject to the drag law in Stokes regime and to non-linear drag law for clean bubbles.

Neglecting the fluctuation of the bubble Reynolds number around its average value, we can write the average drag force as:

$$\langle \frac{\boldsymbol{u}_f - \boldsymbol{u}_b}{\tau_b}\mathcal{F}(Re_b)\rangle \approx \frac{\langle \boldsymbol{u}_f\rangle - \langle \boldsymbol{u}_b\rangle}{\tau_b}\mathcal{F}(\langle Re_b\rangle) = \frac{\langle \boldsymbol{u}_f\rangle - \langle \boldsymbol{u}_b\rangle}{\tau^*_b} \tag{7.4}$$

Whereas discussed in Chapter 6, we define an effective relaxation time for the bubbles based on the average value of Re_b: $\tau^*_b = \tau_b/\mathcal{F}(\langle Re_b\rangle)$, with $\mathcal{F} > 1$. From the definition of the terminal velocity $V_{term} = (1-\beta)\boldsymbol{g}\tau_b$, it is clear that a rescaling of the relaxation time modifies the terminal velocity. This means that in still liquid, large bubbles will have smaller rising velocity, $V^*_{term} = (1-\beta)\boldsymbol{g}\tau^*_b$ compared to the estimation with drag force in the Stokes regime. In turbulent flows, we observe a similar behavior as well. In figure 7.1, we report the average vertical velocity for different bubble diameters, and we compare the case of bubbles subject to non-linear drag (Simulation I) and drag in the Stokes regime (Simulation II). It is observed that, for a given bubble diameter (or Stokes number), the rising velocity is smaller if one accounts for the finite Reynolds number effect in the computation of the drag. It is further observed that bubbles systematically present a rising

velocity smaller than their terminal velocity. If we use the method proposed in Chapter 6 to estimate the effective $St^* = \tau_b^*/\tau_\eta$ with the relation (6.5), we can see that the average rising velocity and the average relative vertical velocity have approximately the same value.

In order to estimate the effect due to the oversampling of fluid region with negative vertical velocity by the bubbles, we also report in this figure the evolution of the average relative vertical velocity $\langle W_{rel} \rangle = \langle u_{bz} - u_{fz} \rangle$ for both drag laws. It is indeed observed that $\langle W_{rel} \rangle$ is slightly larger than the bubbles average rising velocity. This means that even without lift force the bubble still over sampling regions where the fluid velocity is negative. However $\langle W_{rel} \rangle$ remains significantly smaller than the terminal velocity when St increases. As deduced from (7.3) and (7.4), this means that the average contribution of the fluid inertia force is comparable, in magnitude, to the buoyancy force itself. We present in figure 7.2 the average vertical component of the fluid inertia force normalized by the buoyancy force, for the three simulations. For vanishingly small Stokes number bubbles behave as tracers, even in the presence of the buoyancy force, and therefore the average inertia force is null. However when the Stokes number is increased, it is observed that the mean fluid inertia force becomes negative, and presents important values relatively to the buoyancy force: for $St \approx 1$ it is about $1/3$ of the buoyancy in absolute value. From (7.3) and (7.4), we can write an approximate relation between the average drag force and fluid inertia force:

$$\frac{\langle W_{rel} \rangle}{V_{term}} = 1 + \frac{\beta \langle a_{fz} \rangle}{(1-\beta)\boldsymbol{g}}. \tag{7.5}$$

where a_{fz} is the z-component total acceleration of the fluid at the bubble position. It observed in figure 7.3 that $\langle W_{rel} \rangle / V_{term}^*$ seems to decrease with St^* as a function of exponential and to be independent of the drag law or the flow Reynolds number and Froude value. The proposed data fitting

$$\frac{\langle W_{rel} \rangle}{V_{term}^*} = \frac{\exp(-1.2St^*) + 1}{2} \tag{7.6}$$

is purely empirical of such evolution and it should be interesting for further study to find an explanation.

In figure 7.4, we compare our results concerning the relative velocity with the results from the DNS of [11]. In their simulation, they have used the same equation Eq. (7.2) to track very light spherical particles motion. More specifically, [11] uses the Stokes drag force ($\mathcal{F} = 1$) and $\tau_b = d_b^2/36\nu$ in the case of contaminated (no-slip interface bubble), fluid inertia force with $\beta = 3$ and the buoyancy force $(1-\beta)\boldsymbol{g}$, with terminal velocity $(1-\beta)\boldsymbol{g}\tau_b = u_\eta$ ($Fr = 1$) and $Re_\lambda = 62$. We can see that our results quantitatively agree with those of [11]. In our simulation, we have surprisingly bubble rising

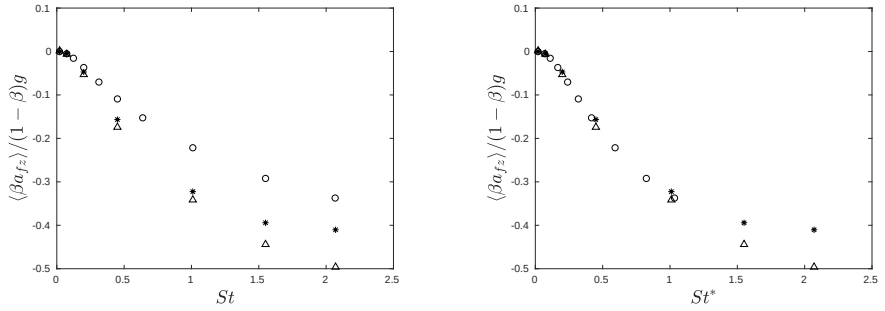

Figure 7.2: Average vertical component of the fluid inertia force normalized by the buoyancy force plotted versus the Stokes number St (left) and the effective Stokes number St^* (right) for 3 simulations. ($\triangle$) $Re_\lambda = 200$ drag force in the Stokes regime (simulation III); ($*$) $Re_\lambda = 100$ drag force in the Stokes regime (simulation II) ; and ($\circ$) $Re_\lambda = 100$ bubble drag law (6.5) (simulation I).

velocity larger than the terminal velocity for the smallest $St = 0.02$. The explanation is that, for $St = 0.02$, the value of the fluid vertical velocity at the bubble position is positive on average $\langle u_{fz} \rangle > 0$. A bubble, with $St = 0.02$, responds instantaneously to the ambient flow velocity. We should remark that, the average value of the fluid vertical velocity at the bubble position $\langle u_{fz} \rangle$ for $St = 0.02$ is about 0.1% of the large eddy velocity which could also be caused by a statistical error.

7.2 Model for the preferential sampling of negative regions

In order to explain why the average fluid velocity and fluid inertia sampled by the bubble are negative, a primitive analysis of the bubble motion in a horizontal vortex is proposed [68, 69]. Consider a bubble in a steady vortex in the xz-plan with a constant angular velocity ω is anticlockwise, see figure 7.5. In cylindrical coordinate $(\boldsymbol{e}_r, \boldsymbol{e}_\theta)$, for a given radial distance r the velocity is $\boldsymbol{u}_f = r\omega \boldsymbol{e}_\theta$ and the fluid acceleration is $\boldsymbol{a}_f = -r\omega^2 \boldsymbol{e}_r$. After releasing a bubble in such a vortex, it will reach an equilibrium position noted (r_e, θ_e) so $\boldsymbol{u}_b = 0$ and $\boldsymbol{a}_b = 0$. At such position the drag force is $\boldsymbol{F}_D = (0, \frac{r_e \omega}{\tau_b})$, the fluid inertia force is $\boldsymbol{F}_I = (-\beta r_e \omega^2, 0)$ and the buoyancy force components are: $\boldsymbol{F}_g = (-(1-\beta) g \sin(\theta_e), -(1-\beta) g \cos(\theta_e))$, and they are in balance: $\boldsymbol{F}_D + \boldsymbol{F}_I + \boldsymbol{F}_g$. This gives the two following equations:

$$0 = 0 - \beta r_e \omega^2 - (1-\beta) g \sin(\theta_e) \tag{7.7}$$

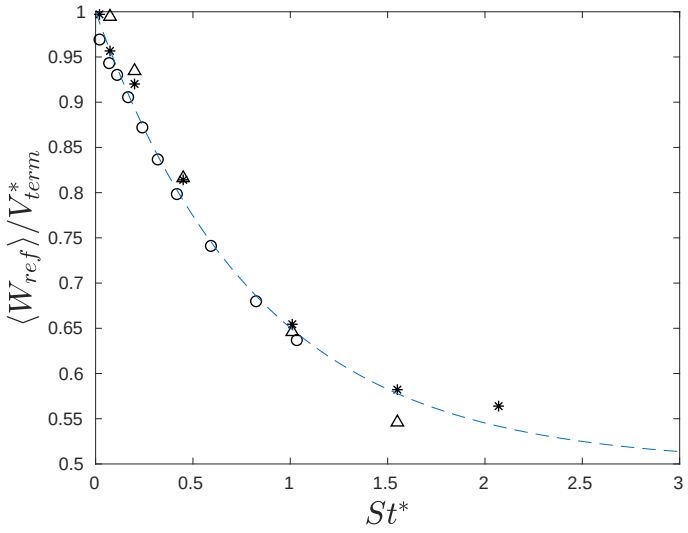

Figure 7.3: The reduction rate $\langle W_{rel} \rangle / V^*_{term}$ versus St^*, ($\circ$) for simulation I ($Re_\lambda = 100$), ($*$) for simulation II ($Re_\lambda = 100$), ($\triangle$) for simulation III ($Re_\lambda = 200$). (- -) is an exponential fitting of form (7.6).

$$0 = \frac{r_e \omega}{\tau_b} + 0 - (1-\beta) g \cos(\theta_e) \tag{7.8}$$

which we can rewrite as

$$\sin \theta_e = -\frac{\beta r_e \omega^2}{(1-\beta) g} \tag{7.9}$$

$$\cos \theta_e = \frac{r_e \omega}{(1-\beta) g \tau_b} \tag{7.10}$$

g here is the norm of gravity $|\boldsymbol{g}|$. From Eq. (7.9) and Eq. (7.10), $\cos \theta_e$ is always negative whereas $\sin \theta_e$ is always positive. This means the equilibrium position is to be found in the locations where vertical component of the fluid acceleration is negative and a negative vertical fluid velocity (top left quadrant of figure 7.5. This model explains first that a bubble can be trapped in a vortex and that once it is trapped it is likely to experience both negative vertical component of the drag force and of the fluid inertia force.

We now discuss the relevance of this simple model to analyze the motion of the bubble in turbulent flows. First we remark that according to the model an equilibrium position always exists because both the drag force and the inertia force increases linearly with the radial distance and the radial extension of the vortex can be arbitrary long in the model. Indeed solving equations (7.9) and (7.10) for r_e and θ_e one obtains:

$$\tan \theta_e = -\beta \omega \tau_b \tag{7.11}$$

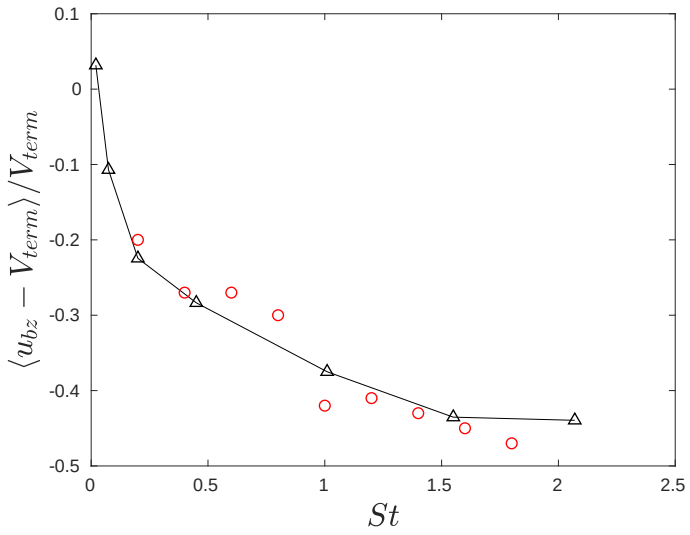

Figure 7.4: The difference of bubble average rising velocity in turbulence between the rising velocity in quiescent flow (terminal velocity) $\frac{\langle u_{bz} - V_{term} \rangle}{V_{term}}$, ($\triangle$) is in our simulation with drag law for clean bubbles in the Stokes regime and $Re_\lambda = 100$ ($\circ$) is the simulation of [11] with the same method with Stokes drag for contaminated bubble and $Re_\lambda = 62$.

$$r_e = \frac{(\beta - 1)g}{\omega(1/\tau_b^2 + \beta^2\omega^2)^{1/2}} \tag{7.12}$$

The first equation confirms that the tangent of the equilibrium position angle is negative and thus the bubble position is in the top left quadrant. While the second equation shows that the radial equilibrium position increases linearly with gravity but reduces with rotation rate. One sees here a possible limitation of the model: a vortex with given vorticity value has to be large enough to include the radial equilibrium position of the bubble. According to the Kolmogorov 41 theory the size ℓ, of a structure and its vorticity ω_ℓ are connected, if one agree to identify the typical vorticity of the structure as its inverse time scale: $\omega_\ell = (\langle\varepsilon\rangle/\ell^2)^{1/3}$. Therefore a condition for the model is to require that:

$$r_e(\ell)/\ell \ll 1 \tag{7.13}$$

where $r_e(\ell)$ is the radial distance between the bubble equilibrium position and the center of a horizontal vortex of characteristic size ℓ and vorticity ω_ℓ. Substituting $\omega_\ell = (\langle\varepsilon\rangle/\ell^2)^{1/3}$ in place of ω in (7.12) one can express $r_e(\ell)/\ell$ as:

$$\frac{r_e(\ell)}{\ell} = \left(\frac{\ell}{\eta}\right)^{-1/3} \frac{St}{Fr} \left(1 + \beta^2 St^2 \left(\frac{\ell}{\eta}\right)^{-4/3}\right)^{-1/2} \tag{7.14}$$

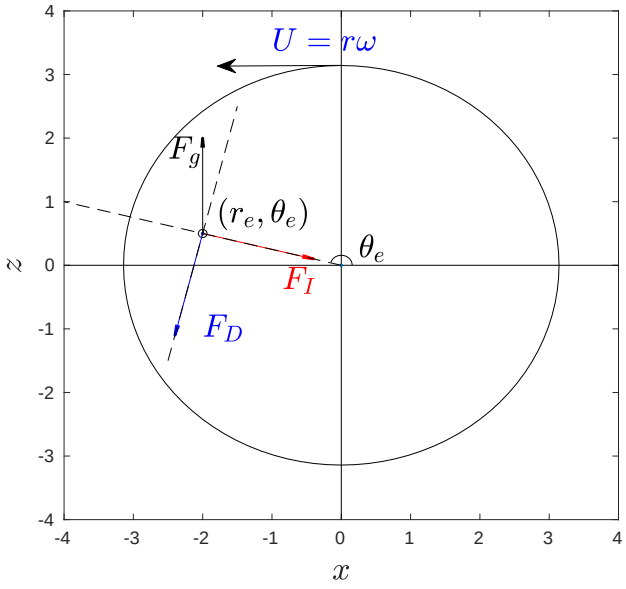

Figure 7.5: Sketch to illustrate bubble equilibrium in a steady rotation with anticlockwise angular speed of ω, accounting for drag F_D, fluid inertia F_I and buoyancy F_g forces acting on the bubble.

with η being the Kolmogorov dissipative scale of the flow. From this formula we see that for small Fr values (strong gravity) $r_e(\ell)/\ell$ can present values larger than 1 over a range of scale ℓ. The graph of $\frac{r_e(\ell)}{\ell} \times Fr$ against ℓ/η is plotted in figure 7.6 for various values of St, from $St = 0.01$ to $St = 10$. The model can be relevant if $\frac{r_e(\ell)}{\ell} \times Fr \ll Fr$. If this condition is not satisfied, the bubble may have difficulty to find an equilibrium position in the structure of size ℓ. From this figure we can conclude that for $Fr = 0.185$ the model can be considered as relevant only for $St < 1$, whereas for larger St the bubble will escape from the vortex.

Another possible limitation of the model lies in its stationary character. Indeed once a bubble enters in a vortex, it takes a finite time, probably of the order of τ_b, to reach its equilibrium position (granted the vortex is large enough). Therefore the characteristic lifetime of the structure needs to be larger than the bubble relaxation time. The structure lifetime can be estimated as ω_ℓ^{-1}, therefore, only the structure of size ℓ such that

$$\ell/\eta \gg St^{3/2} \tag{7.15}$$

can live long enough to allow the bubble to find an equilibrium position. As we only consider here St of order unity at most, this condition is a

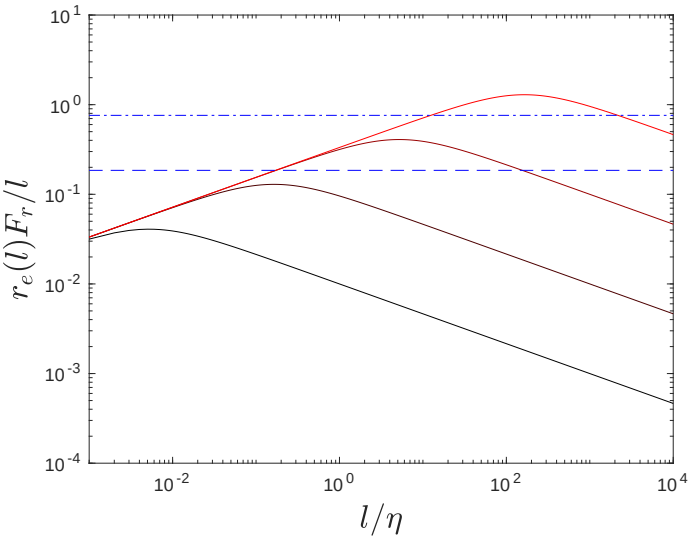

Figure 7.6: Equilibrium radials position of a bubble $\frac{r_e(\ell)}{\ell} \times Fr$ against ℓ/η for $St = 0.01, 0.1, 1$ and 10 form black to red color. Vortex model is relevant for $\frac{r_e(\ell)}{\ell} \times Fr < Fr$. The two horizontal lines correspond to (- -) $Fr = 0.185$ and (- ·) $Fr = 0.76$ (values of our DNS).

priori satisfied as it appears as restrictive than the inertial range condition ($\ell/\eta \gg 1$).

Numerical studies have shown that small bubbles are indeed trapped in a vortex [11, 67]. The trapping time is of the order of the structure lifetime, which gives an intermittent picture for the bubble vertical motion, the bubble experiences successive phases of freely rising motion and phases of capture by a vortex. Moreover the duration of the capture might be considered as random as the bubbles can reside in large vortex with large time scale or in smaller ones (with smaller lifetime). This model appears consistent with the observation of DNS that both the relative velocity and the fluid acceleration at the bubble position are negative in average (see figures 7.1 and 7.2).

7.3 Acceleration statistics under buoyancy force

The buoyancy force impacts the bubble acceleration statistic, even for very small bubble $St < 1$. It has been observed [70] that the gravity can enhance both vertical and horizontal acceleration variances. In their study, [70] focus on very small bubbles with St of the order of 10^{-2}. Our numerical simulations are consistent with this result, and extend the range of Stokes number studied as St varies from 0.02 to 2.07. Figure 7.7 presents the variance of both the horizontal and vertical acceleration components for $Fr = 0.185$ along with the bubble acceleration variance in absence of gravity ($Fr \to \infty$) in the case of drag force in the Stokes regime. We confirm the observations that acceleration variance in any direction is increased by gravity. We can also remark that the variance of the acceleration in the horizontal direction is even slightly larger than in the vertical direction. The observation can be associated to the alternation of capture and rising which could increase the fluctuation of the acceleration.

However the acceleration flatness, is reduced by the gravity as seen in figure 7.8 which compares the normalized 4th order moment of the acceleration for $Fr = 0.185$ and $Fr = \infty$ in the case of Stokes drag for $Re_\lambda = 100$ and 200. It is further observed that the horizontal component is more reduced than the vertical one. It is also seen that the flatness of the fluid acceleration at the bubble position is also smaller than what has been observed in the simulation without gravity. The reduction also depends on the relative importance of the gravity to the turbulent intensity, herein the $Fr = \frac{a_\eta}{(1-\beta)g}$ with characteristic acceleration scale of the turbulence a_η.

The *pdf*s of the acceleration, with and without gravity, are presented in figure 7.9. The reduced flatness is not significantly important to change

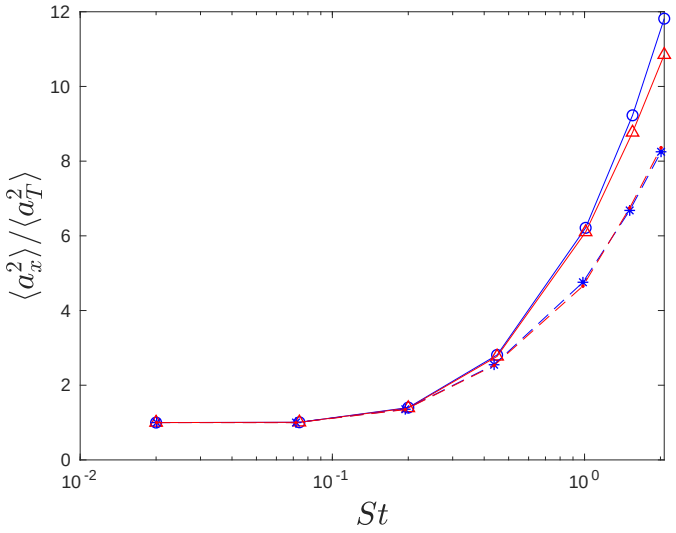

Figure 7.7: Acceleration variance versus the Stokes number $St = \tau_b/\tau_\eta$, ($\circ-$) horizontal component of acceleration with gravity, ($\triangle-$) vertical component of acceleration with gravity, (- $*$ -) horizontal component of acceleration without gravity, (- $\cdot$ -) vertical component of acceleration without gravity. For all the curve, the drag law is given in the Stokes regime as in simulation II with $Re_\lambda = 100$.

the form of the distribution function. The *pdf*s of acceleration preserve the log-normal distribution in both x and z directions at least for small enough fluctuations.

The acceleration Lagrangian auto-correlation is also affected by the buoyancy force. Figure 7.10 shows that the acceleration remains correlated over a slightly longer period when the bubbles are subject to gravity, and the difference appears to be larger for large St. However, it is observed that the vertical and the horizontal acceleration components do not show a significant difference.

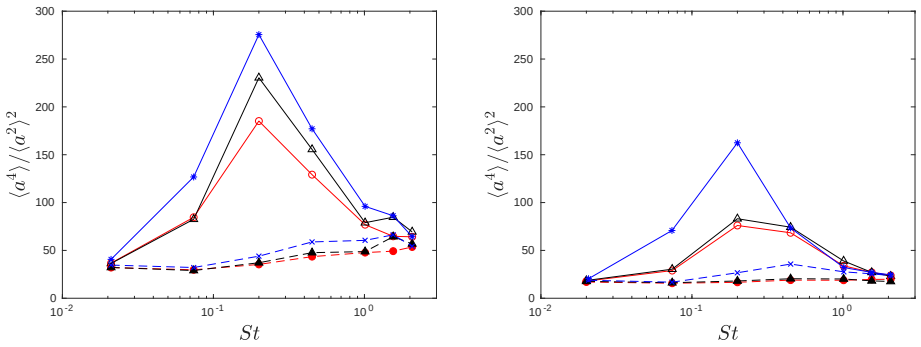

Figure 7.8: The bubble acceleration flatness versus the Stokes number $St = \tau_b/\tau_\eta$, with (left) $Fr = a_\eta/(1-\beta)g = 0.72$, (right)$Fr = a_\eta/(1-\beta)g = 0.19$, ($\circ-$) horizontal component of acceleration with gravity, ($\triangle-$) vertical component of acceleration with gravity, ($*-$) vertical component of acceleration without gravity. The evolution of the flatness of the fluid acceleration at the bubble position versus St, ($\bullet--$) horizontal component of acceleration with gravity, ($\blacktriangle--$) vertical component of acceleration with gravity, ($\times$--) vertical component of acceleration without gravity.

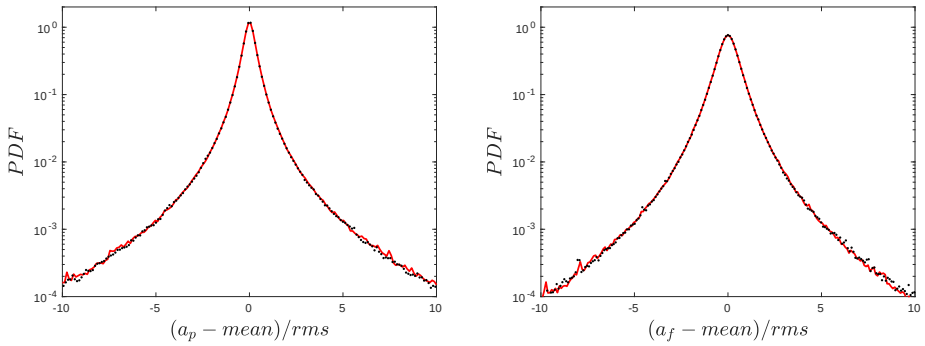

Figure 7.9: The normalized PDFs of the bubble ($St = 0.45$) bubble acceleration (left) and the fluid acceleration at the bubble position(right), (red color) is horizontal component (black) is the vertical component.

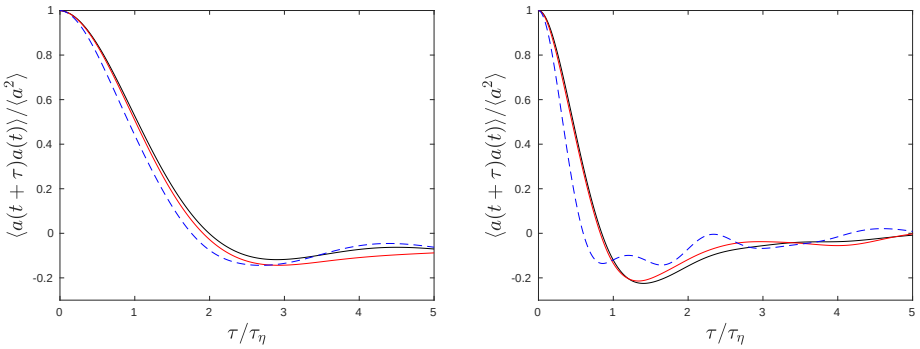

Figure 7.10: The Lagrangian autocorrelation functions under gravity effects. The continuous lines are the autocorrelation function with gravity and the dash line is that without gravity, black is the x-component and red is the z-component. (left) $St = 0.02$, (right) $St = 1$.

7.4 Conclusions

In this chapter, the gravity effect on the bubble motion in turbulence has been considered for bubbles with non-vanishing Re_b. The finite Reynolds number effect of the drag force (nonlinear drag) reduces the average rising velocity by increasing the mean drag force. Following the conclusions of the previous chapter, we can use the effective relaxation time to estimate the effective terminal velocity taking account for the finite Reynolds number effects.

We found that even without lift force the bubble still slightly oversampling downstream flows. The oversampling effect increases with St and saturate around $St \simeq 0.5$. But the main reason for the reduction of the rising speed is the negative value of the average vertical component of the fluid inertia (i.e. fluid acceleration at the bubble position).

Furthermore, we considered the gravity effect to the bubble acceleration statistics. The gravity increases the bubble acceleration variance and decreases its flatness for small $Fr < 1$. The acceleration is also observed to remain correlated over a long period compared to the case without gravity.

Chapter 8

Lift force effect on the bubble motion in turbulence

In early simulation studies with point-wise particle method to simulate the bubble motion in turbulence, the lift force is sometimes absent in the equation of motion, such as in [11, 71] as well as in the study presented in previous chapters. The stochastic model we proposed in Chapter 5 has neglected the lift force term. In order to justify this simplification the bubble must be in the Stokes regime, which imply that $Re_b \ll 1$. However, when Re_b becomes non-negligible the lift force might modify the acceleration statistics. The objective of this chapter is to study the lift force effect on the bubble motion, in particular, the acceleration statistics.

Numerical simulations of bubble-laden homogeneous and isotropic turbulent flow accounting for the lift force have shown that the role of the lift force is important for the study of the bubble dynamic and specifically for their rising velocity, because the slip velocity is large. According to [67, 13, 60], lift force results in a strong enhancement of the preferential accumulation of bubbles in the downward flow side of the vortex. This results in a considerable reduction of the bubble rising velocity and an alteration of large-scale motion and a modification of the spatial distribution of bubble clusters in turbulence [71]. But the previous studies are mostly concerned with the interplay between lift and gravity effects. We proposed in this chapter to first investigate only the lift force effects on the acceleration statistics. We performed DNS with only drag, fluid inertia and lift force in the equation of motion. Then in the following section, we will add the buoyancy force, to see how the lift force conjointly with the gravity affects the bubble motion.

The lift force is computed with

$$\boldsymbol{F}_L = (\rho_b/\rho_f + C_M)^{-1} C_L(\boldsymbol{u}_f - \boldsymbol{u}_b) \times \boldsymbol{\Omega}_f \tag{8.1}$$

with the lift force coefficient $C_L = C_L(Re_b, Sr)$ given by eq. (3.18) is a function of (Re_b, Sr) characterizing the relative velocity and the local shear rate, as presented in Chapter 3 [46, 44]. Note that formally F_L is here not a force but a force per unit of displaced mass and for a spherical bubble $(\rho_b/\rho_f + C_M)^{-1} = 2$. In the following we will assume that the bubbles are spherical and have free slip condition on their interface. Since the range of Re_b in our studies do not satisfy the Stokes regime, the drag force in this chapter will be given by the non-linear drag force for clean bubble Eq. (3.8). The effective relaxation time, used for post-treatment, is computed a posteriori as

$$\tau_b^* = \tau_b/\mathcal{F}(\langle Re_b \rangle) \tag{8.2}$$

with $\tau_b = \frac{d_b^2}{24\nu}$, with $\mathcal{F}$ of eq. (6.5) and $\langle Re_b \rangle = \frac{d_b \langle |\boldsymbol{u}_f - \boldsymbol{u}_b| \rangle}{\nu}$ where $\langle |\boldsymbol{u}_f - \boldsymbol{u}_b| \rangle$ is obtained from the DNS, and the effective Stokes number $St^* = \tau_b^*/\tau_\eta$.

8.1 The influence of lift force on bubble acceleration statistics

In this section, we focus on the lift force effect on the bubble acceleration statistics. The objective is to see how much does the lift force impacts the small bubble acceleration statistics with the absence of gravity. Because of the statistical isotropy of the bubble motion, all the acceleration and velocity statistics have zero mean value. The equation of motion for the bubbles per unit of displaced mass is:

$$\boldsymbol{a}_b = \frac{d\boldsymbol{u}_b}{dt} = \frac{\boldsymbol{u}_f - \boldsymbol{u}_b}{\tau_b}\mathcal{F}(Re_b) + 3\frac{D\boldsymbol{u}_f}{Dt} + 2C_L(\boldsymbol{u}_f - \boldsymbol{u}_b) \times \boldsymbol{\Omega}_f \tag{8.3}$$

where the forces per unit displaced mass on the right-hand side are from left to right the drag $\boldsymbol{F_D}$, the inertia $\boldsymbol{F_I}$ and the lift $\boldsymbol{F_L}$. The characteristics of the carrier phase turbulence are identical to those of the previous chapter with $Re_\lambda \simeq 100$. The simulation parameters are reported in table 6.1 for the fluid field and table 7.1 for the bubble size and Stokes number. For reference, simulations are also performed by setting $C_L = 0$ in Eq. (8.3) which will be referred in this chapter as DNS without lift force.

We start by presenting in figure 8.1, the bubble acceleration variance normalized by a_η^2 from the DNS with/without lift force. The first remark is that the lift force does not have a significant impact on the bubble acceleration

variance, at least for Stokes numbers below 2. The bubble acceleration variance $\langle a_b^2 \rangle$ increases with St^* as previously observed without lift force (see figure 6.9). The acceleration variance is almost the same for vanishingly small Stokes number ($St^* = 0.02$), for which a bubble can be essentially considered as a fluid tracer. With the St^* increase, the acceleration variance increases slightly slower compared to the case without lift force. The maximal difference in acceleration variance is observed for $St^* = 0.5$ and for larger St^* the difference becomes progressively smaller.

In figure 8.2, we present the bubble acceleration *pdf*s obtained from the DNS with and without lift force. It is observed that in both cases the bubble acceleration *pdf*s are very similar and present a non-Gaussian behavior with stretched tails indicating the occurrence of very intense acceleration events. For Stokes number of order one ($St^* \simeq 0.65, 0.9, 1.13$), the bubble acceleration *pdf*s appears nevertheless more stretched with lift force than without lift force.

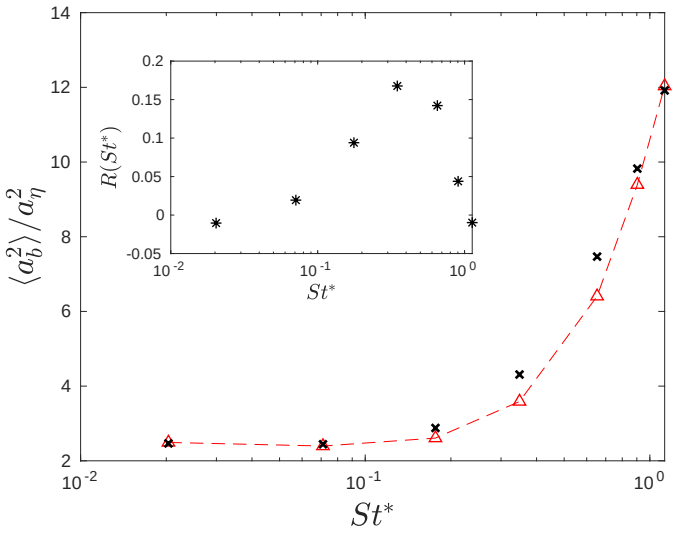

Figure 8.1: Bubble acceleration variance ($\triangle$) simulation with the lift force $\langle a_l^2 \rangle$, ($\times$) for bubble acceleration variance of the simulation without the lift force $\langle a_{nl}^2 \rangle$. Insert: Acceleration variance $R(St^*) = \frac{\langle a_{nl}^2 \rangle - \langle a_l^2 \rangle}{\langle a_{nl}^2 \rangle}$ without and with lift force normalized with the former acceleration variance.

We also compare, in figure 8.3, the Lagrangian acceleration autocorrelation along the bubble trajectory $\rho_{a_b} = \frac{\langle a_b(t) a_b(t+\tau) \rangle}{\langle a_b^2 \rangle}$ with and without the lift force for various Stokes numbers. It is observed that, the Lagrangian autocorrelation functions present again a very similar evolution. In both cases,

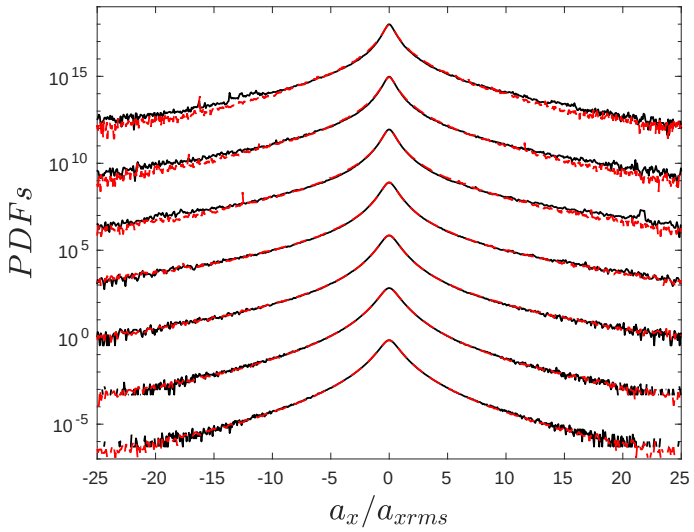

Figure 8.2: (- -) *pdf*s of the bubbles acceleration (without lift force and gravity) normalized by its root-mean-square value, (–) *pdf*s of the bubbles acceleration (with lift force and no gravity) normalized by its root-mean-square value for $St^* = 0.02,\ 0.07,\ 0.18,\ 0.35,\ 0.6,\ 0.90,\ 1.13$ (respectively, shifted upward by two decades from each other for clarity).

when the Stokes number increases, we observe a faster decorrelation of the acceleration. In order to analyze further the dynamic of the bubbles when subject to the lift force, we plot in figure 8.4 the variance of the various forces (per unit of displaced mass): fluid inertia effect $\langle \mathbf{F}_I^2 \rangle$, drag force $\langle \mathbf{F}_D^2 \rangle$ and lift force $\langle \mathbf{F}_L^2 \rangle$ in the two cases: with or without lift force. These variances are normalized by a_η^2. From Eq. (8.3), the variance of the bubble acceleration is related to the variance of the forces with the following expression:

$$\langle \mathbf{a}_b^2 \rangle = \langle \mathbf{F}_I^2 \rangle + \langle \mathbf{F}_D^2 \rangle + \langle \mathbf{F}_L^2 \rangle + 2\langle \mathbf{F}_I . \mathbf{F}_L \rangle + 2\langle \mathbf{F}_I . \mathbf{F}_D \rangle + 2\langle \mathbf{F}_L . \mathbf{F}_D \rangle \qquad (8.4)$$

The last three terms are the correlation between the forces and are plotted in figure 8.4. In this figure, we see that the lift force increases with St^* and becomes, at large St^*, comparable to the fluid inertia force, which remains the dominant force. At $St^* \simeq 1.1$ the variance of the lift force is about 50% of the fluid inertia. We can remark that the fluid inertia force variance is very slightly reduced when accounting for the lift force. This reduction is due to the modification of the preferential concentration caused by the lift force, which is maximum when the bubble relaxation time has the same order as the Kolmogorov scale. Concerning the drag force, it is observed as well as the lift force, it has a very reduced impact on the statistics. We notice a small increase of the drag force when accounting for the lift force. Also to

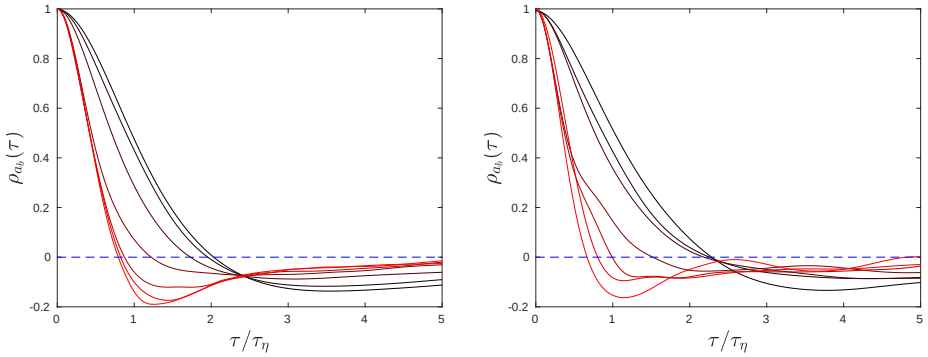

Figure 8.3: The auto-correlation function of bubble acceleration $\rho_{a_b} = \frac{\langle a_b(t)a_b(t+\tau)\rangle}{\langle a_b^2\rangle}$. (Left) DNS without lift force, (Right) DNS with lift force. $St^* = [0.02,\ 0.07,\ 0.18,\ 0.35,\ 0.65,\ 0.90,\ 1.13]$ (from black to red respectively).

be remarked is that the variance of the lift becomes more important than the drag force for $St^* > 0.5$. To summarize, we found that although the lift force variance is quite significant for large St^*, the total bubble acceleration does not change much.

To explain this, we use the decomposition of the bubble acceleration variance given in Eq. (8.4). We can see in figure 8.4, the correlation between drag force and inertia force $2\langle \boldsymbol{F}_I.\boldsymbol{F}_D\rangle$ remains nearly unchanged with or without lift force, and presents the same behavior as detailed in Chapter 5: the drag and inertia force are completely anticorreleted for $St^* = 0$. And this anticorreleation progressively return to 0 as the St^* increases and the characteristic time scale of the drag force increases. We observe a different behavior between the lift force and the inertia force. As St^* increases the lift force increases but in the same time, the correlation between the two forces $\langle \boldsymbol{F}_I.\boldsymbol{F}_L\rangle$ becomes more and more negative. It turns out that the sum of $\langle \boldsymbol{F}_L^2\rangle + 2\langle \boldsymbol{F}_I.\boldsymbol{F}_L\rangle$ almost exactly cancel in Eq. (8.4) leaving unchanged the bubble acceleration variance. This means that as St^* increases it becomes more likely to have the fluid inertia force and the lift force in the opposite direction. Finally, note that the correlation between the drag and the lift is exactly null because the relative velocity vector and the lift force vector are orthogonal (see the definition of the forces in (3.3) and (3.15)).

In order to explain the observation, we can rewrite the equation of motion Eq. (8.3) as follows:

$$a_{bi} = \frac{u_{bi}}{dt} = (u_{fj} - u_{bj})(\frac{\delta_{ij}}{\tau_b^*} - 2C_L\epsilon_{ijk}\Omega_k) + 3D_t u_{fi} \tag{8.5}$$

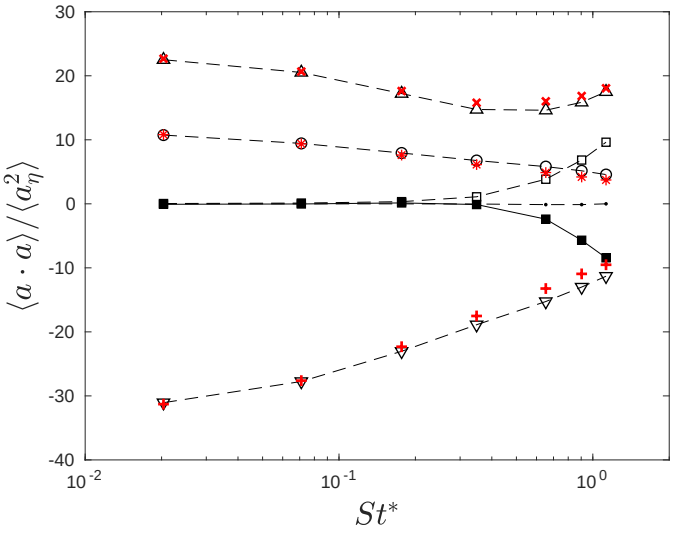

Figure 8.4: The different contribution of the hydrodynamic force to the bubble acceleration variance normalized by the Kolmogorov acceleration a_η^2 for different St^*. Results from simulation without lift force: (x) is the fluid inertia force contribution $\langle \boldsymbol{F}_I^2 \rangle$, (*) is the drag force contribution $\langle \boldsymbol{F}_D^2 \rangle$, (+) is the the correlation between drag force and fluid inertia force $2\langle \boldsymbol{F}_I . \boldsymbol{F}_D \rangle$; Results from simulations with the lift force: ($\triangle$) is the fluid inertia force contribution $\langle \boldsymbol{F}_I^2 \rangle$, ($\circ$) is drag force contribution $\langle \boldsymbol{F}_D^2 \rangle$, ($\triangledown$) is the contribution of the correlation between drag force and fluid inertia force $2\langle \boldsymbol{F}_I . \boldsymbol{F}_D \rangle$, ($\square$) is the lift force contribution $\langle \boldsymbol{F}_L^2 \rangle$, ($\blacksquare$) is the contribution of the correlation between lift force and fluid inertia force $2\langle \boldsymbol{F}_I . \boldsymbol{F}_L \rangle$, ($\cdot$) is the contribution of the correlation between lift force and drag force $2\langle \boldsymbol{F}_D . \boldsymbol{F}_L \rangle$.

where $\mathbf{u}_f$ the fluid velocity, Ω_k is the k component of the vorticity and $D_t \mathbf{u}_f$ is the fluid acceleration vector at the bubble position. We can define a tensorial relaxation frequency

$$\phi_{ij} = (\delta_{ij} \tau_b^{*-1} - 2 C_L \epsilon_{ijk} \Omega_k)^{-1} \tag{8.6}$$

in which we can see two contributions: the contribution of the drag force $\delta_{ij} \tau_b^{*-1}$ and the contribution of the lift force $-2 C_L \epsilon_{ijk} \Omega_k$. The contribution of the drag force tends to reduce the relative velocity by yielding an acceleration vector aligned with the relative velocity whereas the lift force contribution results in a rotation of the acceleration vector relatively to the relative velocity. The three invariants of the tensor ϕ_{ij} are:

$$I_1 = 3 \tau_b^{*-1} \tag{8.7}$$

$$I_2 = 3 \tau_b^{*-2} + C_L^2 (\Omega_{12}^2 + \Omega_{13}^2 + \Omega_{23}^2) \tag{8.8}$$

$$I_3 = \tau_b^{*-3} + \tau_b^{*-1} C_L^2 (\Omega_{12}^2 + \Omega_{13}^2 + \Omega_{23}^2) \tag{8.9}$$

where Ω_{ij} is the rate of rotation tensor, $\Omega_{ij} = \partial_i u_{fj} - \partial_j u_{fi}$. From the Kolmogorov scaling and isotropy, we assume that $\mathcal{O}(\Omega_{12}^2) = \mathcal{O}(\Omega_{13}^2) = \mathcal{O}(\Omega_{23}^2) = \tau_\eta^{-2}$ which enables to estimate the invariant of the tensor normalized by τ_η as

$$I_1 \approx St^{*-1} \tag{8.10}$$

$$I_2 \approx 3(St^{*-2} + C_L^2) \tag{8.11}$$

$$I_3 \approx St^{*-3} + 3C_L^2 St^{*-1} \tag{8.12}$$

Accordingly, the canonical form of the tensor ϕ in non-dimensional form is:

$$\phi_c \approx \begin{bmatrix} St^{*-1} & -\sqrt{3}C_L & 0 \\ \sqrt{3}C_L & St^{*-1} & 0 \\ 0 & 0 & St^{*-1} \end{bmatrix} \tag{8.13}$$

Therefore it is clear that the dynamic system given by $\dot{\mathbf{x}} = -\mathbf{x}\phi_c$ corresponds to spiraling motion going inward to the origin. As expected the rate of rotation is controlled by the value of the lift coefficient while the compression rate is given by the inverse of the Stokes number. When the Stokes number is very small the diagonal term are dominant compared to the off-diagonal terms, since in that case the lift coefficient is very small due to the smallness of the Reynolds number (see the expression for the lift coefficient in Eq. (3.18). Therefore the drag force can very quickly adjust to the forcing caused by the fluid inertia force, resulting in a drag force and an inertia force in the opposite direction. On the other hand, for larger Stokes number, the lift coefficient presents larger value and we have the opposite situation as the lift coefficient dominates over St^{*-1}. As a consequence, when the bubble resides in a region of the flow dominated by rotation the lift force has a centrifugal orientation, pointing outward the vortex while the fluid inertia is a centripetal force pointing inward and therefore they are both anti-aligned. This picture explains the negative correlation between lift and inertia observed in Figure 8.4, and thus the absence of the effect of the lift force on the bubble dynamics despite the fact that the force itself can have a non-negligible magnitude.

8.2 The lift force effect on rising velocity

In this section, we study the motion of a bubble subjected to gravity in addition to drag, fluid inertia and lift in turbulent flow. We would like to investigate how the interplay of lift and buoyancy forces can significantly modify the bubble dynamics, and in first place its rising speed as reported in the beginning of Chapter 7, whereas we have shown in the previous section that the lift force has a negligible effect on the motion of a bubble in a turbulent flow. To carry out this study, we performed DNS of turbulent flow using again the pointwise particle approximation to track the bubble motion. In this section we consider the following force balance equation for the bubbles:

$$\boldsymbol{a}_b = \frac{d\boldsymbol{u}_b}{dt} = \frac{\boldsymbol{u}_f - \boldsymbol{u}_b}{\tau_b}\mathcal{F}(Re_b) + 3\frac{D\boldsymbol{u}_f}{Dt} + 2C_L(\boldsymbol{u}_f - \boldsymbol{u}_b) \times \boldsymbol{\Omega}_f - 2\boldsymbol{g} \quad (8.14)$$

The simulation parameters can be found in table 6.1 for the fluid field and table 7.1 for the bubble size and Stokes number. We recall that due to the non-linear drag terms the effective terminal velocity is expressed as $V^*_{term} = (1-\beta)\boldsymbol{g}\tau^*_b$ and the relevant Stokes number is $St^* = \tau^*_b/\tau_\eta$.

We present in figure 8.5, the evolution with St^* of the average rising velocity of the bubble $\langle u_{bz}\rangle$ normalized by its terminal velocity V^*_{term} from the DNS with or without the lift force. It appears that the rising speed is smaller with the lift force in the budget than without:

$$V^*_{term} > \langle u_{bz}\rangle_{\text{without lift}} > \langle u_{bz}\rangle_{\text{with lift}} \quad (8.15)$$

We observe that for $St^* \approx 1$ the average rising speed can be as low as $0.5\,V^*_{term}$. Remark that for $St^* = 0.02$, the rising velocity in case of no lift force is slightly larger than the terminal velocity.

In order to study the effect of lift force on the rising velocity, the average relative vertical velocity $\langle W_{ref}\rangle = \langle u_{bz} - u_{fz}\rangle$ is compared in figure 8.6, with the results obtained without the lift force (and presented in Chapter 7). We observe that DNS with the lift force, gives $\langle W_{ref}\rangle$ closer to the terminal velocity than DNS without lift force:

$$V^*_{term} > \langle W_{ref}\rangle_{\text{with lift}} > \langle W_{ref}\rangle_{\text{without lift}} \quad (8.16)$$

As a consequence, we can say that the bubbles are more prone to be found in the region of the flow with negative vertical velocity when the lift force is accounted for. This is confirmed in figure 8.7 which presents the evolution with St^* of the average value of the fluid vertical velocity at the bubble position for the two sets of simulations. It is observed that without the lift

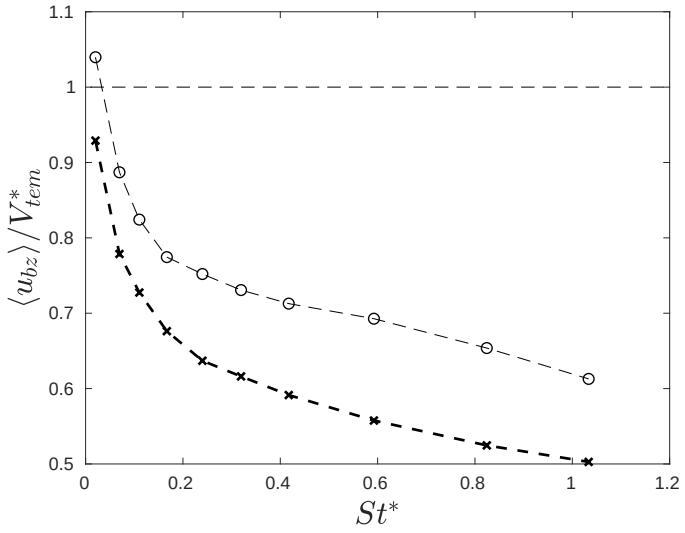

Figure 8.5: The average value of the rising velocity $\langle u_{bz} \rangle$ normalized by the terminal velocity V^*_{term}. (○): DNS without lift force, (x): DNS with lift force.

force the average fluid velocity at the bubble position presents a (negative) minimum value for $St^* \approx 0.2$, while with the lift force the average fluid vertical velocity decreases continuously up to $St^* \approx 1$.

$$0 > \langle u_{fz} \rangle_{\text{without lift}} > \langle u_{fz} \rangle_{\text{with lift}} \tag{8.17}$$

This situation seems surprising as Eq. (8.15) and Eq. (8.17) appear to be in contradiction with Eq. (8.16). This could be explained by proposing that two mechanisms can lead to the reduction of the rising speed: (i) bubble trapping in flow vortex and (ii) oversampling of the downward flow region by bubbles. The reduction of the average relative velocity compared to the terminal velocity is attributed to the first mechanism. Therefore the increase of the relative velocity of the DNS with lift relatively to the DNS without lift indicates that the addition of the lift force makes the vortex trapping less efficient. Indeed, as discussed above, when a bubble is in a vortex, the lift force is centrifugal and can help the bubble to escape from the vortex.

To assess further the trapping by vortex, we plot in figure 8.8 the average value of the vertical inertia forces acting on the bubble in each case against St^*. We observe that the average value of the fluid acceleration $\langle a_{fz} \rangle$ is negative (except for the two smallest Stokes numbers) and that the values computed from DNS with lift force are less negative than the results from DNS without lift force. Following the analysis of the previous chapter, the

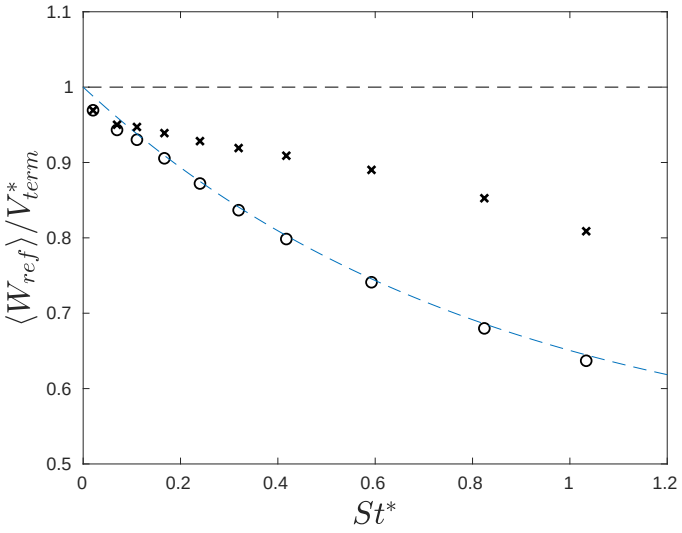

Figure 8.6: The average value of the vertical relative vertical velocity $\langle W_{ref} \rangle$ normalized by the terminal velocity V^*_{term}. ∘: DNS without lift force, x: DNS with lift force. (- -) is a empirical fitting with $\langle W_{rel} \rangle / V^*_{term} = \frac{\exp(-1.2\,St^*)-1}{2}$.

reduction of the average relative vertical velocity $\langle W_{ref} \rangle$ is related to the negative average value of the fluid acceleration sampled by the bubbles when trapped in a vortex. Therefore the observation that the fluid acceleration at the bubble position is less negative with the lift force accounted for is consistent with a reduced efficiency of the vortex trapping.

To propose a more quantitative analysis of the effect of the lift force on the vortex trapping, we consider again the idealized situation of a bubble in a vortex as discussed in Chapter 7. We consider that the vortex has a steady rotation rate ω, and we supplement the bubble force equation with the lift force as sketch in figure 8.9. We recall that in cylindrical coordinate $(\boldsymbol{e}_r, \boldsymbol{e}_\theta)$ at a given radial distance r the velocity is $\boldsymbol{u}_f = r\omega \boldsymbol{e}_\theta$, the fluid acceleration is $\boldsymbol{a}_f = -r\omega^2 \boldsymbol{e}_r$ and the vorticity is $\boldsymbol{\Omega} = 2\omega \boldsymbol{e}_y$. When the bubble has reached its equilibrium position, denoted as (r_e, θ_e), the drag force is $\boldsymbol{F}_D = (0, \frac{r_e \omega}{\tau_b^*})$, the fluid inertia force is $\boldsymbol{F}_I = (-3r_e\omega^2, 0)$, the lift force is $\boldsymbol{F}_L = (4C_L r_e \omega^2, 0)$ and the buoyancy force $\boldsymbol{F}_g = (-(1-\beta)gsin(\theta_e), -(1-\beta)gcos(\theta_e))$. The resulting dynamic equilibrium yields:

$$0 = 0 - 3r_e\omega^2 + 4C_L r_e \omega^2 + 2g\sin(\theta_e) \tag{8.18}$$

$$0 = \frac{r_e \omega}{\tau_b^*} + 0 + 2g\cos(\theta_e) \tag{8.19}$$

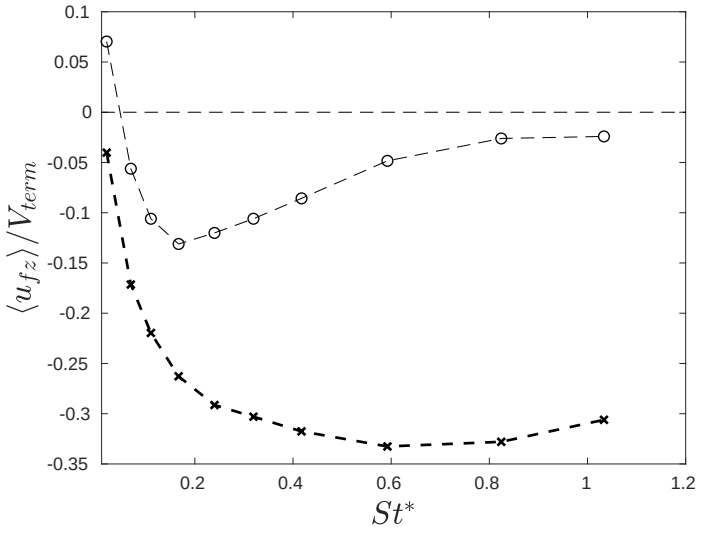

Figure 8.7: The average value of the vertical component fluid velocity at the bubble position normalized by the global fluid velocity RMS. (∘): DNS without lift force, (x): DNS with lift force.

and transform to

$$\sin\theta_e = -\frac{(4C_L - 3) r_e \omega^2}{2g} \tag{8.20}$$

$$\cos\theta_e = -\frac{r_e \omega}{2g\tau_b^*} \tag{8.21}$$

We can see that $\cos\theta_e$ is always negative, however, because of the introduction of the lift coefficient, the sign of $\sin\theta_e$ is not necessarily positive contrary to the case without lift force. As seen from the equation above if $C_L < 0.75$ then $\sin\theta_e > 0$, and the equilibrium position lies in the same top left quadrant as if there was no lift force. We recall that in that quadrant the fluid acceleration and velocity are both negative. However if $C_L > 0.75$, the bubble equilibrium position shift in the region where the fluid acceleration is positive and the fluid velocity is positive. Of course, the turbulent structure is much more complicated. The fluid structure will deform in a short period of time but this analysis helps us to understand the phenomenon. In the insert of figure 8.8, for small St^* the mean lift force coefficient is seen to be larger than 0.75. And indeed, we can see that the mean value of the fluid acceleration at the first two points is positive. For larger St^*, the mean value of the lift coefficient becomes smaller than 0.75, and the fluid acceleration presents negative mean values. As St^* increases further the fluid acceleration becomes comparable to the effective gravity $(1-\beta)\boldsymbol{g}$, resulting

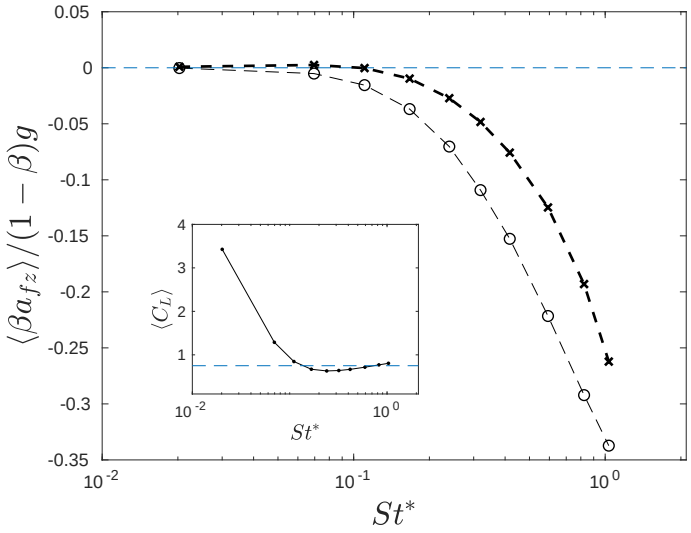

Figure 8.8: The evolution of average value of the vertical component fluid inertia force $\langle 3a_{fz}\rangle$ normalized by the effective buoyancy force against St^*. ($\circ$): DNS without lift force, (x): DNS with lift force. Inset: is the evolution of the average lift coefficient against St^*, dash line shows $C_L = 0.75$.

in a slow down of the bubble rise. For large St^*, a bubble will drift through the turbulent structure under the buoyancy effect. During this process the bubble will have a longer time to stay, or just say being trapped, at the upper body with the downward stream of the horizontal vortex structure due to this equilibrium positioning tendency. In other words, it makes the gravity harder to drive the bubble when it is in the equilibrium position. That explains why this over sampling of the negative fluid acceleration region.

To confirm this picture, we present, for different St^*, in figure 8.10 the average rising velocity conditioned on vertical component of the fluid acceleration a_{fz}: $\langle u_{bz}|a_{fz}\rangle$. The conditional average is normalized by the unconditional average value. We can see that the bubble vertical velocity is faster on average when it is experiencing a positive fluid acceleration. On the contrary, the bubble rises slower, on average, or even have negative vertical velocity, when the fluid acceleration at his position is negative. A further evidence is provided in figure 8.11, where we plot the iso-contours of joint *pdf* between the relative velocity of bubbles in the z-direction normalized by the terminal velocity W_{ref}/V_{term} and the z-component of the fluid acceleration at the bubble position a_{fz}/a_η. The variance of the vorticity at the bubble position normalized by the variance of the fluid field is also plotted in figure 8.12. We found that the variance of the vorticity at the bubble position increases

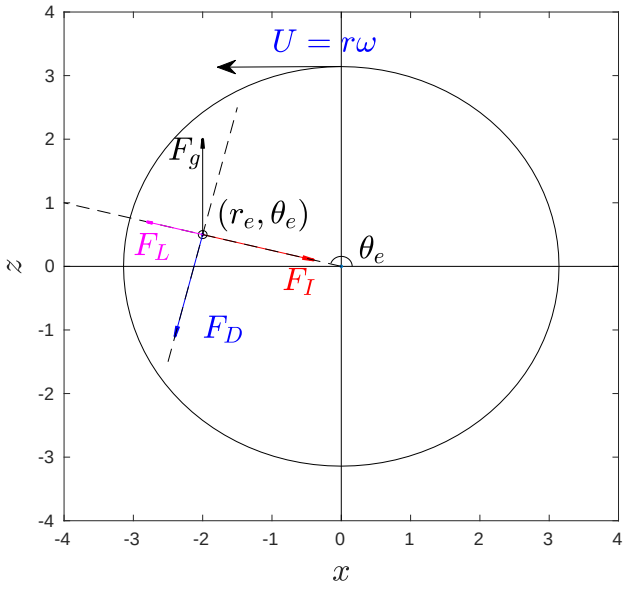

Figure 8.9: Sketch to illustrate bubble equilibrium in a steady rotation with anticlockwise angular speed of ω, accounting for drag $\boldsymbol{F}_D$, fluid inertia $\boldsymbol{F}_I$, buoyancy $\boldsymbol{F}_g$ and lift $\boldsymbol{F}_L$ forces acting on the bubble.

with St^* and the increase rate in the z-direction is higher than in the horizontal direction. The reason is that with St^* increases, it becomes easier for the bubble to pass between strong vorticity region and weak vorticity region whereas a bubble with small St^* behaves simply like a tracer. The buoyancy force in the z-direction enhances the fluctuations of the vorticity experienced by a bubble.

When a bubble interacts with an horizontal vortex, when it is in the bottom part, in which $a_{fz} > 0$, the bubble will spend a shorter time passing this region and go to the upper part of the vortex, in which $a_{fz} < 0$. Then the bubble slows down in this region and might therefore spend a longer time in the area. The bubble will repeat this procedure until the vortex structure breakup or until the bubble escape from the vortex. Additionally, the lift force tends to help the bubble to escape the vortex, because the lift force acts as centrifugal force in the situation.

In figure 8.13, the one component bubble acceleration variance normalized by the a_η^2 is presented for the DNS (lift force, drag, fluid inertia force) results with/without gravity. In general, by enabling the gravity, the bubble acceleration is enhanced, the observation can be explained by the previous conclusion that the bubble acceleration variance will be enhanced by gravity. The enhancement is getting larger with the increase of St^*. In figure 8.14

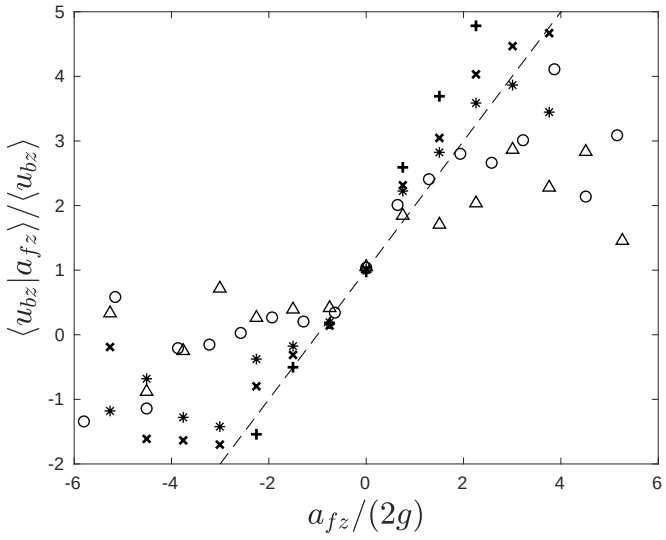

Figure 8.10: The average bubble velocity conditioned on the vertical component of the fluid acceleration $\langle u_{bz}|a_{fz}\rangle$, (+) $St^* = 0.17$, (x) $St^* = 0.32$, (*) $St^* = 0.42$, ($\circ$) $St^* = 0.60$, ($\triangle$) $St^* = 1.01$, in the simulation considering lift force, drag force, fluid inertia force and gravity.

presents the bubble acceleration *pdf*s obtained from the same simulations with/without gravity is reported. It is observed that, the bubble acceleration *pdf*s clearly present a non-Gaussian behavior with stretched tails indicating the occurrence of very intense acceleration events. The *pdf*s presents a good collapse for the various St^*.

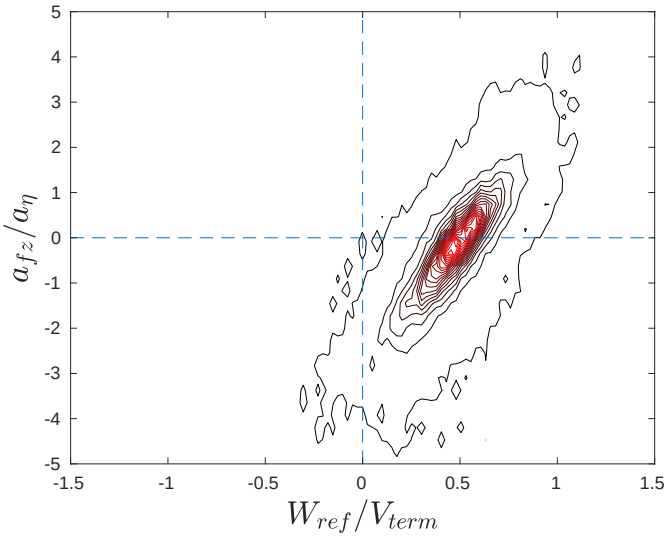

Figure 8.11: The iso-contours of joint *pdf* between the relative velocity of the bubble in z-direction W_{ref}/V_{term} and the z-component fluid acceleration a_{fz}/a_η, in the simulation accounting for lift force, drag force, fluid inertia force and gravity for $St^* = 0.9$. From black to red density increases.

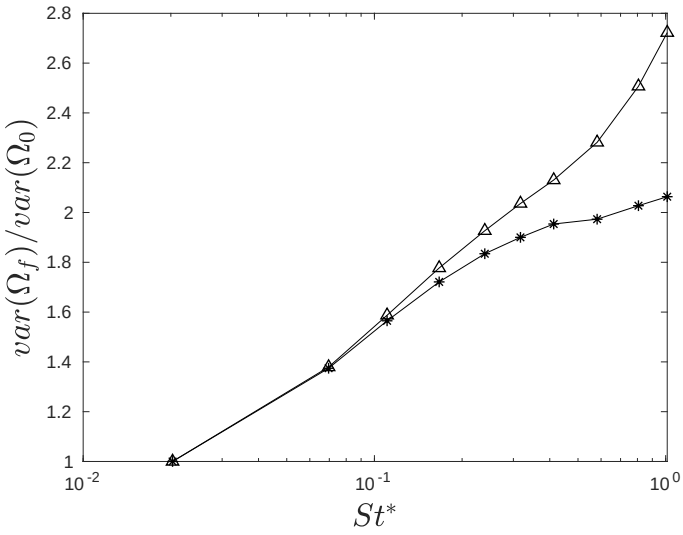

Figure 8.12: The evolution of the vorticity variance at bubble position normalized by the fluid field vorticity variance versus St^*, ($\triangle$) is the vorticity in z-direction, (*) is the vorticity in x-direction, in the simulation considering drag force, fluid inertia force, lift force and gravity.

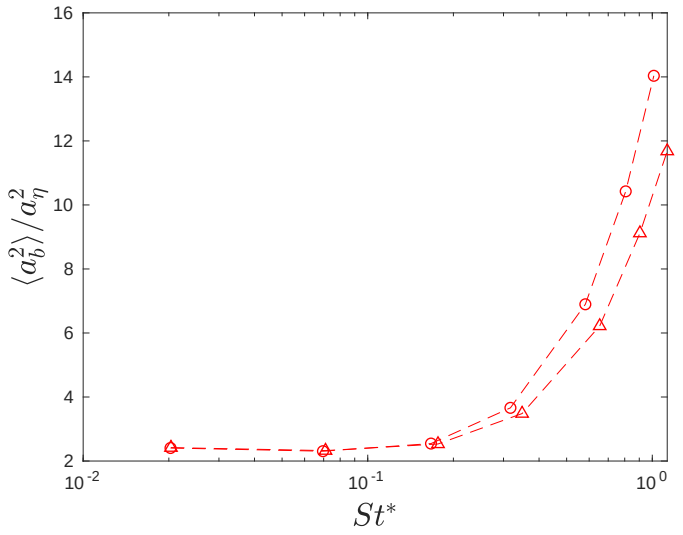

Figure 8.13: The evolution of the bubble acceleration variance $\langle a_b^2 \rangle$ normalized with the square of Kolmogorov acceleration a_η^2 versus St^*, ($\triangle$) is the results from the simulation accounting for drag force, fluid inertia force, lift force and no gravity, ($\circ$) is the results from the simulation accounting for drag force, fluid inertia force, lift force and gravity.

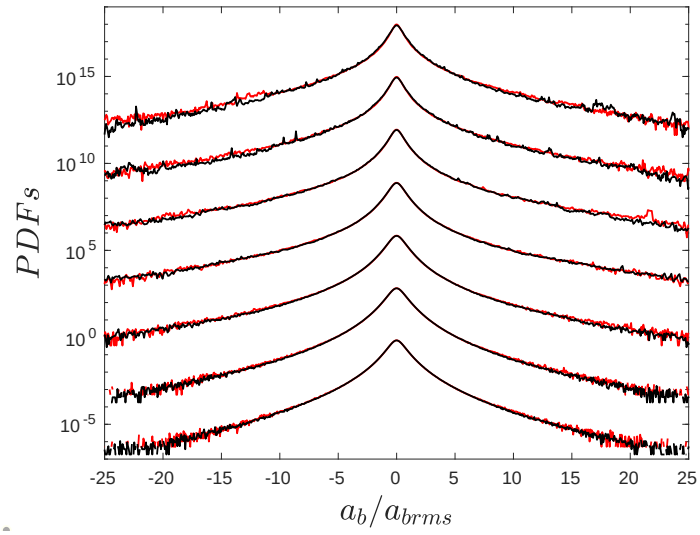

Figure 8.14: (- -)*pdf*s of the bubbles acceleration of the simulation accounting for (drag force, fluid inertia force, lift force but no gravity) normalized by its root-mean-square value, (–) *pdf*s of the bubbles acceleration of the simulation accounting for (drag force, fluid inertia force, lift force and gravity) normalized by its root-mean-square value, for $St^* = 0.02$, 0.07, 0.18, 0.35, 0.6, 0.90, 1.13 (respectively, shifted upward by two decades from each other for clarity)

8.3 Conclusions

In this chapter, we studied the effect of the lift force on the bubble motion in turbulent flow by using Euler-Lagrangian approach.

In order to investigate the influence of the lift force on the bubble acceleration statistics, we firstly isolate the effect of lift force from the gravity by only accounting for drag force, fluid inertia force, lift force and setting the buoyancy force to zero. The results are compared to the simulations where only drag force and fluid inertia force are considered. The results show that, the influence of the lift force to the bubble acceleration is very limited. Despite the fact that for $0.65 < St* < 1.1$, the lift force have comparable variance to the fluid inertia force, it has no sizable influence on the bubble acceleration statistics. Because in the same time the correlation between lift force and fluid inertia force becomes more and more negative such that the contribution of lift force on the variance of the total acceleration variance is neutralized.

In the second part, we performed simulations accounting for drag force, fluid inertia force, lift force and buoyancy force to investigate how the lift force influence the bubble motion with the presence of gravity. We have found that the lift force has a greater impact on the bubble motion compared to the case where the gravity is disabled. The lift force makes the bubble have a preferential sampling to the down flow region. This reduces significantly the bubble rising velocity. The fluid material acceleration at the bubble position has a negative average value $\langle a_{fz} \rangle < 0$, which can contribute to the fluid inertia force. Compared with the simulation where there are only drag force, fluid inertia force and buoyancy force, the simulation accounting for lift force has larger value of $\langle a_{fz} \rangle$. Based on the analysis of a bubble in a vortex rotating with a constant rotation rate, we found that the lift force has a tendency to prevent the bubble from being trapped in the vortex. It pushes the bubble to the down flow region and act like a centrifuge force while the bubble is trapping in the vortex by fluid inertia force who is a centripetal force.

When we are interested in the bubble acceleration statistics for $St^* \ll 1$, the bubble is so small that only the drag force and the fluid inertia force are relatively important compared to other forces contribution. Thus, this study justifies that the lift force can be neglected, if we are only interested in the motion of small bubbles as in Chapter 5. While the lift force affect to long-distance transport phenomena, due to it's influence on the bubble's spatial distribution.

Chapter 9

General conclusions

This thesis is focused on the study of micro-bubbles ($d_b < \eta$) motion in high Reynolds number isotropic and homogeneous turbulent flows by using numerical approach. The Euler-Lagrange method is used to solve the two-phase turbulence problems in a one-way coupling approach.

We performed DNS to resolve the turbulent flow field in a 3D box with periodic boundary conditions. The turbulence field is resolved with two different Reynolds number $Re_\lambda = 100$ and $Re_\lambda = 200$. The spectral method is applied to resolve the Navier-Stokes equations with a forcing at large scales to maintain a statistically steady state. The small bubbles are treated as a sphere with slip boundary condition and is tracked with the equation of motion which is given by Newton's equation, using the fluid information interpolated at the bubble position to compute the different hydrodynamic forces acting on the bubble.

We first began by considering exclusively the drag force in Stokes regime and fluid inertia force in the equation of motion. For small Stokes numbers, the two forces are commensurate and are found to be preferentially anti-aligned, whereas for larger Stokes numbers the drag force becomes negligible and the bubble acceleration is essentially given by the fluid inertia forces resulting in a bubble acceleration variance larger than that for fluid tracers. We proposed a model, depending on the Stokes number, the Reynolds number and the density ratio, describing qualitatively these observations. The model based on the spectral response of the bubble to the fluid fluctuations (similar to the Tchens theory) assumes firstly the shape of the frequency spectra of the fluid velocity along the bubble position (with a ω^{-2} power law), and secondly that the material derivative of the fluid velocity at the bubble position can be substituted by the time derivative along the bubble trajectories. These assumptions lead to fairly accurate estimations for small $St < 1$, and

some deviations are observed for $St \approx 1$ as the preferential concentration of bubbles is not accounted for. This effect could be taken into account in the model, by providing more precise, St dependent, estimation of the high frequency part of the Lagrangian fluid velocity spectra and of the fluid acceleration variance at the bubble position. It is further observed that the micro-bubble acceleration conditioned on the local dissipation rate presents a surprising invariant. For values of the local dissipation rate similar or larger than the average one, the conditional acceleration variance appears to be invariant with the Stokes number and increases with the dissipation rate, whereas the conditional *pdf*s are observed to be nearly invariant with the dissipation rate and the Stokes number when normalized by the conditional variance. Such invariance was not expected because of the very intense clustering of the bubbles as reported by [71] around $St = 1$. Indeed, at small Stokes number bubbles behave like fluid tracers, whereas for Stokes numbers of order 1 (for which one can neglect the drag force) the acceleration of a bubble is roughly $\beta = 3$ times that of a tracer at the same position. Nevertheless the near invariant of the conditional statistics implies that in the two cases, bubbles sample fluid regions in which the fluid acceleration conditional statistics are the same as in the entire domain. This observation can provide some help to study the β and St dependence of the clustering morphology of the bubbles.

Secondly, to extend the scope of the studies in Chapter 5, we considered the effect of finite bubble Reynolds numbers Re_b to the acceleration statistics. It has been observed that the Reynolds number effect to the drag force is essential for the bubble dynamics when $Re_b > 1$. Computed from the simulation we found that, even for the bubbles with $d_b < \eta$, it is possible to observe Reynolds number value lager than unity. Using the drag law in the Stokes regime to calculate the drag force, in such case, will underestimate the instantaneous drag force as well as its statistical values. It is necessary to use nonlinear drag law to compute the drag force.

We have tested two other drag force coefficients in the DNS, one in the case of clean bubble Eq.(3.8) and another for the case of contaminated surface bubble Eq.(3.9). With the introduction of the finite Reynolds number effect, the bubble will response faster to the fluid velocity, resulting in smaller relative velocity fluctuations and larger drag force fluctuations for the same value of St compared to the results using Stokes drag force. These differences are increasing with the increase of St. Besides, the nonlinear drag law leads to longer decorrelation time of the bubble acceleration due to the reduction of the effective relaxation time. These above observations provide evidence that in turbulent flow, the fluid inertia force drives the bubble motion and the drag force is enslaved.

We have proposed a method to scale the characteristic relaxation time τ_b^* to account for the finite bubble Reynolds number effect and further the effective Stokes number St^* with the average value of $\langle Re_b \rangle$, by accounting for the first order effect of the local bubble Reynolds number. This rescaled characteristic times enables to obtain a similar behavior to the drag law in Stokes regime for various statistical quantities.

Thirdly, we have investigated how does the buoyancy influence the bubble dynamics in turbulent flows, by tracking the bubble trajectory with the equation of motion including drag force (Stokes or nonlinear drag), the fluid inertia force and the buoyancy force. We found that even without lift force the bubble still slightly oversampling the downstream of flow. The oversampling effect will increase with St and saturate around $St \simeq 0.5$. But the main reason for the reduction of the rising speed is the negative value of the average vertical component of the fluid inertia (i.e. fluid acceleration at the bubble position). Furthermore, we examined the gravity effect on the bubble acceleration statistics. The gravity increases the acceleration variance and decreases its flatness for small Froude number $Fr < 1$. The observation is coherent with the results presented in the experimental study of [70]. The acceleration is also observed to remain correlated over a long period compared to the case without gravity.

Finally, we have studied the lift force effect on bubble dynamics. In order to see the lift force effect on the acceleration statistics, we solve the bubble equation of motion including nonlinear drag force, fluid inertia force, lift force and disabled gravity. We have found that the lift force have a very limited effect on the bubble acceleration statistics for the bubble with $St < 1.1$. Although the lift force variance increases progressively with the increase of St, its contribution to the total bubble acceleration variance is neutralized by the correlation between the lift force and the fluid inertia force. Then we enabled the gravity and we have confirmed that, when a bubble is rising in turbulent flow, the lift force makes the bubble to preferably move in down flow regions. Besides, compared with the simulation where there are only drag force, fluid inertia force and buoyancy force, the simulations accounting for lift force have larger value of vertical fluid acceleration $\langle a_{fz} \rangle$. Based on the analysis of a bubble in a vortex rotating with a constant rotation rate, we found that the lift force has a tendency to prevent the bubble from being trapped in the vortex. It pushes the bubble to the down flow region and acts like a centrifuge force while the bubble is trapping in the vortex by fluid inertia force who is a centripetal force. Furthermore, we also compared the bubble acceleration variance of the simulation with and without gravity. We found that as expected, in the simulation with gravity, the bubble variances are larger than that in the simulation without gravity. We concluded that the contribution of the lift force is important for the bubble acceleration

statistics only when the buoyancy force is important. When $St^* \ll 1$, the bubble is so small that only the drag force and the fluid inertia force are relatively important compared to other forces contribution. This study justifies that the lift force is not important, if we are only interested in the motion of small bubbles, as in Chapter 5.

Based on the observations of the simulation where only drag force and fluid inertia force are of interests, we have proposed, within the LES framework, an extension of the approach of [24] in order to account for the unresolved fluid turbulent fluctuations in the dynamics of micro-bubbles for locally homogeneous and isotropic high-Reynolds number flows. To this end, the instantaneous acceleration of the bubble is decomposed into a filtered contribution given by the resolved fluid velocity field and a random contribution. The stochastic part is given by the sum of two correlated random processes, one for the drag forces and the second for the fluid inertia terms. For the instantaneous norm of both forces, we consider the fluctuations of the energy transfer rate, relying on the fact that the fluctuations of the norm are self-similar for a given value of the energy transfer rate. For the latter a surrogate is obtained by a log-normal stochastic process evolving along the bubble trajectory. Whereas the former, which is observed to be invariant, is estimated from the variance of the forces conditioned on the dissipation rate as obtained from the model which has been proposed based on the Tchen theory. The residual part is supplemented by a stochastic process for the orientations of the two forces. The model is given by two coupled random walks on the surface of the unit sphere, which enables us to reproduce the progressive decorrelation of the force components, their correlation with the large-scale motion, as well as the return to local isotropic for sufficiently large-scale separation, and the preferential anti-alignment of the two forces observed for $St < 1$. To summarize, the model depends on the Stokes number and the β parameter of the bubbles as well as a local Reynolds number Re_Δ based on the mesh size. In addition few parameters of the model need to be prescribed from the DNS. The comparisons of the statistics obtained with LES supplemented by the proposed stochastic model with the ones obtained from DNS confirmed that the dynamics of the bubbles can be accurately computed using this approach even for very coarse meshes while the standard LES approach (without stochastic modeling for the high frequency fluctuations) fails to reproduce the statistics of the DNS. Nevertheless, the bubble clustering at sub-grid scales or short-time relative dispersion is not improved by the modeling presented in this paper because the estimation of the dissipation rates along each bubble trajectory is obtained by independent stochastic processes. The derivation of the proposed model is made for arbitrary density ratio, although, in this thesis we only focus on the micro-bubble regime $\beta = 3$. It can be shown that for $\beta = 0$ our model becomes equivalent to the formulation proposed for inertial particles in [24]. More-

over, for neutrally dense particles $\beta = 1$, the proposed model would provide results equivalent to those obtained for vanishingly small Stokes number, as expected for particles much smaller than the Kolmogorov scales.

The assessment of the model for intermediate values of β is also interesting but is postponed for future work. Also interesting is to account for other forces that can have a non-negligible role on the bubble dynamics (buoyancy, lift and history). As well, accounting for the deformation of the bubbles is necessary if one is interested in bubbles larger than the micro-scale of the flow ($d_b > \eta$). Finally, we have focused on the modeling of the sub-grid scale for homogeneous and isotropic turbulent flow. Nevertheless, we think that the model proposed in this paper could provide acceptable results for flows that can be considered locally isotropic and homogeneous at the scale of the mesh, since the main parameters of the model are defined locally.

Bibliography

[1] T.G. Leighton, D.G.H. Coles, M. Srokosz, P.R. White, and D. K. Woolf. Asymmetric transfer of CO_2 across a broken sea surface. *Nature: Scientific Reports*, 8:2045–2322, 2018.

[2] S.C. Doney, L. Bopp, and M.C. Long. Historical and future trends in ocean climate and biogeochemistry. *Oceanography*, 27, 2014.

[3] B. Jacob, A. Olivieri, M. Miozzi, E.F. Campana, and R. Piva. Drag reduction by microbubbles in a turbulent boundary layer. *Physics of Fluids*, 22(11):115104, 2010.

[4] W.C. Sanders, E.S. Winkel, D.R. Dowling, M. Perlin, and S.L. Ceccio. Bubble friction drag reduction in a high-Reynolds-number flat-plate turbulent boundary layer. *Journal of Fluid Mechanics*, 552:353380, 2006.

[5] M.R. Maxey and J.J. Riley. Equation of motion for a small rigid sphere in a nonuniform flow, 1983.

[6] M.R. Maxey, E.J. Chang, and L.P. Wang. The motion of microbubbles in a forced isotropic and homogeneous turbulence. *Applied Scientific Research*, 51(1):291–296, 1993.

[7] R. Mei, R.J. Adrian, and T.J. Hanratty. Particle dispersion in isotropic turbulence under stokes drag and basset force with gravitational settling. *Journal of Fluid Mechanics*, 225:481495, 1991.

[8] P. Bagchi and S. Balachandar. Effect of turbulence on the drag and lift of a particle. *Physics of Fluids*, 15(11):3496–3513, 2003.

[9] J. Bec. Multifractal concentrations of inertial particles in smooth random flows. *Journal of Fluid Mechanics*, 528:255277, 2005.

[10] J. Bec, L. Biferale, G. Boffetta, A. Celani, M. Cencini, A. Lanotte, S. Musacchio, and F. Toschi. Acceleration statistics of heavy particles in turbulence. *Journal of Fluid Mechanics*, 550:349358, 2006.

[11] M.R. Maxey, E.J. Chang, and L.P. Wang. simulation of interactions between micro-bubble and turbulent flow. *Appl Mech Rev*, 47(6):s71–s74, 1994.

[12] P.D.M. Spelt and A. Biesheuvel. Dispersion of gas bubbles in large-scale homogeneous isotropic turbulence. *Applied Scientific Research*, 58(1):463–482, 1997.

[13] I.M. Mazzitelli, D. Lohse, and F. Toschi. On the relevance of the lift force in bubbly turbulence. *Journal of Fluid Mechanics*, 488:283313, 2003.

[14] I.M. Mazzitelli and D. Lohse. Lagrangian statistics for fluid particles and bubbles in turbulence. *New Journal of Physics*, 6:203–203, 2004.

[15] P. Sagaut. *Turbulence Direct Numerical Simulation and Large-Eddy Simulation*. American Cancer Society, 2004.

[16] V. Sabel'nikov, A. Chtab-Desportes, and M. Gorokhovski. New sub-grid stochastic acceleration model in les of high-Reynolds-number flows. *The European Physical Journal B*, 80(2):177–187, 2011.

[17] G.A. La Porta, A.and Voth, A.M. Crawford, J. Alexander, and E. Bodenschatz. Fluid particle accelerations in fully developed turbulence. *Nature*, 409:1017 –1019, 2001.

[18] N. Mordant, A.M. Crawford, and E. Bodenschatz. Three-dimensional structure of the lagrangian acceleration in turbulent flows. *Phys. Rev. Lett.*, 93:214501, 2004.

[19] G. A. Voth, A. La Porta, A. M. Crawford, J. Alexander, and E. Bodenschatz. Measurement of particle accelerations in fully developed turbulence. *Journal of Fluid Mechanics*, 469:121160, 2002.

[20] J.M. Mercado, V.N. Prakash, Y. Tagawa, C. Sun, and D. Lohse. Lagrangian statistics of light particles in turbulence. *Physics of Fluids*, 24(5):055106, 2012.

[21] H. Homann, D. Schulz, and R. Grauer. Conditional eulerian and lagrangian velocity increment statistics of fully developed turbulent flow. *Physics of Fluids*, 23(5):055102, 2011.

[22] N. Mordant, P. Metz, O. Michel, and J.F. Pinton. Measurement of lagrangian velocity in fully developed turbulence. *Phys. Rev. Lett.*, 87:214501, 2001.

[23] S.B. Pope and Y.L. Chen. The velocitydissipation probability density function model for turbulent flows. *Physics of Fluids A: Fluid Dynamics*, 2(8):1437–1449, 1990.

[24] M. Gorokhovski and R. Zamansky. Modeling the effects of small turbulent scales on the drag force for particles below and above the kolmogorov scale. *Physical Review Fluids*, 3(3):1–23, 2018.

[25] C. M. Tchen. *Mean value and correlation problems connected with the motion of small particles suspended in a turbulent fluid. PhD thesis.* Delft University, Netherlands, 1947.

[26] R. Mei. Velocity fidelity of flow tracer particles. *Experiments in Fluids*, 22(1):1–13, 1996.

[27] E. Calzavarini, R. Volk, M. Bourgoin, E. Lévêque, J.F. Pinton, and F. Toschi. Acceleration statistics of finite-sized particles in turbulent flow: the role of faxn forces. *Journal of Fluid Mechanics*, 630:179189, 2009.

[28] R. Volk, N. Mordant, G. Verhille, and J.-F. Pinton. Laser doppler measurement of inertial particle and bubble accelerations in turbulence. *EPL (Europhysics Letters)*, 81(3):34002, 2007.

[29] S.B. Pope, J.T. Stuart, and M. Tabor. Lagrangian microscales in turbulence. *Philosophical Transactions of the Royal Society of London. Series A: Physical and Engineering Sciences*, 333(1631):309–319, 1990.

[30] H.L. Grant, R.W. Stewart, and A. Moilliet. Turbulence spectra from a tidal channel. *Journal of Fluid Mechanics*, 12(2):241268, 1962.

[31] A.M. Oboukhov. Some specific features of atmospheric tubulence. *Journal of Fluid Mechanics*, 13(1):7781, 1962.

[32] A.N. Kolmogorov. A refinement of previous hypotheses concerning the local structure of turbulence in a viscous incompressible fluid at high Reynolds number. *Journal of Fluid Mechanics*, 13(1):8285, 1962.

[33] K.R. Sreenivasan and R.A. Antonia. The phenomenology of small-scale turbulence. *Annual Review of Fluid Mechanics*, 29(1):435–472, 1997.

[34] A.S. Monin and A.M. Yaglom. *Statistical Fluid Mechanics: The Mechanics of Turbulence:volume 1.* Cambridge University Press, 1973.

[35] T.D. Taylor and A. Acrivos. On the deformation and drag of a falling viscous drop at low reynolds number. *Journal of Fluid Mechanics*, 18(3):466476, 1964.

[36] V.G. Levich. *Physicochemical Hydrodynamics.* Prentice-Hall, 1962.

[37] J. F. Harper and D. W. Moore. The motion of a spherical liquid drop at high Reynolds number. *Journal of Fluid Mechanics*, 32(2):367391, 1968.

[38] R. Mei, J.F. Klausner, and C. J. Lawrence. A note on the history force on a spherical bubble at finite Reynolds number. *Physics of Fluids*, 6(1):418–420, 1994.

[39] R. Clift, J.R. Grace, and M.E. Weber. *Babble, drops and particles.* Academic press, New York, 1978.

[40] J. Magnaudet, M. Rivero, and J. Fabre. Accelerated flows past a rigid sphere or a spherical bubble. part 1. steady straining flow. *Journal of Fluid Mechanics*, 284:97135, 1995.

[41] S.M. Yang and L.G. Leal. A note on memoryintegral contributions to the force on an accelerating spherical drop at low Reynolds number. *Physics of Fluids A: Fluid Dynamics*, 3(7):1822–1824, 1991.

[42] D. Legendre, A. Rachih, S. Souilliez, C.and Charton, and E. Climent. Basset-boussinesq history force of a fluid sphere. *Phys. Rev. Fluids*, 4:073603, 2019.

[43] W.C. Park, J.F. Klausner, and R. Mei. Unsteady forces on spherical bubbles. *Experiments in Fluids*, 19(3):167–172, 1995.

[44] D. Legendre and J. Magnaudet. A note on the lift force on a spherical bubble or drop in a low-Reynolds-number shear flow. *Physics of Fluids*, 9(11):3572–3574, 1997.

[45] P.G. Saffman. The lift on a small sphere in a slow shear flow. *Journal of Fluid Mechanics*, 22(2):385400, 1965.

[46] D. Legendre and J. Magnaudt. The lift force on a spherical bubble in a viscous linear shear flow. *Journal of Fluid Mechanics*, 368:81126, 1998.

[47] R. Zamansky, F. Coletti, M. Massot, and A. Mani. Turbulent thermal convection driven by heated inertial particles. *Journal of Fluid Mechanics*, 809:p390–437, 2016.

[48] Z.T. Zhang, D. Legendre, and R. Zamansky. Model for the dynamics of micro-bubbles in high-reynolds-number flows. *Journal of Fluid Mechanics*, 879:554578, 2019.

[49] W. J. T. Bos and R. Zamansky. Power fluctuations in turbulence. *Physical Review Letters*, 122(12):124504, 2019.

[50] S.A. Orszag. Accurate solution of the orrsommerfeld stability equation. *Journal of Fluid Mechanics*, 50(4):689703, 1971.

[51] C. Canuto, M.Y. Hussaini, A. Quarteroni, and T.A. Zang. *Some Algorithms for Unsteady Navier-Stokes Equations.* Springer Berlin Heidelberg, Berlin, Heidelberg, 1988.

[52] S. A. Orszag. On the elimination of aliasing in finite-difference schemes by filtering high-wavenumber components. *Journal of the Atmospheric Sciences*, 28(6):1074–1074, 1971.

[53] D. Pekurovsky. P3dfft: a framework for parallel computations of fourier transforms in three dimensions. *SIAM Journal on Scientific Computing*, 34(4):C192–C209, 2012.

[54] S.Y. Chen, G.D. Doolen, R.H. Kraichnan, and Z.S. She. On statistical correlations between velocity increments and locally averaged dissipation in homogeneous turbulence. *Physics of Fluids A: Fluid Dynamics*, 5(2):458–463, 1993.

[55] P.K. Yeung, S.B. Pope, A.G. Lamorgese, and D.A. Donzis. Acceleration and dissipation statistics of numerically simulated isotropic turbulence. *Physics of Fluids*, 18(6):065103, 2006.

[56] J.S. Hadamard. Mouvement permanent lent dune sphère liquide et visqueuse dans un liquide visqueux. *Comptes rendus de l'Académie Des Sciences*, V152:p1735 –1738, 1911.

[57] B. Rybczynski. On the translatory motion of a fluid sphere in a viscous medium. *Bulletin international de l'Académie des sicences de Cracovie Serie A*, pages p40 –46, 1911.

[58] S. Huisman, P. Ern, and V. Roig. Interaction and coalescence of large bubbles rising in a thin gap. *Physical Review E : Statistical, Nonlinear, and Soft Matter Physics*, vol. 85:pp. 027302–1–027302–4, 2012.

[59] R.E.G. Poorte and A. Biesheuvel. Experiments on the motion of gas bubbles in turbulence generated by an active grid. *Journal of Fluid Mechanics*, 461:127154, 2002.

[60] M.R. Snyder, O.M. Knio, J. Katz, and O.P. Le Maître. Statistical analysis of small bubble dynamics in isotropic turbulence. *Physics of Fluids*, 19(6):065108, 2007.

[61] A. Aliseda and J.C. Lasheras. Preferential concentration and rise velocity reduction of bubbles immersed in a homogeneous and isotropic turbulent flow. *Physics of Fluids*, 23(9):093301, 2011.

[62] W. Hwa-Chi and J. Walter. Particle density correction for the aerodynamic particle sizer. *Aerosol Science and Technology*, 6(2):191–198, 1987.

[63] C.Y. Yang and U. Lei. The role of the turbulent scales in the settling velocity of heavy particles in homogeneous isotropic turbulence. *Journal of Fluid Mechanics*, 371:179205, 1998.

[64] A. Aliseda, A. Cartellier, and J.C. Hainaux, F.and Lasheras. Effect of preferential concentration on the settling velocity of heavy particles in homogeneous isotropic turbulence. *Journal of Fluid Mechanics*, 468:77105, 2002.

[65] K. Kawanisi and R. Shiozaki. Turbulent effects on the settling velocity of suspended sediment. *Journal of Hydraulic Engineering*, 134(2):261–266, 2008.

[66] P.D. Friedman and J. Katz. Mean rise rate of droplets in isotropic turbulence. *Physics of Fluids*, 14(9):3059–3073, 2002.

[67] P.D.M. Spelt. On the motion of gas bubbles in homogeneous isotropic turbulence. *Journal of Fluid Mechanics*, 336:211–244, 1997.

[68] E.A. Van Nierop, S. Luther, J.J. Bluemink, J. Magnaudet, A. Prosperetti, and D. Lohse. Drag and lift forces on bubbles in a rotating flow. *Journal of Fluid Mechanics*, 571:439454, 2007.

[69] M. Rastello, J. Marié, and M. Lance. Drag and lift forces on clean spherical air bubbles in a rotating flow. *International Conference on Multiphase Flow*, page 5, 2010.

[70] V. Mathai, E. Calzavarini, J. Brons, C. Sun, and D. Lohse. Microbubbles and microparticles are not faithful tracers of turbulent acceleration. *Phys. Rev. Lett.*, 117:024501, 2016.

[71] E. Calzavarini, M. Kerscherk, D. Lohse, and F. Toschi. Dimensionality and morphology of particle and bubble clusters in turbulent flow. *Journal of Fluid Mechanics*, 607:1324, 2008.